University of California
Santa Barbara

Realization and ground state properties of topological superconductors in one dimension

A dissertation submitted in partial satisfaction
of the requirements for the degree

Doctor of Philosophy
in
Physics

by

Younghyun Kim

Committee in charge:

Professor Chetan Nayak, Co-chair
Doctor Roman M. Lutchyn, Co-chair
Professor John Martinis
Professor Cenke Xu

June 2016

The Dissertation of Younghyun Kim is approved.

Professor John Martinis

Professor Cenke Xu

Doctor Roman M. Lutchyn, Committee Co-chair

Professor Chetan Nayak, Committee Co-chair

June 2016

Realization and ground state properties of topological superconductors in one dimension

by

Younghyun Kim

Acknowledgements

My six-year-long journey at UCSB would not have been possible without supports from many people. First of all, I would like to thank my advisors, Chetan Nayak and Roman Lutchyn, for their guidance. They have taught me how to find and solve interesting problems, how to write and present to share the results with other physicist. They also have provided me chances to interact with physicists outside of UCSB by supporting me to attend many conferences and workshops. Most importantly, their encouragements with patience have kept me on track and made this journey an enjoyable one.

I also want to thank the other members of my committee, Cenke Xu and John Martinis. Cenke's classes helped me understanding many important concepts in condensed matter physics. He also has organized CMT group meetings from which I learned about various researches in the field. The collaborative meetings with Martinis' group served as a great opportunity to learn and interact with experimentalists. Using this experience as a starting point, I could participated in several successful experimental physics projects. Among them, I learned a lot from the series of collaborations with Chris Palmstrøm and Javad Shabani. Especially, I am so grateful for discussions with Javad where I learned many interesting aspects of material science and condensed matter experiment.

I have had great opportunities to collaborate with many physicists around the world including Sanka Das Sarma, Enrico Rossi, Junhua Zhang, Erikas Gaidamauskas, Jens Paaske and Karsten Flensberg. Discussions with them have been always insightful and provided constructive feedback on the works presented in this dissertation.

Interactions and collaborations with people in Station Q have been very valuable experiences for me. In particular, I appreciate Bela Bauer for answering my questions on basic numerics. Meng Cheng and Dong Liu have guided me through all the technical details in calculations for RG analysis and slave-boson theory. I also want to thank

former and current Station Q graduate students: Jennifer Cano, Eugeniu Plamadeala, Brayden Ware, Kaushal Patel, Dominic Else and Christina Knapp for all the discussions and group meetings.

I want to thank my Korean colleagues: Eun-Gook Moon, SungBin Lee, Hyejin Ju, Gil-Young Cho, Soonwon Choi, Jeongwan Haah and Isaac Kim for interesting conversations on physics and many other subjects during their stays in Santa Barbara. I also want to thank Hyungwon Kim for interesting discussions during the PSSCMP and Boulder summer school.

None of this dissertation would have been possible without the support of my family. I thank my parents for their never ending love. I also want to thank my brother who has been always supporting me. Finally, I thank my wife for all the emotional supports and love.

Curriculum Vitæ

Younghyun Kim

Education

2016	Ph.D. in Physics, University of California, Santa Barbara.
2008	B.S. in Physics, Massachusetts Institute of Technology.

Publications

1	Younghyun Kim, Dong E. Liu, Erikas Gaidamauskas, Jens Paaske, Karsten Flensberg, and Roman M. Lutchyn, "Signatures of Majorana Kramers Pairs in superconductor-Luttinger liquid and superconductor-quantum dot-normal lead junctions," arXiv: 1605.02073.
2	J. Shabani, M. Kjaergaard, H. J. Suominen, Younghyun Kim, F. Nichele, K. Pakrouski, T. Stankevic, R. M. Lutchyn, P. Krogstrup, R. Feidenhans'l, S. Kraemer, C. Nayak, M. Troyer, C. M. Marcus, and C. J. Palmstrøm, "Two-dimensional epitaxial superconductor - semiconductor heterostructures: A platform for topological superconducting networks," Phys. Rev. B 93, 155402 (2016)
3	Junhua Zhang, Younghyun Kim, Enrico Rossi, and Roman M. Lutchyn, "Topological superconductivity in a multichannel Yu-Shiba-Rusinov chain," Phys. Rev. B **93**, 024507 (2016).
4	Younghyun Kim, Junhua Zhang, Enrico Rossi, and Roman M. Lutchyn, "Impurity-induced bound states in superconductors with spin-orbit coupling," Phys. Rev. Lett. **114**, 236804 (2015).
5	Kalon Gopinadhan, Anil Annadi, Younghyun Kim, Amar Srivastava, Brijesh Kumar, Jingsheng Chen, J. Michael D. Coey, Ariando, Thirumalai Venkatesan, "Carrier confinement effects and gate tunable anisotropic spin-orbit coupling at $LaAlO_3/SrTiO_3$ (110) interface," Adv. Electron. Mater. 1500114 (2015).
6	J. Shabani, Younghyun Kim, T. McFadden, R. M. Lutchyn, C. Nayak, and C. J. Palmstrøm, "Probing spin orbit interaction in InAs/InGaAs gate-defined one-dimensional channels," arXiv: 1408.1122.
7	Younghyun Kim, Meng Cheng, Bela Bauer, Roman M. Lutchyn, and Sankar Das Sarma, "Helical order in one-dimensional

magnetic atom chains and possible emergence of Majorana bound states," Phys. Rev. B **90**, 060401(R) (2014).

8 Younghyun Kim, Roman M. Lutchyn, and Chetan Nayak, "Origin and transport signatures of spin-orbit interactions in one- and two- dimensional $SrTiO_3$-based heterostructures," Phys. Rev. B **87**, 245121 (2013).

9 Younghyun Kim, Jennifer Cano, and Chetan Nayak, "Majorana zero modes in semiconductor nanowires in contact with higher-Tc superconductors," Phys. Rev. B **86**, 235429 (2012).

Abstract

Realization and ground state properties of topological superconductors in one dimension

by

Younghyun Kim

Topological superconductors with and without time-reversal symmetry are new phases of matters which host Majorana zero modes at their ends. The possibility of realizing such phases in various kinds of materials that are experimentally accessible, in addition to their unique signatures in simple transport measurements, has brought significant amount of attention from both theorists and experimentalists in condensed matter physics. In this thesis, we extend the previous studies on the realization of topological superconductors and try to answer some of the open questions regarding their transport signatures.

First, we study extensions of the realization scheme based on semiconducting nanowires proximity coupled to $s-$wave superconductors [54, 69] by replacing the s-wave superconductor with high temperature superconductors. We show that significant amount of induced superconducting gap in a nanowire can be achieve for a special interface geometry. The existence of gapless nodal excitations in the cuprate superconductors lead to a finite lifetime of Majorana zero modes when they are coupled to fermionic bath. We also consider the topological superconductivity in the Yu-Shiba-Rusinov states in chains of magnetic atoms at the surface of two dimensional $s-$wave superconductors with strong spin-orbit coupling. We study the generalization of the single Shiba state problem into a multiple Shiba states problem in the presence of spin-orbit coupling. We show that spin-orbit coupling induces the mixing of Shiba states correspond to different angular momentum channels and leads to interesting effects such as angular dependence of Shiba spectrum on the direction of magnetic moment. Based on these newly discovered effects,

we propose new experimental methods to analyze and tune the physical parameters of the magnetic atom chains which can be applied to the ongoing experiments [62, 70, 79]. Using the formalism developed for a single impurity, we study the magnetic atom chains with multiple Shiba state bands and present the topological phase diagram.

Next, we study the transport signatures of time-reversal invariant topological superconductors which support Kramers pair of Majorana modes. Especially, we explore the effects of interactions on the transport signatures in tunnel junctions involving Majorana Kramers pairs by considering two types of junction geometries. We first consider a junction between Majorana Kramers pair and Luttinger liquid. Using renormalization group (RG) analysis, we study the boundary conditions of the infrared fixed points where system flows to as a function of interaction strength. In the presence of weak repulsive interactions in the Luttinger liquid, two channel Andreev reflection is stable in contrast to the junction between an interacting lead and a conventional $s-$wave superconductor. Second, we study the ground state properties of Majorana Kramers pair-quantum dot-normal lead junction using weak coupling RG and slave-boson mean-field theory. We find that the Kodno interaction between the lead electrons and the quantum dot and the Majorana-quantum dot interaction compete each other. We find a new strong coupling fixed point characterized by strong correlation between impurity spin and Majorana Kramers pair, and we study its signatures in differential tunneling conductance.

Contents

List of Figures

Chapter 1

Introduction

In superconductors where charge conservation symmetry is broken, fermionic quasiparticles, Bogoliubov quasiparticles, are mixtures of electrons and holes. For spinless superconductors, a Bogoliubov quasiparticle operator can be written as

$$\gamma_i = \sum_j u_i(j) c_j^\dagger + v_i(j) c_j \tag{1.1}$$

where $c_j/c_j^\dagger$ is the annihilation/creation operator for an electron at position j. When u_i and v_i satisfy the condition $u_i(j)^* = v_i(j)$, γ_i is equal to $\gamma_i^\dagger$ which makes it a Majorana fermion operator. A superconductor that hosts Majorana quasiparticles at its defects is called a topological superconductor. In one dimension, topological superconductors support localized zero energy Majorana quasiparticles, Majorana zero modes (MZMs) at their ends. There has been a great interest in realizing and detecting MZMs since they obey the non-Abelian braiding statistics which is a key element for topological quantum computation [43, 65].

In this chapter, we will review the previous works on topological superconductivity in one dimension, and establish the background for the later chapters. For more details

on the subject, please refer to the review by Alicea [4].

1.1 Toy model: Kitaev's chains

We begin with a toy model [45] for one dimensional topological superconductor which hosts one localized MZM at each end of it. The model consists of spinless fermions c_j with nearest neighbor hopping and pairing (p-wave) terms. The Hamiltonian is given by

$$H = -\sum_{j=1}^{L} \mu c_j^\dagger c_j - \sum_{j=1}^{L-1} \left[t c_j^\dagger c_{j+1} + \Delta e^{i\theta} c_j c_{j+1} + \text{h.c.} \right] \tag{1.2}$$

where L is the length of the chain, t is the hopping energy, Δ is the pairing amplitude and θ is the superconducting phase. We set t and Δ to be real. For $\Delta = 0$, the normal state spectrum of the above Hamiltonian in momentum space follows $\cos ka$ band structure with bandwidth $4|t|$. Here a is the lattice constant used for Fourier transformation. When $\mu > |2t|$, the ground state of this Hamiltonian corresponds to the vacuum state. For $|\mu| < |2t|$, once we introduce a small $p-$wave pairing gap Δ, the spectrum opens up a gap $\propto \Delta \sin k_F a$ at the Fermi momenta $\pm k_F$. It turns out that there is a crucial difference between the above two gapped states that when we put them together, a MZM arises at the boundary. To see this in more explicit way, we transform a complex fermion operator c_j into two Majorana fermion operators as

$$c_j = \frac{e^{-\frac{i\theta}{2}} (\gamma_{2j-1} + i\gamma_{2j})}{2} \tag{1.3}$$

with

$$\gamma_k = \gamma_k^\dagger \text{ and } \{\gamma_k, \gamma_l\} = 2\delta_{kl}. \tag{1.4}$$

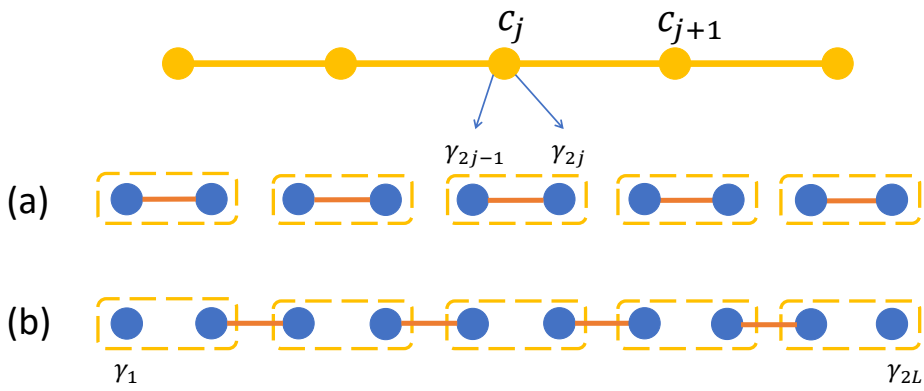

Figure 1.1: Illustration of the two different phases of Kitaev chain model. (a) Trivial phase. (b) Topological phase.

In terms of these new Majorana fermion operators, our Hamiltonian read

$$H = -\frac{\mu}{2}\sum_{j=1}^{L}[1 + i\gamma_{2j-1}\gamma_{2j}] + \frac{i}{2}\sum_{j=1}^{L-1}[(t-\Delta)\gamma_{2j-1}\gamma_{2j+2} - (t+\Delta)\gamma_{2j}\gamma_{2j+1}] \tag{1.5}$$

Note that the eigenvalue of $i\gamma_{2j}\gamma_{2j+1} = 1$ or -1 corresponds to filled or empty state for j's site, $n_j = c_j^\dagger c_j = 1$ or 0. Now let us consider two special points in the parameter sapce. First, when $\Delta = t = 0$ and $\mu < 0$ the ground state can be characterized by

$$i\gamma_{2j-1}\gamma_{2j} = -1 \tag{1.6}$$

for all j which is a vacuum state for c_js. In this case, two Majorana fermions in the same site form a pair as illustrated in Fig. 1.1 (a). Next, we consider the case when $t = \Delta > 0$ and $\mu = 0$. In this limit, the Hamiltonian simplifies to

$$H = -i\Delta\sum_{j=1}^{L-1}\gamma_{2j}\gamma_{2j+1} \tag{1.7}$$

where the ground state corresponds to $i\gamma_{2j}\gamma_{2j+1} = -1$ for $j = 1$ to $L-1$, see Fig. 1.1 (b). Now one can immediately find that γ_1 and γ_{2L} do not appear in the effective Hamiltonian (1.7), as a result, there are two degenerate ground states corresponding to two eigenstates of MZMs, $i\gamma_1\gamma_{2L} = \pm 1$. Then, the two ground states can be connected to occupied/unoccupied zero energy single-particle orbital

$$d = \frac{\gamma_1 + i\gamma_{2L}}{2}. \tag{1.8}$$

In principle, the above Hamiltonian is the simplest case for a fined-tuned point in the parameter space, and one can, in general, have a splitting term $i\delta\gamma_1\gamma_{2L}$ analogous to the wavefunction overlap between two MZMs. However, in the topological phase with finite gap, this splitting energy will be exponentially suppressed as $\delta \propto e^{-L/\xi}$ for a coherence length ξ of the system.

We can naturally extend the Kitaev's toy model into a spin-1/2 case with time-reversal symmetry: two decoupled chains with $p-$wave intra-channel pairings. Those two chains could be time-reversal partners of each other. In this case, the system can support two MZMs (i.e. $\gamma_\uparrow$ and $\gamma_\downarrow$) at each ends. In the presence of time-reversal symmetry, the splitting term $i\gamma_\uparrow\gamma_\downarrow$ is not allowed, and the pair of MZMs are protected. These two MZMs are called Majorana Kramers pair. The realization of this spin-1/2 system with Majorana Kramers pair requires strong intra-channel pairing while conventional s-wave pairing is between two different spin channels. We introduce the previous works on the realization of Majorana Kramers pairs in Chapter 4.

Going back to the original discussion on the single Kitaev's chain, we have seen how MZMs can arise in spinless $p-$wave superconductors. However, in experiment, we are dealing with spin-$\frac{1}{2}$ electrons, and it requires clever engineering to realize effectively *spinless* topological superconductivity in electronic materials. There has been lots of

efforts to realize the Kitaev's model based on various materials including topological insulators [29, 30, 17], semiconducting wires [54, 69], half metallic wires [22, 13, 89], magnetic atoms at the surface of superconductors and more. In the following section, we review the proposals based on semiconducting wires. For discussion on proposals based on magnetic atoms, see Sec. 3.1.

1.2 Realization of topological superconductivity in nanowires

In this section we review the realization schemes of one dimensional topological superconductor using semiconducting nanowires [54, 69]. There have been a lot of successful experimental efforts [60, 18, 19, 27, 14, 20, 36, 3, 97] on realizing the topological superconductivity and detecting the signal of MZMs using semiconducting nanowires due to the ability to control the carriers easily by applying gate voltages. Devices based on the nanowires allow us to naturally build a tunnel junction. By covering a part of the wire, the system becomes normal-topological superconductor junction. Using a gate at the junction as a tunneling barrier, one can easily tune the transparency of the junction. We discuss the signatures of MZMs in such tunnel junction setups in the next section.

In the nanowire proposal there are three key ingredients for realizing the effective Hamiltonian for Kitaev's spinless p-wave superconductor: 1) one dimensional electrons with spin-orbit coupling. 2) proximity induced gap from a bulk s-wave superconductor. 3) Zeeman splitting by applied magnetic field. These ingredients can be combined as illustrated in Fig. 1.2 (a). The model Hamiltonian can be written as

$$H = \int dk \left[\psi_k^\dagger \left(\frac{k^2}{2m^*} - \mu + \alpha \sigma_y k + h \sigma_x \right) \psi_k + \Delta \psi_{\uparrow k} \psi_{\downarrow -k} + \text{h.c.} \right]. \tag{1.9}$$

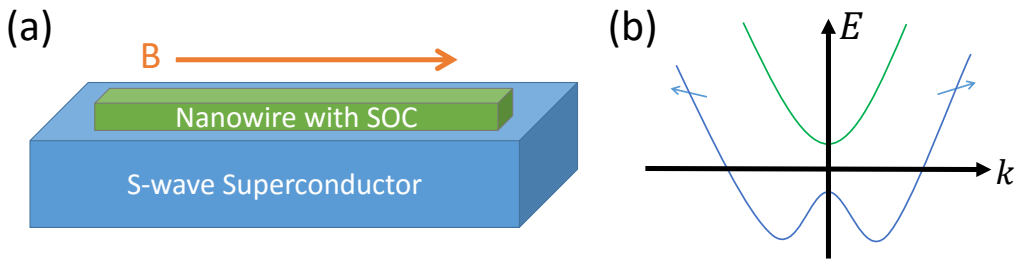

Figure 1.2: Schematic set up for realizing topological superconductivity in a nanowire(a) and its normal state band structure (b).

Here ψ is the annihilation operator for an electron in the nanowire with effective mass m^*. α is the size of the spin-orbit coupling and h is the Zeeman splitting energy. When a nanowire is coupled to a bulk $s-$wave superconductor with finite tunneling strength, effective pairing gap Δ is induced by the proximity effect. We will study the proximity effect for more general cases in Chapter 2. Let us consider the normal state $\Delta = 0$ first. In the presence of both spin-orbit coupling and Zeeman term, the band structure can be described as in Fig. 1.2 (b). The gap at $k = 0$ opens when the direction of spin-orbit coupling (y) and Zeeman term (x) are not aligned. When the chemical potential μ locates within the gap, only the bottom band are partially filled and we are in the effectively spinless limit. Introducing the induced pairing Δ in this limit leads to gap opening at the Fermi momenta. In the limit of large Zeeman energy $h \gg \Delta, \alpha k_F$ one can prject the pairing term to the bottom band and the effective intra-band pairing looks like a $p-$wave pairing [5], therefore, the nanowire is in the topological phase and supports MZMs at its ends. The transition between trivial phase and topological phase accompany the closing of the bulk gap. The gap at $k = 0$ closes when $h = \sqrt{\Delta^2 + \mu^2}$ at which the topological phases transition happens. Therefore, the condition for the wire to be in topological

phase can be given as

$$h > \sqrt{\Delta^2 + \mu^2}. \tag{1.10}$$

The above condition for the topological phase can be reproduced by solving Bogoliubov-de Gennes (BdG) equation for MZMs. We discuss the method to find zero energy solution in Sec. 2.2.5.

1.3 Transport signatures of Majorana zero modes in tunneling geometries

Here we review the properties of MZMs coupled to one dimensional lead through a tunneling barrier. For non-interacting systems, a MZM coupled to a normal electrons through tunnel junction leads to the $2e^2/h$ differential conductance at zero bias voltage due to the perfect Andreev reflection at the junction [48]. For example, let us consider a spinless lead, or helical lead (HL), coupled to a MZM at $x = 0$. The model can be described by

$$H = H_{\mathrm{HL}} + t\gamma(\psi(0) - \psi_\dagger(0)) \tag{1.11}$$

where H_{HL} describes the bulk theory of the helical lead, t is the tunneling amplitude for the junction, γ is the MZM and $\psi^\dagger(x)$ is the creation operator for the electron in HL at position x. Here we assume a semi-infinite nanowire where the coupling between two MZMs at opposite ends can be ignored. Then, the scattering matrix for incident electrons with energy E at the junction can be described as [66]

$$S(E) = \hat{I} + 2\pi i \hat{W}^\dagger \left(-E - i\pi \hat{W}\hat{W}^\dagger\right)^{-1} \hat{W}, \tag{1.12}$$

where

$$\hat{W} = (t, -t) \tag{1.13}$$

describes the coupling between the MZM and electrons in the HL. At zero bias, $E = 0$, we get

$$S(0) = \begin{pmatrix} 0 & 1 \\ 1 & 0 \end{pmatrix} \tag{1.14}$$

Here the diagonal elements correspond to normal reflection amplitudes for electron to electron channel and hole to hole channel, while the offdiagonal components correspond to the amplitudes for Andreev reflections. Note that the reason for the perfect Andreev reflection with amplitude one is the fact that γ is coupled to $\psi(0)$ and $\psi^\dagger(0)$ with equal tunneling strength. This fact follows from the hermicity and the definition of Majorana fermion, $\gamma = \gamma^\dagger$. The differential conductance at the tunnel junction is given by

$$G(E) = \frac{2e^2}{h}|S_{12}(E)|^2 \tag{1.15}$$

which leads to $G(0) = 2e^2/h$.

In the case of spinful lead coupled to a MZM, one can diagonalize the tunneling terms such that the MZM is now coupled to only one spin channel. In this case, the same scattering matrix analysis leads to a perfect Andreev reflection for the MZM coupled spin channel and a perfect Normal reflection for the other channel, which yields $G(0) = 2e^2/h$ again.

In the presence of electron-electron interactions in the lead, the above conclusion on zero bias differential conductance could be modified. The effects of interactions have been considered using the Luttinger liquid formalism [26, 2, 55]. For example, the Hamiltonian

corresponds to (1.11) becomes

$$H = H_{\mathrm{LL}} + t\gamma(\psi(0) - \psi_{\dagger}(0)) \tag{1.16}$$

by replacing the HL part with the interacting spinless Luttinger liquid Hamiltonian with Luttinger parameter K. Then, we can analyze the stability of the normal reflection fixed point by looking at the tree level renormalization group (RG) flow of the coupling t:

$$\frac{dt}{dl} = \left(1 - \frac{1}{2K}\right) t \tag{1.17}$$

where $l = \ln b$ denotes the change in ultraviolet cutoff scales from Λ to Λ/b. One can immediately see that coupling to MZM, t is relevant for $K > 1/2$, therefore, the normal reflection is unstable in this limit, and the system flows to the perfect Andreev reflection fixed point. This result agrees with the scattering matrix analysis for the non-interacting HL ($K = 1$). In the case of spinful Luttinger liquid coupled to a MZM, similar analysis leads to the RG equation

$$\frac{dt}{dl} = \left(1 - \frac{1}{4K_{\sigma}} - \frac{1}{4K_{\rho}}\right) t \tag{1.18}$$

where $K_{\sigma/\rho}$ is the Luttinger parameter for spin/density channel. Therefore, we find that with Majorana the system will generically flow to Andreev fixed point.

On the contrary, normal reflection fixed point is quite stable for the case of a Luttinger liquid coupled to a conventional s-wave superconductor. Without MZMs, the most relevant perturbation we can add at the normal reflection fixed point is a local pairing:

$$H_{\Delta} = \Delta\psi_{\uparrow}^{\dagger}(0)\psi_{\downarrow}^{\dagger}(0). \tag{1.19}$$

For $K_{\sigma} = 1$, this term is relevant only when there is attractive interaction in the lead,

$K_\rho > 1$. Therefore, for attractive interaction in the lead, the Andreev reflection fixed point is stable whereas for repulsive interaction it is unstable. The non-interacting limit with $K = 1$ is a special case where the outcome depends on the ratio between the amplitudes of cooper pair tunneling and back scattering. In constrast to this, we have seen that, in the case of MZMs coupled to spinless/spinful leads, Andreev reflection fixed point is stable against moderate repulsive interactions $K_\rho > 1/2$ or $K_\rho > 1/3$. Therefore, the quantized zero bias differential conductance of $2e^2/h$ is a universal signature of the tunnel junction between an interacting lead and a topological superconductor.

In the case of a junction between a spinful normal lead and a time-reversal invariant topological superconudctor with Majorana Kramers pair, we have $4e^2/h$ zero bias differential conductance due to the presence of MZM in each spin channel. In Chapter 4, we discuss the effect of various interactions on the differential conductance.

1.4 Outline

We conclude this introduction with an outline of the remainder of the thesis. In Chapter 2, we present the new realization scheme based on a semiconducting nanowire in contact with $d-$wave high temperature superconductors. We study the condition for being in the topological phase, ideal geometry that optimizes the induced gap, and stability of MZM in such system. In Chapter 3, we study a system consists of a ferromagnetic chain of atoms at the surface of superconductor. By developing a formalism for studying multiple bound states for magnetic impurities in two dimensional superconductor, we extend the previous works on realizing MZM based on single impurity band into multiple impurity bands model. In Chapter 4, transport signatures of time-reversal invariant topological superconductors are studied in the presence of interactions. We consider two geometries: 1) Tunnel junction between Luttinger liquid-Majorana Kramers pair. 2)

Majorana Kramers pair-quantum dot-normal lead junction. For the first case, we study the effects of interactions in the lead on the differential conductance at zero bias. For the second case, the competition between the Kondo interaction between the quantum dot and the normal lead and the Majorana induced interaction between the quantum dot and the Majorana Kramers pair is discussed. We conclude in Chapter 5 with possible future direction of the field of topological superconductivity.

Chapter 2

Majorana zero modes in nanowires in contact with $d-$wave superconductors

In this chapter, we investigate the possibility of realizing Majorana zero mode using high temperature superconductors with $d-$wave pairing symmetry such as cuprate superconductors. We show that, by using clever geometry such as step edge surface, one can induce pairing gap in the nanowire and realize Majorana zero mode in the presence of Zeeman coupling. We also study the stability of the Majorana modes in the presence of a coupling to the nodal gapless excitations in cuprates.

The content of this chapter is reprinted with permission from Phys. Rev. B 86, 235429 (2012) available online at `http://dx.doi.org/10.1103/PhysRevB.86.235429`

2.1 Introduction

For a finite length nanowire, the stability of MZM at its ends is determined by the size of the topological gap. Deep inside the topological phase where Zeeman energy is greater than the induced gap, the topological gap of the wire is mainly determined by the quasi-particle gap at the Fermi momenta. In a realistic situation, this quasi-particle gap is proportional to the induced pairing gap in the nanowire. Therefore, choosing superconductors with larger pairing gap and higher critical field can increase the induced gap and the stability of MZM. Therefore, there were several studies on the realization of MZM using high temperature superconductors such as pnictides and cuprates.[40, 94, 88, 64, 96, 24] In the following we will study the case for $d-$wave superconductors. One of the interesting aspects of the cuprate superconductors is their non-trivial pairing symmetry. Due to the sign structure and gapless nodal lines in the pairing potential, it is far from clear that the cuprate superconductors can induce a proximity effect in the nanowire. In what follows, we will show that $d-$wave superconductors can induce a large pairing gap when their steplike structure is used to form an interface with nanowires. MZM in this system can be coupled to gapless nodes and gains finite lifetime. We will study the decay rate of MZM in the presence of such couplings.

2.2 Proximity effect and existence of Majorana zero modes

2.2.1 Model

We consider a quasi-1D semiconductor nanowire of length L_x aligned along the x-axis, with width w in the y-axis and width w_z in the z-direction. We will assume that

the $x-$axis and $y-$axis are pointing in the (100) and (010) crystallographic directions of the underlying superconductor. As a result, in momentum space, (110) direction is aligned with the gapless nodes of the $d-$wave superconductor. We will assume that $w_z \ll w \ll L_x$ and consider only the lowest energy quantization along the z-axis. We will allow multiple sub-bands in the y-direction. The nanowire is described by the action S_{NW} while the superconductor is described by the action S_{SC} as shown below. The coupling between the electrons in the nanowire and quasi-particles in the superconductor is described by S_T.

$$\begin{aligned} S_{NW} =& \frac{2\pi}{\beta}\sum_m\sum_i\int dk_x \bar{\Psi}_{m,i,k_x}\left\{-i\omega_m + \alpha k_x\sigma_y\tau_z + \left(\epsilon_{k_x} + \tfrac{\hbar^2(\pi i)^2}{2m^* w^2} - \mu\right)\tau_z + V_x\sigma_x\right\}\Psi_{m,i,k_x} \\ S_{SC} =& \frac{2\pi}{\beta}\sum_m\int_{\mathbf{q}} \bar{c}_{m,\mathbf{q}}(-i\omega_m + \xi_q\tau_z + \Delta_q\tau_x)c_{m,\mathbf{q}} \\ S_T =& \frac{2\pi}{\beta}\sum_{m,i}\int dk_x\int_{\mathbf{q}} t_i(k_x,\mathbf{q})\bar{\psi}_{m,i,k_x}c_{m,\mathbf{q}} + h.c. \end{aligned} \tag{2.1}$$

Here ω_m is Matsubara frequency, and i is a sub-band index in the nanowire. Ψ and c are the vectors in the Nambu space where σ's and τ's correspond to Pauli matrices in the spin sector and the particle-hole sector for each. For example, $\Psi_{m,i,k_x} = (\psi_{m,i,k_x\uparrow}, \psi_{m,i,k_x\downarrow}, \bar{\psi}_{-m,i,-k_x\downarrow}, -\bar{\psi}_{-m,i,-k_x\uparrow})^T$. The functions $t_i(k_x,\mathbf{q})$ are the tunneling amplitudes between the superconductor and the i^{th} sub-band of the semiconductor nanowire. We assume for simplicity that the electron wavefunction in the i^{th} sub-band of the nanowire takes the form $\psi(x,y) = \sqrt{\frac{1}{w}}\sin(\frac{\pi y i}{w})\,\psi(x)$. We assume a parabolic dispersion along the $x-$axis $\epsilon_{k_x} \equiv \frac{\hbar^2 k_x^2}{2m^*}$, and m^*, $V_x = g\mu_B B_x/2$, μ and α are, respectively, the effective mass, Zeeman splitting, chemical potential, and stength of spin-orbit coupling in the nanowire. In the absence of superconductivity, the chemical potential is related to

the Fermi momentum $k_{F,i}$ in the i^{th} sub-band according to

$$\frac{\hbar^2 k_{F,i}^2}{2m^*} + \frac{\hbar^2(\pi i)^2}{2m^* w^2} - \mu = \sqrt{V_x^2 + \alpha^2 k_{F,i}^2} \tag{2.2}$$

We will take the following form [68] for the band structure in a cuprate superconductor:

$$\begin{aligned}\xi_q(eV) =& t_0 + t_1(\cos q_x a + \cos q_y a)/2 + t_2 \cos q_x \cos q_y + t_3(\cos 2q_x a + \cos 2q_y a)/2 \\ &+ t_5 \cos 2q_x a \cos 2q_y a + t_4(\cos 2q_x a \cos q_y a + \cos q_x a \cos 2q_y a)/2 \end{aligned} \tag{2.3}$$

where $t_0 = 0.1305, t_1 = -0.5951, t_2 = 0.1636, t_3 = -0.0519, t_4 = -0.1117, t_5 = 0.051$ (all in units of electron volts) and $a \approx 4\,\text{Å}$. We will take a superconducting gap of the form $\Delta_q = \Delta_0(\cos q_x a - \cos q_y a)/2$ and the representative value $\Delta_0 = 30$ meV.

2.2.2 Tunneling between the nanowire and the superconductor

Using the assumed form $\psi(x,y) = \sqrt{\frac{1}{w}} \sin(\frac{\pi y i}{w})\, \psi(x)$ for the electron wavefunction in the i^{th} sub-band in the nanowire, we can write $t_i(k_x, \mathbf{q})$ using the real space tunneling amplitude $t(\mathbf{r}, \mathbf{r}')$ as follows:

$$t_i(k_x, \mathbf{q}) = \int dx \int_0^w dy \int d^2\mathbf{r}'\, t(\mathbf{r}, \mathbf{r}')\, e^{ik_x x - iq_x x'}\, \frac{e^{-iq_y y'} \sin(\frac{\pi y i}{w})}{\sqrt{w}}. \tag{2.4}$$

Due to the quantization along the y-axis we will encounter with the following expression:

$$\begin{aligned} g_j(q_y) &= \int_0^w dy \frac{e^{-iq_y y} \sin(\frac{\pi y j}{w})}{\sqrt{w}} \\ &= -i^{j+1}\, \frac{e^{-iq_y w/2}}{\sqrt{w}} \left[\frac{\sin((q_y w - \pi j)/2)}{q_y - \pi j/w} - (-1)^j \frac{\sin((q_y w + \pi j)/2)}{q_y + \pi j/w} \right] \end{aligned} \tag{2.5}$$

where j is the sub-band index. As one can expect, this function becomes more sharply peaked around $q_y = \pm\pi j/w$ as w is increased.

In the next section, we will consider three different kinds of tunneling matrix elements $t(\mathbf{r}, \mathbf{r}')$ between a cuprate superconductor and a semiconducting nanowire:

1. Momentum conserving tunneling due to a clean interface where $t(\mathbf{r}, \mathbf{r}') = t\delta^{(2)}(\mathbf{r} - \mathbf{r}')$. Then $t_i(k_x, \mathbf{q}) = t_i^{\mathrm{u}}(k_x, \mathbf{q})$ with

$$t_i^{\mathrm{u}}(k_x, q) \equiv t\delta(k_x - q_x)g_i(q_y). \tag{2.6}$$

2. Momentum independent tunneling for the dirty or rough interface. For illustrative purposes, we consider the extreme case of $t(\mathbf{k}, \mathbf{q}) = \lambda(\mathbf{q})$, independent of $\mathbf{k}$. Electrons in the nanowire are now coupled uniformly to entire Brillouin zone, where the gap can have different signs.

3. A nanowire on top of a step edge of a cuprate, as shown in Figure 2.1. We assume that the terraces are evenly spaced, with the terrace edges at $x_n = nl$. We take $l \approx$ 7nm, which corresponds to an angle $\theta \approx 10^\circ$. We assume the tunneling amplitude is dominated by the terrace edges x_n. We assume the steps are wide so that tunneling only occurs around $x = x_n$. There is no such restriction for $y-$axis. Then $t(\mathbf{r}, \mathbf{r}') = t\sum_n d\delta(x - x_n)\delta(x\cos\theta - x')\delta(y - y')$, where d is the length scale for the region in which tunneling happens for each step. This yields $t_i(k_x, \mathbf{q}) = t_i^{\mathrm{s}}(k_x, \mathbf{q})$ with

$$t_i^{\mathrm{s}}(k_x, \mathbf{q}) \equiv td\sum_j \delta(k_x - q_x\cos\theta + jQ)g_i(q_y) \tag{2.7}$$

where $Q = 2\pi/l$.

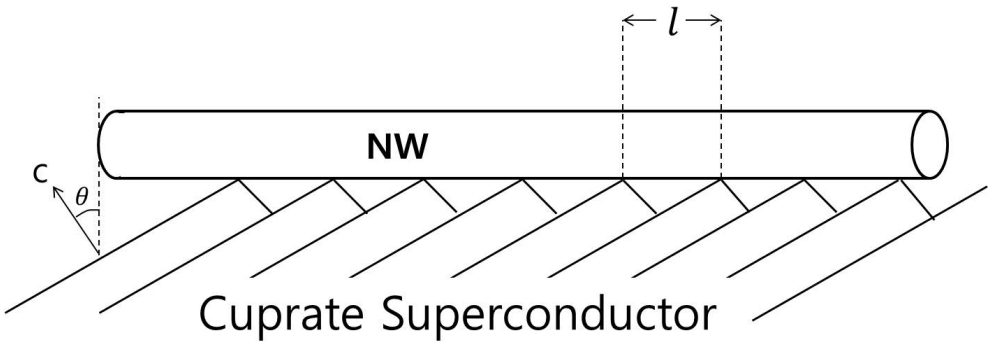

Figure 2.1: Schemetic diagram of an interface between a nanowire and a steplike surface of a cuprate superconductor.

2.2.3 Induced Superconductivity

Integrating out the superconductor's degrees of freedom generates an effective action for the nanowire $S_{\text{eff}} = S_{NW} + S'$ where

$$S' = -\frac{2\pi}{\beta}\sum_{m,i,j}\int_{k_x,k'_x,\mathbf{q}}\bar{\psi}_{m,i,k_x}\left[\frac{t_i(k_x,\mathbf{q})t_j(k'_x,\mathbf{q})^*}{-i\omega_m+\xi_q\tau_z+\Delta_q\tau_x}\right]\psi_{m,j,k'_x} \tag{2.8}$$

$$= -\sum_{m,i,j}\int_{k_x,k'_x}\bar{\psi}_{m,i,k_x}\left[ir_{k_x,k'_x,i,j,m}\omega_m+\epsilon'_{k_x,k'_x,i,j,m}\tau_z+\Delta'_{k_x,k'_x,i,j,m}\tau_x\right]\psi_{m,j,k'_x} \tag{2.9}$$

with

$$r_{k_x,k'_x,i,j,m} = \int\frac{d^2\mathbf{q}}{(2\pi)^2}\frac{t_i(k_x,\mathbf{q})t_j(k'_x,\mathbf{q})^*}{\omega_m^2+\xi_q^2+|\Delta_q|^2}, \tag{2.10}$$

$$\epsilon'_{k_x,k'_x,i,j,m} = \int\frac{d^2\mathbf{q}}{(2\pi)^2}\frac{t_i(k_x,\mathbf{q})t_j(k'_x,\mathbf{q})^*\,\xi_q}{\omega_m^2+\xi_q^2+|\Delta_q|^2}, \tag{2.11}$$

$$\Delta'_{k_x,k'_x,i,j,m} = \int\frac{d^2\mathbf{q}}{(2\pi)^2}\frac{t_i(k_x,\mathbf{q})t_j(k'_x,\mathbf{q})^*\,\Delta_q}{\omega_m^2+\xi_q^2+|\Delta_q|^2}. \tag{2.12}$$

The main difference between s-wave and d-wave superconductors comes from the structure of Δ_q. Especially, Δ_q vanishes for $q_x = \pm q_y$, and at the nodal points on the Fermi surface of a $d_{x^2-y^2}$ superconductor, the denominators in Eqs. 2.10-2.12 vanish quadrat-

ically at $\omega_m = 0$. Therefore, these integrals will diverge logarithmically unless the numerators also vanish. For an infinitely-long nanowire, momentum conservation along the wire (or momentum conservation up to a multiple of Q) prevents any coupling between low-energy electrons and the nodal points of the superconductor. Consequently, the numerators in Eqs. 2.10-2.12 are zero at the nodal points, and we do not have to deal with the divergence. However, for localized MZM, there will be a coupling to the nodal points. We will study this coupling perturbatively in Section 2.4.

From the total action $S_{\text{eff}} = S_{NW} + S'$, we obtain the spectrum from the poles of the Green function:

$$\begin{aligned} G^{-1} = &\left(\delta_{ij}\delta_{k_x k'_x} + r_{k_x,k'_x,i,j}(\omega)\right)\omega - \left(\left[\epsilon_{k_x} + \tfrac{\hbar^2(\pi i)^2}{2m^* w^2} - \mu\right]\delta_{ij}\delta_{k_x k'_x} - \epsilon'_{k_x,k'_x,i,j}(\omega)\right)\tau_z \\ &- \alpha k_x \sigma_y \tau_z - V_x \sigma_x + \Delta'_{k_x,k'_x,i,j}(\omega)\tau_x \end{aligned} \tag{2.13}$$

Here, we have analytically continued $i\omega_m \to \omega$ and written, e.g. $r_{k_x,k'_x,i,j,m} \to r_{k_x k'_x ij}(\omega)$. The smallest positive pole of this equation is the gap.

For simplicity, let us make the approximation that momentum is conserved in the x-direction. Now r, ϵ', Δ' are all diagonal in k_x and we can drop the subscript k'_x. If we neglect the dependence in ω in r, ϵ' and Δ', finding poles of Eq. (2.13) reduces to finding the eigenvalues of the matrix M:

$$M = (\delta_{ij} + r_{k_x,i,j}))^{-1}\left(\alpha k_x \sigma_y \tau_z + V_x \sigma_x + \Delta'_{k_x,i,j}\tau_x + \left(\left[\epsilon_{k_x} + \tfrac{\hbar^2(\pi i)^2}{2m^* w^2} - \mu\right]\delta_{ij} + \epsilon'_{k_x,i,j}\right)\tau_z\right) \tag{2.14}$$

We now take a limit $w \gg a$ where momentum non-conservation in the y-direction is small on the scale of the Fermi momentum of the superconductor. In this case, we can

make replace $g(q_y)$ with a sum of two delta functions.

$$g_j(q_y) \approx -\frac{\pi i^{j+1} e^{-iq_y w/2}}{2i\sqrt{w}}[\delta(q_y - \pi j/w) - (-1)^j \delta(q_y + \pi j/w)]. \tag{2.15}$$

(We will use the full expressions when we cite quantitative results.) In this limit, the expressions in the previous subsection for t^u and t^n are diagonal in sub-band indicies. Dropping the redundant subscript j, the effective action S_{eff} can be written as

$$\begin{aligned} S_{\text{eff}} =& \frac{2\pi}{\beta} \sum_{m,i} \int dk_x \bar{\Psi}_{k_x,i,m} \big[-i(1 + r_{k_x,i,m})\omega_m + \alpha k_x \sigma_y \tau_z + (\epsilon_{k_x} + \tfrac{\hbar^2(\pi i)^2}{2m^* w^2} - \mu - \epsilon'_{k_x,i,m})\tau_z \\ & + V_x \sigma_x - \Delta'_{k_x,i,m} \tau_x \big] \Psi_{k_x,i,m} \end{aligned} \tag{2.16}$$

with

$$r_{k_x,i,m} = \frac{|t_{i,k_x}|^2}{\omega_m^2 + \xi^2_{k_x,\pi i/w} + \left|\Delta_{k_x,\pi i/w}\right|^2}, \tag{2.17}$$

$$\epsilon'_{k_x,i,m} = \frac{|t_{i,k_x}|^2 \ \xi_{k_x,\pi i/w}}{\omega_m^2 + \xi^2_{k_x,\pi i/w} + \left|\Delta_{k_x,\pi i/w}\right|^2}, \tag{2.18}$$

$$\Delta'_{k_x,i,m} = \frac{|t_{i,k_x}|^2 \ \Delta_{k_x,\pi i/w}}{\omega_m^2 + \xi^2_{k_x,\pi i/w} + \left|\Delta_{k_x,\pi i/w}\right|^2}. \tag{2.19}$$

We now see that, in the limit in which we replace $g_j(q_y)$ by a sum of δ-functions, there is no coupling between the nanowire and the nodal points in the superconductor for generic values of k_x. For the momentum conserving tunneling, t_{i,k_x} is given by

$$|t_{i,k_x}|^2 = \int_{k'_x} \int \frac{d^2\mathbf{q}}{(2\pi)^2} t_i(k_x, \mathbf{q}) t_i(k'_x, \mathbf{q})^* \sim |t|^2 \tag{2.20}$$

The induced superconducting gap function is:

$$\Delta^{\text{ind}}_{k_x,i,m} = \frac{\Delta'_{k_x,i,m}}{1+r_{k_x,i,m}} = \frac{|t_{i,k_x}|^2 \Delta_{k_x,\pi i/w}}{\omega_m^2 + \xi^2_{k_x,\pi i/w} + \left|\Delta_{k_x,\pi i/w}\right|^2 + |t_{i,k_x}|^2} \tag{2.21}$$

At the Fermi surface, in the static limit, this is

$$\Delta^{\text{ind}}_{k_F,i} \equiv \Delta^{\text{ind}}_{k_F,i,0} = \frac{|t_{i,k_x}|^2 \Delta_{k_F,\pi i/w}}{|t_{i,k_F}|^2 + \xi^2_{k_F,\pi i/w} + \left|\Delta_{k_F,\pi i/w}\right|^2} \tag{2.22}$$

Note that $\xi_{k_{F,i}}$ usually does not vanish due to the mismatch between the Fermi momentum of the nanowire and that of the superconductor. This mismatch is one of the limiting factors for induced superconductivity. From the single-particle spectrum obtained from Eq. (2.14), we see that the single-particle gap at k_F in the i^{th} sub-band is:[83]

$$\Delta^{\text{qp}}_{k_F,i} = \frac{E_{SO}}{\sqrt{V_x^2 + E_{SO}^2}} \Delta^{\text{ind}}_{k_F,i} \tag{2.23}$$

where $E_{SO} = \alpha k_{F,x}$ and $k_{F,x}$ is the Fermi momentum in the x-direction.

2.2.4 Renormalized Parameters

The parameters $\mu, \alpha, \epsilon, V_x$ are renormalized by a factor of $(1+r)^{-1}$ compared to those of an isolated nanowire as a result of the coupling to the superconductor. Rescaling the fermion fields by $\bar{\Psi}_{k_x,i,m} \to \bar{\Psi}_{k_x,i,m}(1+r_{k_x,i,m})^{-1/2}$, $\Psi_{k_x,i,m} \to \Psi_{k_x,i,m}(1+r_{k_x,i,m})^{-1/2}$ leads to

$$\begin{aligned} S_{\text{eff}} =& \frac{2\pi}{\beta} \sum_{m,i} \int dk_x \bar{\Psi}_{k_x,i,m} \big[-i\omega_m + \tilde{\alpha}_{k_x,i,m} k_x \sigma_y \tau_z \\ &+ \left(\tilde{\epsilon}_{k_x} - \tilde{\mu}_{k_x,i,m}\right) \tau_z + \tilde{V}_{k_x,i,m} \sigma_x - \Delta^{\text{ind}}_{k_x,i,m} \tau_x \big] \Psi_{k_x,i,m} \end{aligned} \tag{2.24}$$

where

$$\tilde{V}_{k_x,i,m} = \frac{V_x}{1+r_{k_x,i,m}}, \quad \tilde{\alpha}_{k_x,i,m} = \frac{\alpha}{1+r_{k_x,i,m}}, \quad \tilde{\mu}_{k_x,i,m} = \frac{\mu - \frac{\hbar^2(\pi i)^2}{2m^* w^2}}{1+r_{k_x,i,m}}. \tag{2.25}$$

It is important to note that both spin-orbit coupling and Zeeman energy are renormalized. As we will see in subsequent sections, the condition to be in a topological phase sets a lower bound $\tilde{V} > \Delta^{\text{ind}}$. The optimum value of r which maximize the quasi-particle gap will depend on various microscopic parameters. From now on, we will assume that the moderate tunneling strength with $r \sim 1$ is the optimum value.

Reduced Zeeman energy would require a larger magnetic field to reach the topological regime. One possible concern is that the larger required magnetic field would destroy superconductivity, but for cuprate superconductors, the critical field is much larger than the field we require for the topological phase transition. As we will see, the induced superconducting gap is typically a few meV which corresponds to the magnetic field of a few Tesla, which will have negligible effect on a high-T_c superconductor.

2.2.5 Majorana Zero Modes

We now discuss the condition for having Majorana zero modes at the end of the wire. For simplicity, we will restrict our analysis to the lowest energy sub-band $i = 1$ and suppress the sub-band index and write $\psi \equiv \psi_{i=1}$. The Hamiltonian of the nanowire can be written in the following form in real space, where all parameters now correspond to their induced values after coupling to the superconductor, described in the previous

section

$$H = \int dx \psi^\dagger_\sigma(x) \left(-\tfrac{\hbar^2 \partial_x^2}{2m^*} - \mu(x) + i\alpha\sigma_y\partial_x + V_x\sigma_x \right) \psi_{\sigma'}(x) + \int dx\, dx' [(\Delta(x,x')\psi^\dagger_\uparrow(x)\psi^\dagger_\downarrow(x') + h.c.]. \tag{2.26}$$

We assume that the nanowire lies along the x-axis for $x < 0$. This condition can be realized by setting $\mu(x < 0) = \mu_0$, and $\mu(x \geq 0) = -\infty$.

Now our Hamiltonian in the Nambu basis $\Psi^\dagger(x) = (\psi^\dagger_\uparrow(x), \psi^\dagger_\downarrow(x), \psi_\downarrow(x), \psi_\uparrow(x))$ can be written as,

$$H = \int dx'\, \Psi^\dagger(x') H_{BdG} \Psi(x)$$

where,

$$H_{BdG} = \int dx \Big[\delta(x-x') \left(-\tfrac{\hbar^2\partial_x^2}{2m^*} - \mu(x) + V_x\sigma_x \right) \tau_z + \delta(x-x') i\alpha\sigma_y\partial_x + \Delta(x,x')\sigma_z\tau_x \Big] \tag{2.27}$$

which gives the following BdG equation for zero energy solution:

$$H_{BdG} \cdot (u_\uparrow(x), u_\downarrow(x), v_\downarrow(x), v_\uparrow(x))^T = 0 \tag{2.28}$$

Since the BdG Hamiltonian is real, we can have real solutions for Majorana zero modes. After imposing particle-hole symmetry for a real solution, we can set $v_{\uparrow/\downarrow}(x) = \lambda u_{\uparrow/\downarrow}(x)$ with $\lambda = \pm 1$. The BdG equation for $E = 0$ can be written as,

$$\int dx' \begin{pmatrix} -\delta(x-x')\left(\frac{\hbar^2\partial_x^2}{2m^*} + \mu_0\right) & V_+(x,x') \\ V_-(x,x') & -\delta(x-x')\left(\frac{\hbar^2\partial_x^2}{2m^*} + \mu_0\right) \end{pmatrix} \times \begin{pmatrix} u_\uparrow(x') \\ u_\downarrow(x') \end{pmatrix} = 0 \tag{2.29}$$

where

$$V_{\pm}(x,x') \equiv V_x\delta(x-x') \pm \lambda\,\Delta(x,x') \pm \alpha\delta(x-x')\partial_x \tag{2.30}$$

with 3 constraints: $[u_{\uparrow/\downarrow}(x=0)]=0$ and normalization. Assuming $u_{\uparrow/\downarrow}(x<0)\propto e^{zx}$, the existence of a zero mode requires at least three roots z_i with positive real part, so that it is normalized and localized at the end $x=0$.

2.3 Induced gap and topological phase transition

In this section, we will analyze the proximity induced gap for three kinds of tunneling amplitudes we discussed in the previous section. We will also study the condition for having MZM at the end of the nanowire.

2.3.1 Clean interface with momentum conserving tunneling

First, let us assume that the interface between the superconductor and the nanowire is uniform, therefore, momentum conserving. For the simplest possible form, $t_i(k_x,\mathbf{q}) = t_i^{\mathrm{u}}(k_x,\mathbf{q})$, we get

$$r_{k_x,i,j,m} = \int \frac{dq_y}{2\pi} \frac{|t|^2\, g_i(q_y) g_j^*(q_y)}{\omega_m^2 + \xi_{k_x,q_y}^2 + \left|\Delta_{k_x,q_y}\right|^2} \tag{2.31}$$

and

$$\Delta'_{k_x,i,j,m} = \int \frac{dq_y}{2\pi} |t|^2\, g_i(q_y) g_j^*(q_y) \times \frac{\frac{\Delta_0}{2}\left(\cos q_x a - \cos q_y a\right)}{\omega_m^2 + \xi_{k_x,q_y}^2 + \left|\Delta_{k_x,q_y}\right|^2} \tag{2.32}$$

Since $g_i(q_y)$ is peaked at $\pm\pi i/w$, the momentum vector (k_x,q_y) in ξ will be far from the Fermi surface of the superconductor for the first few nanowire sub-bands. Therefore, $\Delta'_{k_x,i,j,m}$ will be suppressed by $\xi^2_{k_x,q_y}$. Another interesting aspects of Eq. (2.32) is that the induced gap takes the form of $d-$wave pairing. If we make the approximation $g(q_y) \approx \delta\left(q_y - \frac{\pi a}{w}\right) + \delta\left(q_y + \frac{\pi a}{w}\right)$ following Eq. (2.19), we can approximate

$\Delta(x,x') \approx W_0\left(a^2\partial_x^2 - \left(\frac{\pi a}{w}\right)^2\right)$. The BdG equation can then be written as in Eq. (2.29) with:

$$V_\pm \equiv V_x \pm \lambda W_0\left(a^2\partial_x^2 + \left(\tfrac{\pi a}{w}\right)^2\right) \pm \alpha\partial_x \tag{2.33}$$

Then the BdG equation for zero modes leads to a quartic equation for z with real coefficients.

$$\left(\frac{1}{4}+\tilde{\Delta}^2\right)z^4 + 2\tilde{\Delta}\lambda z^3 + \left(1+\tilde{\mu}+\frac{2\pi^2\tilde{\Delta}^2}{\tilde{w}^2}\right)z^2 + \frac{2\pi^2\lambda\tilde{\Delta}}{\tilde{w}^2}z + \tilde{\mu}^2 - \tilde{V}_x^2 + \frac{\tilde{\Delta}^2\pi^4}{\tilde{w}^4} = 0, \tag{2.34}$$

where $\tilde{x} = \frac{m^*\alpha x}{\hbar^2}$, $\tilde{\mu} = \frac{\hbar^2\mu_0}{m^*\alpha^2}$, $\tilde{V}_x = \frac{\hbar^2 V_x}{m^*\alpha^2}$, $\tilde{\Delta} = \frac{m^*a^2}{\hbar^2}W_0$ and $\tilde{w} = \frac{m^*\alpha}{\hbar^2}w$. Note that when z_is are the roots for $\lambda = 1$ channel, $-z_i$s are the solutions for $\lambda = -1$ channel. Since the coefficients are real, if z_i is solution, z_i^* is also a solution for same channel.

1. When $\tilde{\mu}^2 - \tilde{V}_x^2 + \frac{\tilde{\Delta}^2\pi^4}{\tilde{w}^4} < 0$, there is at least one negative real root and one positive real root. Also, the product of the four roots z_i is $\frac{4(\tilde{\mu}^2-\tilde{V}_x^2+\frac{\tilde{\Delta}^2\pi^4}{\tilde{w}^4})}{1+4\tilde{\Delta}^2} < 0$. When all roots are real, we have three positive roots for either $\lambda = 1$ or $\lambda = -1$. When two of the roots are complex, then the four roots can be written $z_1 > 0$, $z_2 < 0$, $z_3 = a + bi$ and $z_4 = a - bi$, and we again have three roots with positive real part for either $\lambda = 1$ or $\lambda = -1$. Therefore, we have a Majorana zero mode in this case.

2. When $\tilde{\mu}^2 - \tilde{V}_x^2 + \frac{\tilde{\Delta}^2\pi^4}{\tilde{w}^4} > 0$ and all four roots are real, there are two different cases. When two of them are positive and two of them are negative, we do not have localized solution for zero energy. When all four roots have same sign (which is positive for either $\lambda = 1$ or $\lambda = -1$), we have two zero modes at the end of nanowire. However these two localized states are at the same end, and they will split into two states with $E > 0$ and $E < 0$ by interaction.

3. When $\tilde{\mu}^2 - \tilde{V}_x^2 + \frac{\tilde{\Delta}^2\pi^4}{\tilde{w}^4} > 0$, and two roots are complex, the other two roots, if they

are real, will have same sign since $\prod_{i=1}^{4} z_i > 0$. If the other two roots are also complex, those two also have same real part. Then it is similar to case 2.

We do not consider the situation in which the above equation has a double root or two purely imaginary solutions in case 1 since those cases are sets of measure zero in parameter space. Therefore, the condition for having MZM is $\tilde{\mu}^2 - \tilde{V}_x^2 + \frac{\tilde{\Delta}^2\pi^4}{\tilde{w}^4} < 0$. We can also extend this analysis to the nth sub-band where $k_y = n\pi/w$, and the condition for topological phase is given as $\tilde{\mu}_n^2 - \tilde{V}_x^2 + \frac{\tilde{\Delta}^2 n^4\pi^4}{\tilde{w}^4} < 0$.

2.3.2 Dirty or Rough Interface

We now consider the case of a dirty or rough interface. In the extreme case introduced in Section 2.2.2, Eq. (2.12) becomes

$$\Delta'_{k,m} = \int \frac{d^2\mathbf{q}}{(2\pi)^2} \frac{|\lambda(\mathbf{q})|^2 \, \Delta_q}{\omega_m^2 + \xi_q^2 + |\Delta_q|^2}$$

The right-hand-side is independent of k. Moreover, since Δ_q is odd under rotation by $\pi/2$ while the rest of the integrand is even, the right-hand-side vanishes after integration, and there will be no induced gap.

2.3.3 Nanowire - Step Edge Interface

From the previous two cases we found the limitations for inducing superconducting gap using the cuprate superconductors. To overcome the limitations, we have to consider a scenario in which the tunneling amplitude breaks the rotation symmetry while the constraint for the momentum conservation is relaxed. For example, one can consider a situation in which the nanowire is on top of a step edge surface of a cuprate, as shown in Figure 2.1. For simplicity, we assume that the terraces are evenly spaced so that the

terrace edges are at $x_n = nl$. In the clean limit, the tunneling amplitude is dominant at the terrace edges, x_n. We assume the tunneling matrix element $t_i(k_x, \mathbf{q}) = t_i^{\mathrm{s}}(k_x, \mathbf{q})$ discussed in Sec II. For small angle $\theta \sim 10^\circ$, we can approximate $\cos\theta \sim 1$, and

$$\Delta'_{k_x,k'_x,i,j,m} = \sum_{n_1,n_2} \int \frac{d^2\mathbf{q}}{(2\pi)^2} |t|^2 \delta(k_x - q_x + n_1 Q)\delta(k'_x - q_x + n_2 Q) \frac{g_i(q_y) g_j^*(q_y) \Delta_q}{\omega_m^2 + \xi_q^2 + |\Delta_q|^2} \quad (2.35)$$

For typical semiconducting nanowires, $k_F << Q$, and we can ignore the contributions from $k_x = k'_x + (n_2 - n_1)Q$ with $n_1 \neq n_2$. Integrating over k'_x leads to

$$\Delta'_{k_x,i,j,m} = \sum_n \int \frac{dq_y}{2\pi} |t|^2 g_i(q_y) g_j^*(q_y) \frac{\Delta_{k_x+nQ,q_y}}{\omega_m^2 + \xi_{k_x+nQ,q_y}^2 + \left|\Delta_{k_x+nQ,q_y}\right|^2} \quad (2.36)$$

and

$$r_{k_x,i,j,m} = \sum_n \int \frac{dq_y}{2\pi} \frac{|t|^2 g_i(q_y) g_j^*(q_y)}{\omega_m^2 + \xi_{k_x+nQ,q_y}^2 + \left|\Delta_{k_x+nQ,q_y}\right|^2} \quad (2.37)$$

with $k_x + nQ \in$ first B.Z. In the limit of small inter-band coupling, the induced gap for each sub-band is given by

$$\Delta_{k_F,i}^{ind} = \frac{\Delta'_{k_F,i,0}}{1 + r_{k_F,i,0}}. \quad (2.38)$$

It is now possible for $(k_x + nQ, q_y)$ to be located close to the Fermi surface of the cuprate superconductor, so the suppression by ξ^2 in the denominator is weaker for some ns than $n = 0$ as we can see from Fig. 2.2.

To estimate the size of the induced gap in each band, we take $\mu_5 = 10$meV and $V_x = 30$meV for a nanowire of width $w = 50$nm. We used the typical values $\alpha = 200\,\mathrm{meV{\cdot}\AA}$ and $m^* = 0.015 m_e$ for InSb nanowire. We find $r_{k_x,i,j,m}$ is almost constant in k_x and diagonal in sub-band index (i, j) at $T = 0$. Choosing $t = 60$meV gives $r_i \sim 0.7$. We find the induced gap for each sub-band is very weakly-dependent on k_x, therefore, it is similar to the $s-$wave pairing. For $V_x = 30$ meV, which corresponds to the value in the

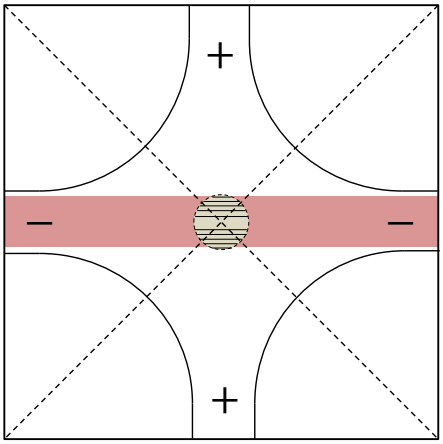

Figure 2.2: Fermi surface of an interface between a semiconductor nanowire and a step-edge of a cuprate. Now induced superconducting gap gets contributions from the colored area.

topological phase, this gives $\Delta^{\text{qp}} = 0.8\text{meV}$. In reality, tunneling will not be perfectly momentum-conserving modulo Q. However, the basic result should still be valid: if momentum non-conservation is much larger in one direction than the other then a large gap can be induced.

We now consider Majorana zero modes at the end of the wire. Since the induced gap is independent of k_x, the characteristic equation for z takes the simple form:

$$\frac{1}{4}z^4 + \left(\tilde{\mu}_i + \tilde{\alpha}^2\right) z^2 - 2\lambda\tilde{\Delta}_i\tilde{\alpha}z + \tilde{\mu}_i^2 - \tilde{V}_x^2 + \tilde{\Delta}_i^2 = 0. \tag{2.39}$$

The condition for the MZM is $\tilde{\mu}_i^2 - \tilde{V}_x^2 + \tilde{\Delta}_i^2 < 0$.[54]

2.4 Coupling between the Majorana zero mode and gapless bulk excitations

Cuprate superconductors with d-wave pairing symmetry can have four gapless nodes in the two-dimensional Brillouin zone. Thus far, we have ignored these low-energy excitations because the tunneling matrix elements $t(k_x, \mathbf{q})$ that we used did not couple electrons in the nanowire to these nodal excitations so long as the tunneling matrix conserves the momentum in $x-$direction. For a localized state, however, one can have some coupling to the nodal excitations in the superconductor. In this section, we add a tunneling term to the action coupling the Majorana zero mode to the superconductor and calculate the self-energy of the Majorana mode perturbatively to analyze its stability.

The tunneling between the MZM from the j^{th} sub-band at $x = 0$ to the fermionic excitations in the superconductor can be described by

$$\begin{aligned} S_T^{\gamma_j} &= \sum_m \int_{-\infty}^{0} dx \int_0^w dy \int d^2\mathbf{r}' v(\mathbf{r}, \mathbf{r}') \gamma_{m,j}(\mathbf{r}) \left[c^\sigma_{-m}(\mathbf{r}') - \bar{c}^\sigma_{-m}(\mathbf{r}') \right] \\ &= \int_{\mathbf{k}} v_{\gamma_j}(\mathbf{k})\, \gamma_j(\omega_m) \left[c^\sigma_{-m,-\mathbf{k}} - \bar{c}^\sigma_{-m,-\mathbf{k}} \right] \end{aligned} \tag{2.40}$$

where $v(\mathbf{r}, \mathbf{r}')$ is the tunneling amplitude between MZM at position r and fermionic excitation at r' in the superconductor. We take $v(\mathbf{r}, \mathbf{r}')$ to be real. On the superconductor operators we have explicitly written the spin superscript σ. In going from the first to the second equality, we have assumed a simplified form for the real Majorana zero mode:

$$\gamma_j(\omega_m, \mathbf{r}) = 2\sqrt{\frac{z}{w}} \sin\left(\frac{\pi j y}{w}\right) \Theta(-x) e^{zx} \gamma_j(\omega_m) \tag{2.41}$$

and the Fourier transform $v_{\gamma_j}(\mathbf{k})$

$$v_{\gamma_j}(\mathbf{k}) = 2\sqrt{\frac{z}{w}} \int_{-\infty}^{0} dx \int_{0}^{w} dy \int d^2\mathbf{r}'\, v(\mathbf{r},\mathbf{r}') \sin\left(\frac{\pi j y}{w}\right) e^{zx + i\mathbf{k}\cdot\mathbf{r}'} \tag{2.42}$$

Plugging in the tunneling amplitudes for clean interface and step edge interface leads to

$$v^u_{\gamma_j}(\mathbf{k}) = \frac{t\sqrt{z} g_j(-k_y)}{z + ik_x} \tag{2.43}$$

$$v^s_{\gamma_j}(\mathbf{k}) = \frac{td\sqrt{z} g_j(-k_y)}{1 - e^{-(z+ik_x\cos\theta)l}} \tag{2.44}$$

Now the self energy $\Sigma_{\gamma_j\gamma_j}(\omega_m)$ of the Majorana modes can be calculated as

$$\begin{aligned}\Sigma_{\gamma_j\gamma_j}(\omega_m) =& \int d^2\mathbf{k}\, \left|v_{\gamma_j}(\mathbf{k})\right|^2 \left[\left\langle c^{\sigma}_{\omega,\mathbf{k}} c^{\sigma'}_{-\omega,-\mathbf{k}}\right\rangle + \left\langle \bar{c}^{\sigma}_{\omega,-\mathbf{k}} \bar{c}^{\sigma'}_{-\omega,\mathbf{k}}\right\rangle - \left\langle \bar{c}^{\sigma}_{\omega,-\mathbf{k}} c^{\sigma'}_{-\omega,\mathbf{k}}\right\rangle - \left\langle c^{\sigma}_{\omega,\mathbf{k}} \bar{c}^{\sigma'}_{-\omega,-\mathbf{k}}\right\rangle\right] \\ =& 2\int d^2\mathbf{k} \frac{\left|v_{\gamma_j}(\mathbf{k})\right|^2 (\Delta_k + i\omega_m)}{\omega_m^2 + \xi_k^2 + \Delta_k^2}\end{aligned} \tag{2.45}$$

For simplicity, we take ξ_k to be of the form $\xi_k = t_1(\cos k_x a + \cos k_y a)/2 + t_2 \cos k_x a \cos k_y a$ and $\Delta_k = \Delta_0(\cos k_x a - \cos k_y a)$. Then, we obtain the retarded self-energy from the analytic continuation, $i\omega_m \to \omega + i\eta$. Using the identity $\lim_{\eta\to 0+} \frac{1}{(x+i\eta)} = P(\frac{1}{x}) - i\pi\delta(x)$, we obtain

$$\mathrm{Im}\Sigma^{\gamma\gamma}_r(\omega) = 2\int_{\mathbf{k}\in\mathbf{k}_0} \left|v_{\gamma_j}(\mathbf{k})\right|^2 (\omega + \Delta_k) \left|\nabla_k(\xi_k^2 + \Delta_k^2)\right|^{-1} \tag{2.46}$$

where $\mathbf{k}_0$ satisfies $\omega^2 = \xi^2_{k_0} + \Delta^2_{k_0}$, and

$$\mathrm{Re}\Sigma^{\gamma\gamma}_r(\omega) = \lim_{\eta\to 0} 2\int d^2\mathbf{k}\, \left|v_{\gamma_j}(\mathbf{k})\right|^2 \frac{(\Delta_k + \omega)(\xi_k^2 + \Delta_k^2 - \omega^2)}{(\omega^2 - \xi_k^2 - \Delta_k^2)^2 + \eta^2} \tag{2.47}$$

From here on, Δ_k disappears from the numerator because it is odd under exchange of k_x and k_y, while all other terms are even. We now explicitly calculate the real and imaginary parts.

2.4.1 Imaginary Part of Self Energy

For small ω, the dominant contribution to Eq. (2.46) comes from momenta near the nodes, which we denote by overbars: $(\pm\bar{k}_x, \pm\bar{k}_y)$. We expand the momenta around the nodal point $(\bar{k}_x, \bar{k}_y)$ as $(k_x, k_y) = (\bar{k}_x + p + q, \bar{k}_y + p - q)$ and expand similarly around the three other nodal points. Expanding ξ_k and Δ_k about the nodal points yields $\xi_k = c_1 p$ and $\Delta_k = c_2 q$, where $c_1 = -t_1 a \sin \bar{k}_x a - 2t_2 a \sin \bar{k}_x a \cos \bar{k}_y a$ and $c_2 = 2\Delta_0 a \sin \bar{k}_x a$. Now the condition $\mathbf{k} \in \mathbf{k}_0$ is given by $\omega^2 = c_1 p^2 + c_2 q^2$. We also take the average value for the tunneling strengths:

$$v^u_{\gamma_j}(\mathbf{k}) = \frac{t\sqrt{z} g_j(-\bar{k}_y)}{z + i\bar{k}_x} = v^u \tag{2.48}$$

$$v^s_{\gamma_j}(\mathbf{k}) = \frac{td\sqrt{z} g_j(-\bar{k}_y)}{1 - e^{-(z + i\bar{k}_x \cos\theta)l}} = v^s \tag{2.49}$$

Note that

$$|v^u|^2 \propto a^4 z/w\,, \qquad |v^s|^2 \propto a^2 d^2 z/w \tag{2.50}$$

are small because $100 < w/a < 250$. In addition, $d \sim a$ and $1/z \gg a$, which further suppresses these tunneling parameters. The cases of uniform tunneling and a step-edge interface can be handled together:

$$\mathrm{Im}\Sigma^{\gamma\gamma}_r(\omega) = \frac{|v^{u,s}|^2}{\sqrt{2}} \omega \int_{\mathbf{k}\in\mathbf{k}_0} \frac{1}{\sqrt{c_1^4 p^2 + c_2^4 q^2}} \tag{2.51}$$

A simple change of variables yields the decay rate $\Gamma(\omega)$ to leading order:

$$\Gamma^{u,s}(\omega) \propto \left(\frac{s}{w}\right) \frac{\omega}{\Delta_0} \frac{|t|^2}{\alpha t_1 + \beta t_2} \tag{2.52}$$

where α and β are dimensionless numbers, and $s = a^2 z$ or $d^2 z$ in the cases of uniform and step-edge tunneling, respectively. In both cases, the decay rate is suppressed by a

small coefficient.

2.4.2 Real Part of Self Energy

The real part of the self-energy follows similarly:

$$\begin{aligned} Re\Sigma_r^{\gamma\gamma}(\omega) &= \lim_{\eta\to 0} 2\int dpdq\,|v^{u,s}|^2\,\frac{\omega(c_1^2p^2+c_2^2q^2-\omega^2)}{(c_1^2p^2+c_2^2q^2-\omega^2)^2+\eta^2} \\ &= -\frac{2\,|v^{u,s}|^2\,\omega}{|c_1c_2|}\ln(\omega/\sqrt{\Lambda^2-\omega^2}) \end{aligned} \tag{2.53}$$

where we introduced UV cut-off Λ. Hence, in the low frequency limit, the correction is singular. The weight of the would-be quasiparticle pole $Z = (1 - \partial\mathrm{Re}\Sigma/\partial\omega)^{-1}$ vanishes logarithmically as zero energy is approached. This indicates that the zero mode does not survive the coupling to nodal excitations, and it will leak into the bulk of the cuprate superconductor. However, the divergence is only logarithmic due to the little phase space at the nodes, so this leakage occurs very slowly.

2.5 Discussion

In this chapter we have studied the semiconducting nanowire-cuprate superconductor interface as a platform for topological superconductivity. Due to the $d-$wave structure of the pairing potential of the cuprate superconductor, it requires special consideration for the interface geometry to induce a superconducting gap in the nanowire. Clean interface with momentum conserving tunneling can give a non-zero induced gap, and it can be optimized when the direction of the nanowire is aligned to (100) or (010) crystallographic direction of the underlying cuprate superconductor. However, the proximity effect is suppressed by the momentum mismatch between the electrons in the nanowire and the cuprate superconductor. One can overcome this by allowing the momentum mismatched

tunneling in only one direction. We show that the step-like terrace surface can be used to create such a scenario.

The coupling between MZM and gapless nodal excitation can cause MZM to decay into the cuprate superconductor. Especially, the real part of the Majorana propagator self-energy shows an infrared divergence which leads to the zero spectral weight of the MZM. However, this divergence has a logarithmic nature due to the vanishing density of states of the gapless excitations. Therefore, one can still expect to observe the signatures of MZM in real experiments at finite temperature.

Chapter 3

Realization of topological superconductors using magnetic atom chains

In this chapter, we study the realization of topological superconductivity from the Yu-Shiba-Rusinov(YSR) states in chains of magnetic adatoms at the surface of s-wave superconductors with strong spin-orbit coupling. We first review the recent development of the theoretical proposal and current status of the experiment on this system. Then, we expand the single orbital Shiba state model into multiple orbitals and study the effect of spin-orbit coupling. Finally, we discuss the multi-channel extension of the YSR chain.

3.1 Introduction

Magnetic impurity in an s-wave superconductor can induce Yu-Shiba-Rusinov (YSR) states [95, 87, 80] which are locally bounded to the impurity. Recently, one dimensional arrays of magnetic impurities and their YSR states in the s-wave superconductor have gained a significant interest because of its possibility to realize topological superconductivity and Majorana zero modes. [12, 61, 46, 8, 92, 72, 73, 75, 41, 9, 25, 49, 93, 71, 35] When a one dimensional array of well separated magnetic atoms is placed at the surface of a superconductor, YSR states of each atoms can be coupled to each other through the superconductor and form YSR band of electronic states. When the magnetic moments of the atoms form a helical order [61, 46, 8, 92, 72] or the sub-lying superconductor has Rashba spin-orbit coupling [41, 9, 35], superconducting gap can be induced to the band. Since each one of YSR states is spin-polarized, this YSR band with induced gap can be mapped into a spinless p-wave superconductor and support MZM at the ends of the chain. For magnetic adatom chains with atomic scale separation between the magnetic atoms, the direct hopping between them leads to the formation of a ferromagnetic half-metal. In this case, the superconductor with strong spin-orbit coupling can also induce p-wave pairing in the half-metal, and the system can be in the topological phase. [49, 37, 23] Later, it is shown that these two scenarios are indeed adiabatically connected from studying single-orbital Anderson model. [71] In recent experiments [62, 70, 79], Fe atom chains formed at the surface of Pb superconductor have been studied using various types of scanning tunneling microscopy (STM) which can resolve the local density of electronic states. It is shown that these Fe atom chains exhibit zero-energy states which are strongly localized at the ends. Measurement with magnetized STM tip [62] reveals the ferromagnetic ordering of the magnetic moments of the Fe atoms. More interestingly, high-resolution study with superconducting tip on the single Fe atom and dipole of Fe

atoms found multiple YSR states bounded to them. [79] Indeed, previous study on Mn and Cr atoms on Pb superconductor surface using high resolution STM study [38] have found such multiple YSR states. This multiplet structure can be understood as eigenstates of various angular momentum components of the exchange potential [80, 41] or multiple orbitals of the magnetic atom coupled to the environment [59]. In half-metal formalism, electronic states from a chain of such atoms can be naturally connected to the multiple $d-$orbital bands. However, most of the previous theoretical studies based on YSR band formalism are assuming single YSR state per atom. Therefore, it is important to consider an extension to multiple YSR bands system[98] from multiple YSR states per atom as a dilute limit of the realistic system.

In what follows, we first deveplop a general formalism to understand the properties of YSR multiplets in two dimensional superconductor with broken inversion symmetry. We consider a signle atom and a dimer of atoms coupled to either $s-$wave or $p-$wave superconductors in the presence of Rashba SOC. We show that Rahsba SOC qualitatively modifies the YSR spectrum when higher angular momentum channels of the exchange potential is included. For YSR states bounded to a single atom, the YSR spectrum has a non-trivial dependence on the direction of the spin when we include SOC. For a dimer, level splitting is a function of the relative direction of the two spins, and Rashba SOC also modifies this relation. We discuss the experimental signatures of those features. Then, we extend our theory to a chain of magnetic atoms with multiple angular momentum channel YSR states. We consider the simplest non-trival case with three angular momentum channels per atom which leads to a theory with three YSR bands. We study the phase diagram of the system in dilute atom limits where the bandwidth of the YSR bands are much smaller than the size of the superconducting gap of the host and level splittings between YSR states. Finally, we discuss the effects of the band mixing due to the spin-orbit coupling and their implications on experiments.

3.2 Yu-Shiba-Rusinov multiplets in superconductors with spin-orbit coupling

In this section, we study the spectrum of YSR states bounded to a magnetic impurity in two-dimensional superconductors with broken inversion symmetry in which spin-triplet pairing and Rashba spin-orbit coupling are present. We assume a generic form for the exchange potential $J(\mathbf{r})$ of a magnetic impurity which is a function of $|\mathbf{r}|$ and preserves rotational symmetry. We develop a formalism to understand the structure of YSR states. Then, we discuss the effects of Rashba SOC on the YSR spectrum and their experimental significance.

3.2.1 Model

We consider a superconductor described by the mean-field Hamiltonian

$$\mathcal{H} = \sum_{\mathbf{k}} \psi_{\mathbf{k}}^{\dagger} H_{\mathrm{SC}}(\mathbf{k}) \psi_{\mathbf{k}} \tag{3.1}$$

where $\psi_{\mathbf{k}} = (c_{\mathbf{k}\uparrow}, c_{\mathbf{k}\downarrow}, c_{-\mathbf{k}\downarrow}^{\dagger}, -c_{-\mathbf{k}\uparrow}^{\dagger})^T$, with $c_{\mathbf{k}\sigma}^{\dagger}$ ($c_{\mathbf{k}\sigma}$) the creation(annihilation) operator for an electron with momentum $\mathbf{k} = (k_x, k_y)$ and spin σ, and

$$H_{\mathrm{SC}}(\mathbf{k}) = \tau_z \otimes (\xi_{\mathbf{k}} + \alpha \mathbf{l}_{\mathbf{k}} \cdot \boldsymbol{\sigma}) + \tau_x \otimes (\Delta_s + \frac{\Delta_t}{k_F} \mathbf{l}_{\mathbf{k}} \cdot \boldsymbol{\sigma}). \tag{3.2}$$

$\mathcal{H}$ describes effectively two-dimensional superconducting thin films, and surfaces of 3D superconductors with strong Rashba SOC. In Eq. (3.2) we set $\hbar = 1$, τ_j, σ_i are the Pauli matrices in Nambu and spin space respectively, $\xi_{\mathbf{k}} = k^2/2m - \epsilon_F$ which is assumed to be the normal state dispersion relation with m being the effective mass of the fermionic quasiparticles. ϵ_F and $k_F = \sqrt{2m\epsilon_F}$ are the Fermi energy and Fermi momentum, re-

spectively, $\mathbf{l_k} = (k_y, -k_x)$[28], α is the strength of the Rashba SOC, and Δ_s, Δ_t are the singlet, triplet, pairing order parameters respectively, that, without loss of generality, we take to be real.

The effect of magnetic impurity in the system can be captured by the following Hamiltonian.

$$H_{\text{imp}} = \sum_j \hat{V}_j(|\mathbf{r} - \mathbf{R}_j|) = \sum_j \hat{U}(|\mathbf{r} - \mathbf{R}_j|)\tau_z \otimes \sigma_0 + \hat{J}(|\mathbf{r} - \mathbf{R}_j|)\tau_0 \otimes \mathbf{S}_j \cdot \boldsymbol{\sigma} \tag{3.3}$$

$\mathbf{R}_i$s are the positions of the impurities, and $\hat{U}$ and $\hat{J}$ are the charge and magnetic potential respectively. Without loss of generality, we set $\mathbf{R} = 0$ for single impurity and $\mathbf{R}_i = x_i$ for dimer. The presence of scalar potential $\hat{U}$ does not affect the qualitative nature of the conclusion. Therefore, we will set $\hat{U} = 0$ from now on. For the details on the effect of scalar potential, please refer to the supplementary materials for Ref. [42]. Using the density of states (per spin) $N_F = m/2\pi$, and the Fermi velocity $v_F = k_F/m$, we can define the dimensionless potential $J \equiv \hat{J}\pi N_F|\mathbf{S}|$ and the dimensionless Rashba SOC $\tilde{\alpha} \equiv \alpha/v_F$ which are used for the rest of the discussion.

To find the eigenstate energies $\{E\}$ of YSR states we have to solve the Schrödinger equation

$$(H_{\text{SC}} + H_{\text{imp}})\psi(\mathbf{r}) = E\psi(\mathbf{r}). \tag{3.4}$$

We define $G = [E - H_{\text{SC}}]^{-1}$, then the Schrödinger equation can be written as

$$[1 - G(E, \mathbf{r})H_{\text{imp}}]\psi(\mathbf{r}) = 0. \tag{3.5}$$

The spectrum of the impurity bound states is obtained by finding the values of E such that $\det[1 - G(E, \mathbf{r})H_{\text{imp}}] = 0$. In momentum space the Schrödinger equation takes the

form:

$$\psi(\mathbf{k}) = \sum_j G(E,\mathbf{k}) \int d\mathbf{k}' e^{ix_j(k\cos\theta - k'\cos\theta')} \hat{V}_j(|\mathbf{k}-\mathbf{k}'|)\psi(\mathbf{k}'). \tag{3.6}$$

Following the formalism of Ref. [34], the Green's function G can be written as the sum $(G(E,\mathbf{k}) = [G^+(E,\mathbf{k}) + G^-(E,\mathbf{k})]/2)$ of the two spin helical bands

$$G^{\pm}(E,\mathbf{k}) = \begin{pmatrix} E+\xi_\pm & \tilde{\Delta}_\pm \\ \tilde{\Delta}_\pm & E-\xi_\pm \end{pmatrix} \otimes \frac{\sigma_0 \pm \sin\theta\sigma_x \mp \cos\theta\sigma_y}{E^2 - \xi_\pm^2 - \Delta_\pm^2}. \tag{3.7}$$

Here $k = |\mathbf{k}|$, $\xi_\pm = k^2/2m \pm \alpha k - \epsilon_F$ and $\Delta_\pm = \Delta_s \pm \Delta_t k/k_F$. Let us define

$$\overline{\psi_{j,\theta}} \equiv \int \frac{kdk}{2\pi} e^{-ix_j k\cos\theta} \psi(\mathbf{k}), \tag{3.8}$$

$$\overline{G^{ij}(E,\theta)} \equiv \int \frac{kdk}{2\pi} e^{-i(x_i - x_j)k\cos\theta} G(E,\mathbf{k}). \tag{3.9}$$

Assuming that $\hat{V}(\mathbf{k})$ at the Fermi surface depends weakly on k and integrating Eq. (3.6) with respect to k, we find

$$\overline{\psi_i(\theta)} = \sum_j \overline{\hat{G}^{ij}(E,\theta)} \frac{1}{2\pi} \int d\theta' \hat{V}_j(\theta-\theta') \overline{\psi_j(\theta')}. \tag{3.10}$$

The above equation can be simplified by decomposing all the functions of angle that enter Eq. (3.10) into their angular momentum components: $f(\theta) = \sum_l f_l e^{il\theta}$. Finally, we get

$$\overline{\psi_{i,l}} - \sum_{j,n} \overline{G_n^{ij}(E)} \hat{V}_j^{l-n} \overline{\psi_{j,l-n}} = 0, \tag{3.11}$$

where

$$\hat{V}_j^l = \begin{pmatrix} J_l \frac{\mathbf{S_j}\cdot\boldsymbol{\sigma}}{|\mathbf{S_j}|} & 0 \\ 0 & J_{-l} \frac{\mathbf{S_j}\cdot\boldsymbol{\sigma}}{|\mathbf{S_j}|} \end{pmatrix}. \tag{3.12}$$

Since $H_{\rm imp}$ is Hermitian and even with respect to $\theta - \theta'$, we require $J_l (= J_{-l})$ to be real.

From now on we set $S = 1$ for the simplicity of expression. The angular momentum components of the local Gorkov-Rashba Green's function can be easily calculated.

$$\overline{\hat{G}_0^{ii}(E)} = -\frac{\pi N_-}{2\sqrt{\Delta_+^2 - E^2}} \begin{pmatrix} E & 0 & \Delta_+ & 0 \\ 0 & E & 0 & \Delta_+ \\ \Delta_+ & 0 & E & 0 \\ 0 & \Delta_+ & 0 & E \end{pmatrix} - \frac{\pi N_+}{2\sqrt{\Delta_-^2 - E^2}} \begin{pmatrix} E & 0 & \Delta_- & 0 \\ 0 & E & 0 & \Delta_- \\ \Delta_- & 0 & E & 0 \\ 0 & \Delta_- & 0 & E \end{pmatrix},$$

$$\overline{\hat{G}_1^{ii}(E)} = -\frac{\pi N_-}{2\sqrt{\Delta_+^2 - E^2}} \begin{pmatrix} 0 & 0 & 0 & 0 \\ -iE & 0 & -i\Delta_+ & 0 \\ 0 & 0 & 0 & 0 \\ -i\Delta_+ & 0 & -iE & 0 \end{pmatrix} + \frac{\pi N_+}{2\sqrt{\Delta_-^2 - E^2}} \begin{pmatrix} 0 & 0 & 0 & 0 \\ -iE & 0 & -i\Delta_- & 0 \\ 0 & 0 & 0 & 0 \\ -i\Delta_- & 0 & -iE & 0 \end{pmatrix},$$

$$\overline{\hat{G}_{-1}^{ii}(E)} = -\frac{\pi N_-}{2\sqrt{\Delta_+^2 - E^2}} \begin{pmatrix} 0 & iE & 0 & i\Delta_+ \\ 0 & 0 & 0 & 0 \\ 0 & i\Delta_+ & 0 & iE \\ 0 & 0 & 0 & 0 \end{pmatrix} + \frac{\pi N_+}{2\sqrt{\Delta_-^2 - E^2}} \begin{pmatrix} 0 & iE & 0 & i\Delta_- \\ 0 & 0 & 0 & 0 \\ 0 & i\Delta_- & 0 & iE \\ 0 & 0 & 0 & 0 \end{pmatrix}. \quad (3.13)$$

where

$$N_\pm = \frac{m}{2\pi}\left(1 \pm \frac{\tilde{\alpha}}{\sqrt{1+\tilde{\alpha}^2}}\right), \quad \Delta_\pm = \Delta_s \pm \Delta_t. \quad (3.14)$$

Note that $\overline{G_n^{ii}} = (\overline{G_n^+(E)} + \overline{G_n^-(E)})/2 = 0$ for $|n| \geq 2$. For the calculation of non-local Green's function $\overline{G_n^{i\neq j}}$, please see Appendix A.1. Henceforth, we assume that the impurity potential has only large $l = 0, 1$ components and neglect higher angular momentum channels.

We consider two different phases of a $H_{\rm SC}$ [81, 91, 82]: $s-$wave ($|\Delta_s| \gg |\Delta_t|$) and $p-$wave ($|\Delta_s| \ll |\Delta_t|$) pairing dominating regimes. As we show below, the spectra are qualitatively different in the two regimes. For the simplicity of the analysis, we will set $\Delta_t = 0$ for $s-$wave dominating regime and $\Delta_s = 0$ for $p-$wave dominating regime.

3.2.2 Single magnetic atom

For a single atom, we can drop the site index i such that $\overline{\psi_{i,l}} = \overline{\psi_l}$. When we assume that $J_{l=-1,0,1}$ are the only non-zero components, Eq. (3.11) can be explicitly written as.

$$\begin{aligned}
\overline{\psi_0} &= \overline{\hat{G}_0(E)}\hat{V}^0\overline{\psi_0} + \overline{\hat{G}_1(E)}\hat{V}^{-1}\overline{\psi_{-1}} + \overline{\hat{G}_{-1}(E)}\hat{V}^1\overline{\psi_1} \\
\overline{\psi_1} &= \overline{\hat{G}_0(E)}\hat{V}^1\overline{\psi_1} + \overline{\hat{G}_1(E)}\hat{V}^0\overline{\psi_0} \\
\overline{\psi_{-1}} &= \overline{\hat{G}_0(E)}\hat{V}^{-1}\overline{\psi_{-1}} + \overline{\hat{G}_{-1}(E)}\hat{V}^0\overline{\psi_0} \\
\overline{\psi_2} &= \overline{\hat{G}_1(E)}\hat{V}^1\overline{\psi_1} \\
\overline{\psi_{-2}} &= \overline{\hat{G}_{-1}(E)}\hat{V}^{-1}\overline{\psi_{-1}}
\end{aligned} \tag{3.15}$$

For a bound state solution to exist for the above equation, following condition is required,

$$\det \begin{bmatrix} \overline{\hat{G}_0(E)}\hat{V}^{-1} - 1 & \overline{\hat{G}_{-1}(E)}\hat{V}^0 & 0 \\ \overline{\hat{G}_1(E)}\hat{V}^{-1} & \overline{\hat{G}_0(E)}\hat{V}^0 - 1 & \overline{\hat{G}_{-1}(E)}\hat{V}^1 \\ 0 & \overline{\hat{G}_1(E)}\hat{V}^0 & \overline{\hat{G}_0(E)}\hat{V}^1 - 1 \end{bmatrix} = 0. \tag{3.16}$$

We solve the above equations in both analytic and numeric ways to get the bound state spectrum. For an s-wave superconductor, we find that, in the presence of Rashba spin-orbit coupling, we have three impurity-induced bound states at $E > 0$. In general, there are one bound state for $J_{l=0}$ and two bound states per each pair of non-zero $J_{\pm l}$. For the case when the magnetic moment of the impurity is perpendicular to the surface of the superconductor, $\mathbf{S} \parallel \hat{z}$, the energies of these states are given by

$$\frac{|E_{1,2}|}{\Delta_s} = \frac{\gamma^2 - J_0^2 J_1^2 \pm \gamma^{\frac{3}{2}}\sqrt{(J_0^2 - J_1^2)^2 + (\gamma-1)(J_0 - J_1)^4}}{\gamma^2(1+(J_0-J_1)^2) + 2\gamma J_0 J_1 + J_0^2 J_1^2} \tag{3.17}$$

$$\frac{|E_3|}{\Delta_s} = \frac{1 - J_1^2}{1 + J_1^2} \tag{3.18}$$

where $\gamma = 1 + \tilde{\alpha}^2$. For $\tilde{\alpha} = 0$, two of the states which correspond to $l = \pm 1$ levels are degenerate due to the rotational symmetry of the Hamiltonian. The presence of SOC, however, causes the $l = \pm 1$ levels to split, see Fig. 3.1 (a). Interestingly, we find that only two of the levels disperse with α and one level remains unchanged.

An important consequence of the presence of the SOC in s-wave SCs is that, by breaking the SU(2) symmetry of the SC Hamiltonian, it causes the spectrum of the YSR states to strongly depend on the direction of $\mathbf{S} = (\cos\phi \sin\theta, \sin\phi \sin\theta, \cos\theta)$. Fig. 3.2 (a) shows an example of the evolution of the spectrum of the YSR states with θ for an s-wave SC. (Due to the remaining U(1) symmetry the spectrum does not depend on the in-plane direction, i.e. ϕ). We see that, the spectrum for the case in which $\mathbf{S} \parallel \hat{z}$ can be very different from the spectrum for the case in which $\mathbf{S}$ lies in the plane. In particular the results of Fig. 3.2 (a) show that by tuning the direction of $\mathbf{S}$ the fermion parity of the bound states can be changed.

For a chain of magnetic atoms, this feature could be very useful to tune between topological and non-topological regimes in the YSR-bands. We will revisit this effect in the next section. In the limit $\tilde{\alpha} \ll \min\{1, |J_0 - J_1|\}$ we can obtain analytic expression for the dependence of the YSR energy levels on the direction of $\mathbf{S}$ in an s-wave SC:

$$\frac{|E_1|}{\Delta_s} \approx \frac{1-J_0^2}{1+J_0^2} + \frac{4\tilde{\alpha}^2 J_0^2 J_1 (J_0 \cos^2\theta - J_1)}{(1+J_0^2)^2 (J_0^2 - J_1^2)} \tag{3.19}$$

$$\frac{|E_{2,3}|}{\Delta_s} \approx \frac{1-J_1^2}{1+J_1^2} + \frac{2\tilde{\alpha}^2 J_0 J_1^2 (J_0 - J_1 \cos^2\theta \pm F(\theta))}{(1+J_1^2)^2 (J_0^2 - J_1^2)} \tag{3.20}$$

$$F_1 = \sqrt{(J_0 - J_1)^2 \cos^2\theta + J_1^2 \sin^4\theta} \tag{3.21}$$

Here we keep only lowest order terms $\tilde{\alpha}$. These expressions are valid as long as the hybridized states are not degenerate. The above result allows us to identify the effect of the interplay of SOC, relative strength of the different components of the magnetic

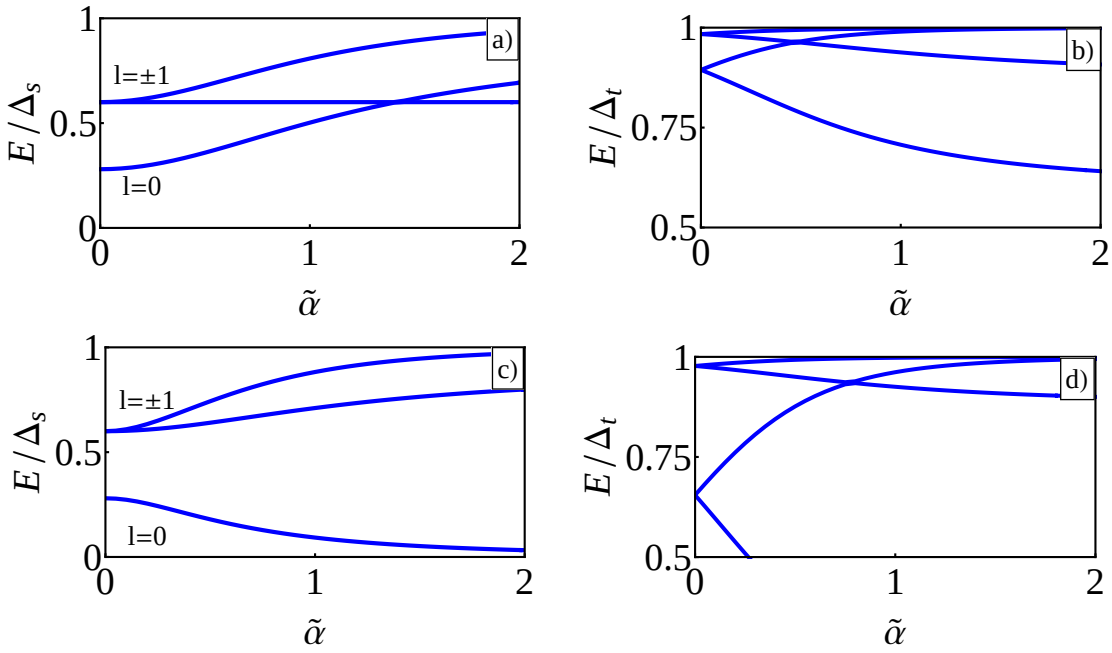

Figure 3.1: Dependence on SOC strength of the spectrum of YSR states induced by a purely magnetic impurity with $J_0 = 3/4$, $J_1 = 1/2$ in $s-$wave (a, c) and $p-$wave (b,d) superconductor for $S \parallel \hat{z}$ (a,b) and $S \parallel \hat{x}$ (c,d).

impurity potentials (J_l), and direction of $\mathbf{S}$ on the YSR spectrum.

We now study YSR states in a p-wave dominating regime. The energies of the YSR spectrum, in the presence of small SOC ($\tilde{\alpha} \ll 1$) for $\mathbf{S} \parallel \hat{z}$ are given by

$$\frac{|E_{1,2}|}{|\Delta_t|} = \frac{1 + J_0 J_1}{\sqrt{(1+J_0^2)(1+J_1^2)}} \pm |\tilde{\alpha}| \frac{(J_0 - J_1)^2}{(1+J_0^2)(1+J_1^2)} \tag{3.22}$$

$$\frac{|E_{3,4}|}{|\Delta_t|} = \frac{1}{\sqrt{1+J_1^2}} \pm |\tilde{\alpha}| \frac{J_1^2}{1+J_1^2}. \tag{3.23}$$

Fig. 3.1 show the evolution with $\tilde{\alpha}$ of the energies of the YSR states in a $p-$wave SC for $\mathbf{S} \parallel \hat{z}$ (b) and $\mathbf{S} \parallel \hat{x}$ (d). In the absence of SOC $\tilde{\alpha} = 0$, one can see that the YSR spectrum is isotropic in $s-$wave case due to the rotational spin symmetry. In $p-$wave case, this is not the case as follows from Fig. 3.1 b) and d). Since the p-wave pairing term mixes different angular momentum channels, l is not a good quantum number

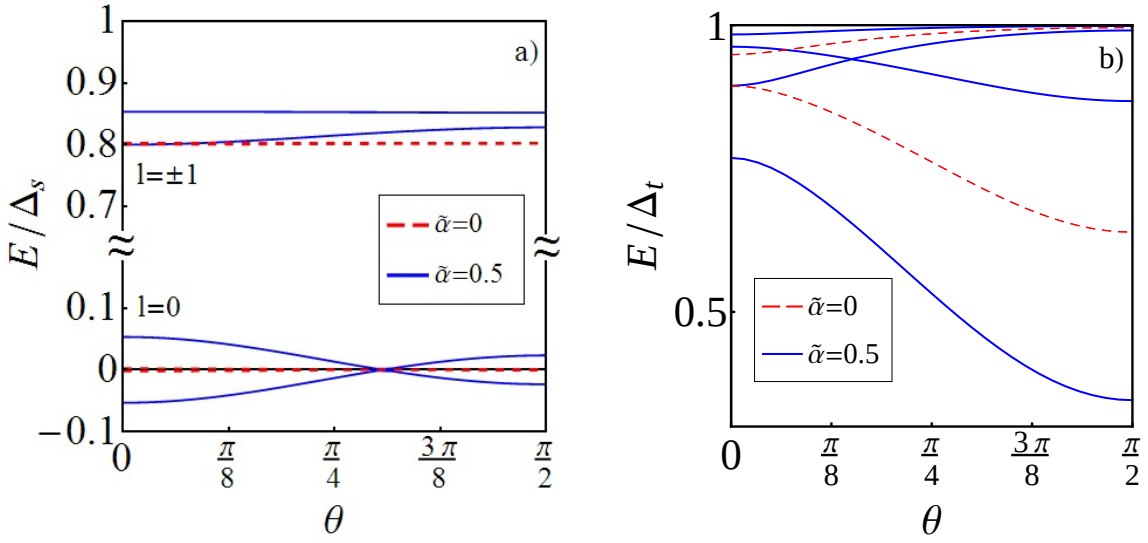

Figure 3.2: Bound state spectrum for magnetic impurity in a $s-$wave(a) and $p-$wave(b) SC as a function of the direction of magnetic moment at $J_0 = 1$, $J_{\pm 1} = 1/3$.

to label the states even in the absence of SOC. Furthermore, one can notice that the states are doubly degenerate at $\tilde{\alpha} = 0$ due to an additional symmetry present in the p-wave case. Indeed, the $p-$wave Green's function is invariant under the transformation $U = \tau_z \otimes \sigma_0 \otimes P$ with P being the momentum inversion operator $\mathbf{k} \to -\mathbf{k}$. Due to this symmetry YSR states appear in pairs in $p-$wave superconductor. In contrast, the $s-$wave Green's function does not have above symmetry and, as a result, there is only one bound state per angular momentum channel (i.e one state for $l = -1, 0, 1$ channels). It leads to the different parities of the number of YSR states in $s-$wave and $p-$wave regimes when the Rashba SOC is added to the Hamiltonian, see Figs. 3.1 and 3.2. This qualitative result allows one to identify the dominant superconducting pairing of a superconductor given that the resolution of the experimental probe is better than the splitting energy due to the Rashba SOC. We now discuss the dependence of the YSR spectrum on the orientation of magnetic impurity moment in $p-$wave superconductors. In contrast to $s-$wave superconductors, the YSR spectrum in $p-$wave case depends on θ even in the absence of SO coupling since $p-$wave pairing is characterized by the vector

$l_{\mathbf{p}}$, see Eq.(3.2). In the limit of zero SOC, one can find analytic solutions for the bound state spectrum.

$$\frac{|E_{1,2}|^2}{\Delta_t^2} = \frac{2 + 2J_0J_1\cos^2\theta + J_0^2(1+J_1^2)}{2(1+J_0^2)(1+J_1^2)} \pm \frac{J_0\sqrt{3J_1^2 - 2J_0J_1(1-J_1^2) + J_0^2(1+J_1^4) + J_1\cos 2\theta(J_1\cos 2\theta - 2J_0(1+J_0-J_1^2))}}{2(1+J_0^2)(1+J_1^2)} \tag{3.24}$$

Note that these bound states at $\alpha = 0$ are doubly degenerate. We can see that while the splitting is quadratic in $\tilde{\alpha}$ in $s-$wave dominating regimes, the splitting energy is linear in $\tilde{\alpha}$ in $p-$wave superconductor. The evolution of the YSR spectrum with θ is plotted in Fig. 3.2 (b). One can notice that the presence of the SOC enhances the dispersion of YSR states with θ.

3.2.3 Dimer of magnetic atoms

When we put two magnetic impurities close to each other, the YSR states in those atoms start to interact through the superconductor. This process which is responsible for the formation of YSR bands in chains of magnetic atoms, can also lead to dramatic changes in the spectrum of YSR states even for a dimer. [38, 79] Therefore, studying the spectrum of a dimer can be taken as a first step toward the understanding of the physics of chains.

In this section, we have studied the properties of a dimer formed by two magnetic impurities placed at a distance d from each other on the surface of the SC assuming $\Delta/\epsilon_F \ll 1$. Using the Eq. 3.11 we can calculate the bound state spectrum of a dimer, see Appendix A.2 for the details of calculation. We find that the wavefunction overlap between the YSR states induced by the two nearby atoms generates level splitting which strongly depends on the relative direction of the impurity spins, and that such splitting

depends on the strength of the SOC. This effect is due to the fact that the wavefunction overlap in spin sector is controlled by the relative direction of two magnetic moments and the amount of SOC. It is interesting to note that the presence of SOC, even when the SC is $s-$wave, has non-trivial effects on the spectrum even in the limit of single bound state per atom ($J_{\pm 1} = 0$). For this reason, to understand the effect of SOC on the YSR spectrum of a dimer we consider the case for $J_{\pm 1} = 0$. For the direction of the spin of the atoms, we fix one to be perpendicular to the plane, $\mathbf{S}_1 \parallel \hat{z}$ and control the direction of the other one, $\mathbf{S_2} = (\sin\theta, 0, \cos\theta)$. The dependence of the dimer YSR states spectrum on the relative angle θ is shown in Fig. 3.3 (a, b). For a $s-$wave superconductor without SOC, the two YSR states in dimer becomes degenerate at $\theta = \pi$ when the two states have opposite spin. The level splitting is at its maximum at $\theta = 0$ when those two YSR states wavefunction completely overlap in spin space. Once we add a SOC, the angle for the degeneracy shifts to some angle $\theta < \pi$ and the amount of this shift depends on the strength of the SOC. This effect can be understood from that the Rashba SOC can be gauged away by rotating the spinor around the $y-$axis depending on the position in $x-$direction. In other words, the electons' spins precess around the $y-$axis as they move along the $x-$axis in the presence of Rashba SOC. For a $p-$wave superconductor, there are total four states with two states per angular momentum channel per atom. In the absence of SOC, these four states becomes two doubly degenerate states at $\theta = \pi$. Once we turn on the SOC, these two crossing point shift into the opposite directions. These properties of the dimer spectrum can serve as useful tools in experiment. For a dimer of "soft" spins which one can tune the direction using applied local magnetic field or magnetized STM tip, the relation between YSR spectrum and relative angle can give information such as strength of the Rashba SOC and order parameter symmetry of the superconductor. Conversely, if the strength of the SOC is known, it allows the determination of the relative angle θ.

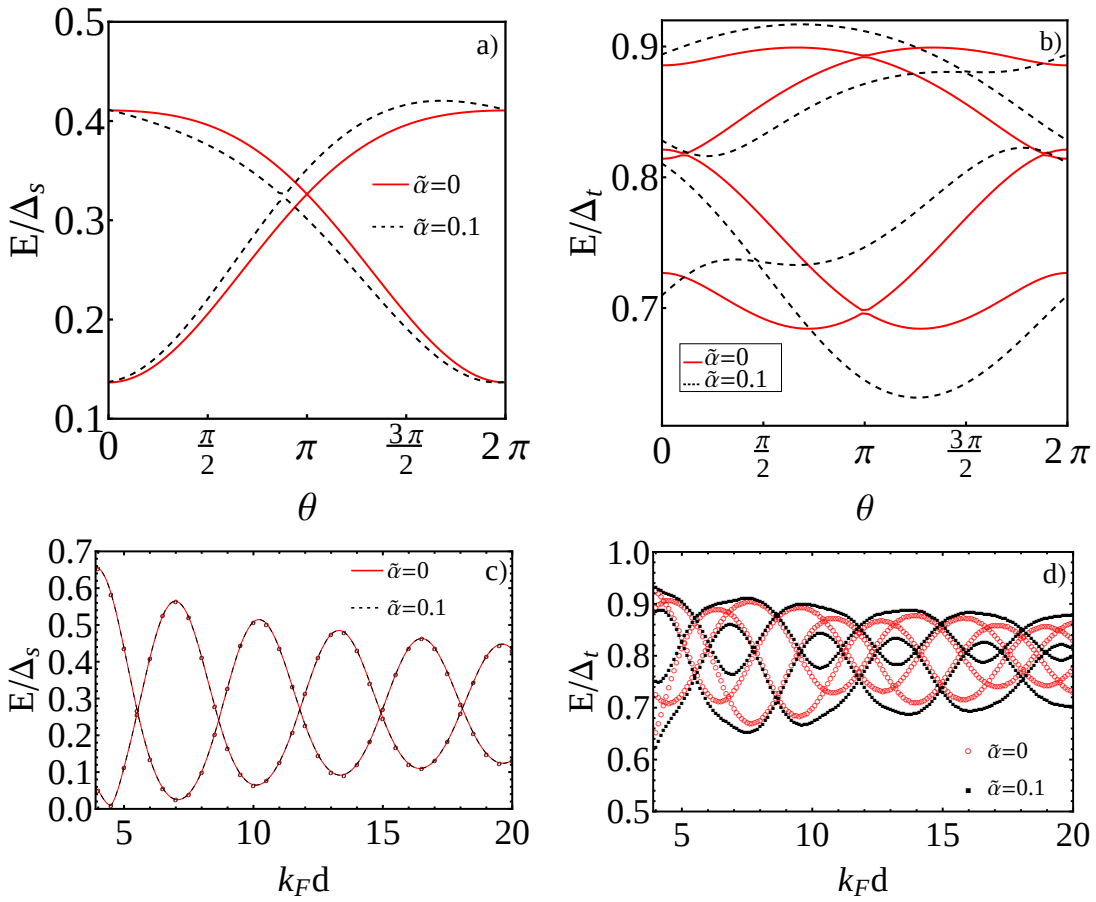

Figure 3.3: Bound state spectrum of a magnetic atom dimer along the $\hat{x}-$direction in a $s-$wave (a) and $p-$wave (b) SC. The direction of one spin is fixed along $\hat{z}$ while the other one pointing in $x-z$ plane with angle θ from $\hat{z}$. Here $J_0 = 3/4$, $k_F d = 6$ and $\epsilon_F = 1000\Delta_{s,t}$. (c) dependence of a dimer YSR spectrum on the distance d between the two impurities aligned along $\hat{z}$ for an $s-$wave SC; $\epsilon_F = 1000\Delta_s$, $J_0 = 3/4$. (d) Same as (c) but for a $p-$wave SC.

The properties of the system SC+dimer can be further identified by studying the dependence of the dimer YSR spectrum on the distance d between the two impurities. Figures 3.3 (c), (d) show the evolution of the energy levels of the YSR spectrum with d, for the case of an $s-$wave and $p-$wave SC respectively. As one can see, the level splitting has a oscillatory dependence in $k_F d$. Using the spectrum of several dimers with different inter atomic distance, one can extract the information on k_F and estimate the bandwidth of the chain with known lattice constant. It can also be used to engineer the chain with

optimum separation between the atoms, so the system can be in topological phase for given parameters. In the next section, we will extend our analysis to a chain of magnetic atoms where each atom supports multiple YSR states.

3.3 Multichannel extension of magnetic atom chain

In this section we consider a chain of magnetic atoms with ferromagnetic ordering and inter-atom distance a. The chain is placed on top of a two-dimensional $s-$wave superconductor with Rashba spin-orbit coupling, see Fig. 3.4 (a). From now on, we will take $\Delta = \Delta_s$, $\Delta_t = 0$ and represent the dimensionless SOC strength by α. We assume that each atom supports three YSR states correspond to $l = -1, 0, 1$, and the chain forms three YSR bands. We follow the formalism that we developed in the previous section.

To simplify the analysis and present the important findings clearly, we assume that the YSR states correspond to $l = 0$ and $|l| = 1$ are well separated. Then, we consider two different limits as shown in Fig. 3.4 (b) and (c). First case is when the single $l = 0$ band is close to the midgap energy $E = 0$ which we call "deep $s-$band" limit, see Fig. 3.4. This limit can be connected to the previous works on the single YSR band system in the limit J_1 goes to zero. We study the effect of adding SOC and $|l| = 1$ levels as a perturbation to the system. The second case is when $|l| = 1$ bands are closer to the midgap energy $E = 0$ than $l = 0$ band, see Fig. 3.4 (c). We call this case "deep $p-$band" limit. In this case, the physical properties of the whole system can be captured by two band effective Hamiltonian. The mixing between different angular momentum bands has various interesting effects on this Hamiltonian.

It is convenient to rewrite Eq. (3.11) in the following form:

$$\sum_j \mathbf{M}^{ij}(E)\overline{\Psi}_j = 0 \tag{3.25}$$

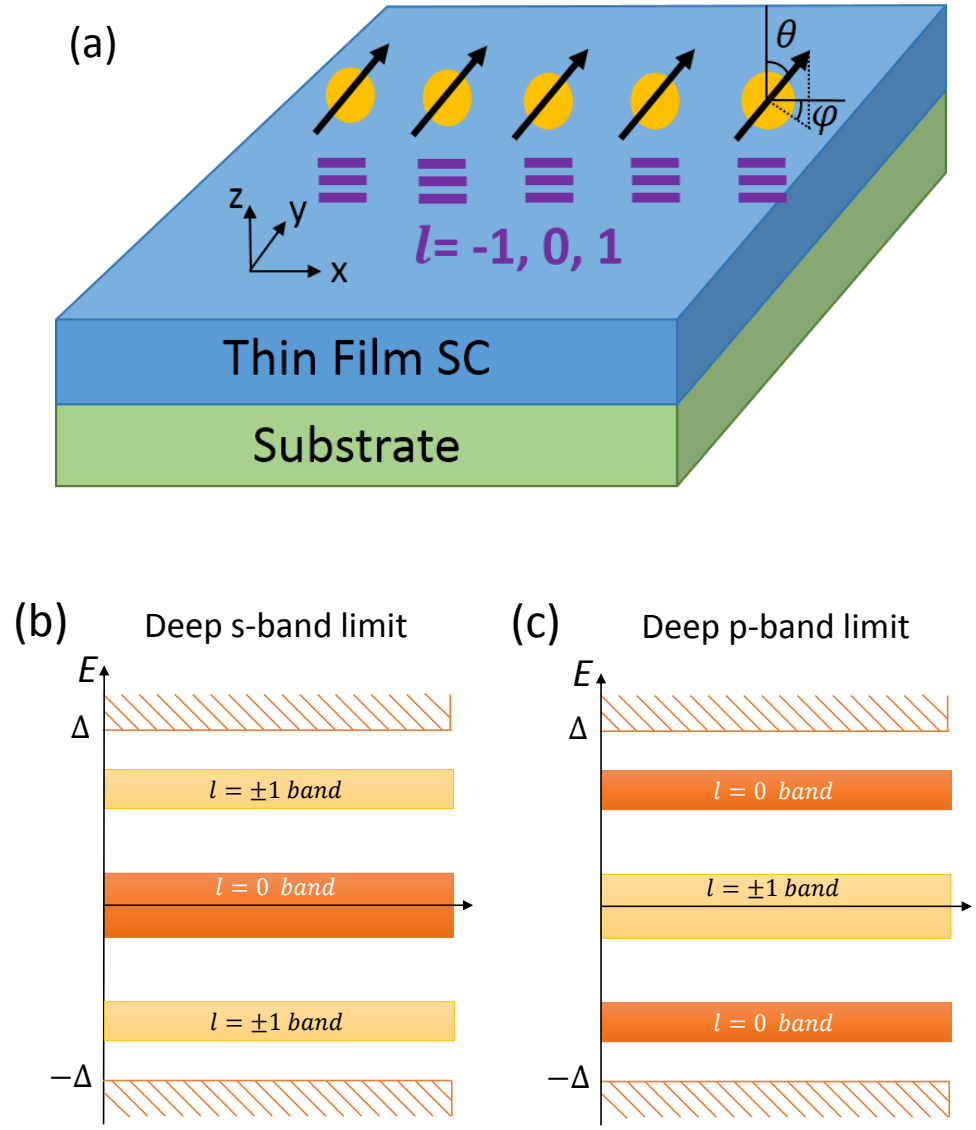

Figure 3.4: (a) Schematic diagram of a multichannel Yu-Shiba-Rusinov chain. (b, c) Schematic band structures for two different limits considered.

where $\overline{\Psi}_j = (\overline{\psi}_{i,-1}, \overline{\psi}_{i,0}, \overline{\psi}_{i,1})^T$ is a 12 dimensional spinor, and the matrix $\mathbf{M}^{ij}(E)$ is defined as $\mathbf{M}^{ij}_{l,l'} = \delta_{i,j}\delta_{l,l'} - \overline{G^{ij}_{l-l'}}(E)V^{l'}$. Here the local part of the matrix $\mathbf{M}^{ii}_{l,l'}$ determines the YSR spectrum of a single magnetic atom whereas the non-local part $\mathbf{M}^{ij}_{l,l'}$ describes the hybridization between YSR states induced by the magnetic atoms at i and j sites. For an equally spaced magnetic atom chain with distance a between the two nearest atoms, this hybridization leads to the formation of the YSR bands. In the limit of $k_F a \gg 1$, which we consider henceforth, the hopping energy scale is proportional to $1/\sqrt{k_F a}$ and, thus, the bandwidth W is small, i.e. $W \ll \Delta$. In this limit, the bands maintain the character of the single impurity YSR states and, thus, we refer to them as s or p-bands. Strictly speaking, SOC mixes different angular momentum states but, since we assume that $\alpha \ll 1$, this terminology is justified.

When s and p bands are well-separated by a gap that is much larger than the temperature, see Fig. 3.4(b) and (c), the problem can be considerably simplified by integrating out the higher-energy bands. In the following, we consider two limiting cases corresponding to the deep $s-$ and $p-$band limits and discuss the corresponding topological phase diagrams. We show that these two cases are qualitatively different since deep $p-$band limit consists of two bands originating from the $l = \pm 1$ YSR states.

3.3.1 Deep s-band limit

Effective Hamiltonian

We first consider the deep s-band limit such that the energy of the $l = 0$ state is close to $E = 0$, i.e., $J_0 \sim 1$ with the on-site energy $\epsilon_0 \approx \Delta(1 - J_0) + \mathcal{O}(\alpha^2) \to 0$. We assume $J_1 \ll J_0$ and limit of narrow bandwidth, so $l = 0$ band is well separated from the p bands. After integrating out the $l = \pm 1$ states, we obtain a tight-binding effective Hamiltonian for the single s-band with the virtual processes through $l = \pm 1$ channels

taken into account perturbatively. This can be done by rewriting $\overline{\psi}_{i,\pm 1}$ using Eq. (3.25)

$$\begin{aligned}\overline{\psi}_{i,-1} &= -(\mathbf{M}^{ii}_{-1,-1})^{-1}(\mathbf{M}^{ii}_{-1,0}\overline{\psi}_{i,0} + \sum_{j\neq i,l}\mathbf{M}^{ij}_{-1,l}\overline{\psi}_{j,l}),\\ \overline{\psi}_{i,1} &= -(\mathbf{M}^{ii}_{1,1})^{-1}(\mathbf{M}^{ii}_{1,0}\overline{\psi}_{i,0} + \sum_{j\neq i,l}\mathbf{M}^{ij}_{1,l}\overline{\psi}_{j,l}),\end{aligned} \tag{3.26}$$

and substituting above expressions into the equation for $l = 0$ component. Keeping terms up to the linear order in inter-site coupling, we obtain

$$\sum_j \mathbf{M}^{ij}_s(E)\overline{\psi}_{j,0} = 0, \tag{3.27}$$

where the exact expression for matrix $\mathbf{M}^{ij}_s(E)$ is given in the Appendix A.3. In order to find the effective Hamiltonian that describes the above equation, we expand the local on-site matrix to the linear order in E around $E = 0$, assuming that $\epsilon_0 \to 0$,

$$\mathbf{M}^{ii}_s(E) \approx \mathbf{M}^{ii(0)}_s - \mathbf{M}^{ii(1)}_s \cdot E, \tag{3.28}$$

and set $E = 0$ in the inter-site matrix:

$$\lim_{E\to 0}\mathbf{M}^{i\neq j}_s(E) \equiv \mathbf{M}^{i\neq j}_s(0). \tag{3.29}$$

In doing so we ignore terms $\mathcal{O}\left(1/k_F a\right) \ll 1$ and $\mathcal{O}\left(\frac{E}{\Delta\sqrt{k_F a}}\right)$. With these approximations, Eq.(3.27) can be written as

$$\sum_j H^{ij}_s\overline{\psi}_j = E\overline{\psi}_i, \tag{3.30}$$

where the local and non-local contributions are given by $H^{ii}_s = \left(\mathbf{M}^{ii(1)}_s\right)^{-1}\mathbf{M}^{ii(0)}_s$ and $H^{ij}_s = \left(\mathbf{M}^{ii(1)}_s\right)^{-1}\mathbf{M}^{i\neq j}_s(0)$, respectively. The tight-binding Hamiltonian $\mathcal{H}_s(i,j)$ is ob-

tained by projecting Eq. (3.30) onto the local YSR states: $\begin{pmatrix} \varphi_+, & \varphi_- \end{pmatrix}^T$ where $\varphi_\pm$ are the particle-hole pair of eigen-spinors of the single-impurity bound states with energy $\pm\epsilon_0$. The local basis can be found by solving the single-site equation $\mathbf{M}_s^{ii}(E)\varphi_\pm = 0$ as a special case of Eq. (3.27), where the bound state energies are determined from $\mathrm{Det}\left[\mathbf{M}_s^{ii}(E)\right] = 0$.

Here we consider three different cases by assuming that the all the atoms' moments are aligned ferromagnetically along a) $\hat{\mathbf{z}}$- (out-of-plane), b) $\hat{\mathbf{x}}$- (along the chain direction), and c) $\hat{\mathbf{y}}$- (in-plane but normal to the chain) axis, and present explicit expressions for the corresponding effective Hamiltonian. As we have seen in the previous section, due to the presence of SOC, the effective Hamiltonian is anisotropic which can be readily seen already at the single-impurity level. For the magnetic-atom with spin in $\hat{\mathbf{z}}-$axis, the eigen-spinors for $l = 0$ state read:

$$\varphi_+ \sim \begin{pmatrix} 1, & 0, & 1, & 0 \end{pmatrix}^T \text{ and } \varphi_- \sim \begin{pmatrix} 0, & 1, & 0, & -1 \end{pmatrix}^T. \tag{3.31}$$

When the spin is along $\hat{\mathbf{x}}$-axis, the eigen-spinors are given by

$$\varphi_+ \sim \begin{pmatrix} 1, & 1, & 1, & 1 \end{pmatrix}^T \text{ and } \varphi_- \sim \begin{pmatrix} -1, & 1, & 1, & -1 \end{pmatrix}^T. \tag{3.32}$$

Finally, for a spin along $\hat{\mathbf{y}}$-axis, the eigen-spinors are

$$\varphi_+ \sim \begin{pmatrix} 1, & i, & 1, & i \end{pmatrix}^T \text{ and } \varphi_- \sim \begin{pmatrix} i, & 1, & -i, & -1 \end{pmatrix}^T. \tag{3.33}$$

In the a) and b) cases, by transforming the effective tight-binding Hamiltonian $\mathcal{H}_s(i,j)$ to momentum space, we find that the corresponding Bogoliubov-de Gennes (BdG) Hamil-

tonian becomes

$$\frac{\mathcal{H}_s^{\hat{z}(\text{or }\hat{x})}(k)}{\Delta} = \begin{pmatrix} h_{z(x)}(k) & \tilde{\Delta}_{z(x)}(k) \\ \tilde{\Delta}^*_{z(x)}(k) & -h_{z(x)}(k) \end{pmatrix}. \tag{3.34}$$

To order α^2 and $\alpha/\sqrt{k_F a}$, the effective hopping energy is given by

$$h_z(k) = \epsilon_z + \frac{1}{2}\left[I_{0,+}(k) + I_{0,-}(k)\right], \tag{3.35}$$

$$h_x(k) = \epsilon_x + \frac{1}{2}\left[I_{0,+}(k) + I_{0,-}(k)\right]. \tag{3.36}$$

The functions $I_{n,\pm}(k) \equiv I_{n,\pm}(k, E=0)$ are defined in the Appendix A.1. The on-site energy is

$$\epsilon_z \simeq \frac{1-J_0}{J_0} + \frac{\alpha^2 J_1(2-J_0+J_1)}{J_0(1+J_1)^2}, \tag{3.37}$$

$$\epsilon_x \simeq \frac{1-J_0}{J_0} - \frac{\alpha^2 J_1^2\left[2(1-J_0)+(1-J_1^2)\right]}{J_0(1-J_1^2)^2}. \tag{3.38}$$

The effective p-wave pairing take the form

$$\tilde{\Delta}_z(k) = \tilde{\Delta}_x(k) = \frac{i}{2}\left[K_{1,+}(k) - K_{1,-}(k)\right] - \frac{i\alpha J_1}{1+J_1}\left[K_{1,+}(k) + K_{1,-}(k)\right]. \tag{3.39}$$

The functions $K_{n,\pm}(k) \equiv K_{n,\pm}(k, E=0)$ are defined in the Appendix A.1. To have a better understanding of the Hamiltonian structure in Eq. (3.34), it is instructive to perform a perturbative expansion of $h(k)$ and $\tilde{\Delta}(k)$, for example, around $k=0$,

$$h_z(k) \overset{k\to 0}{\approx} h_z^{(0)} + h_z^{(2)}k^2, \tag{3.40}$$

$$h_x(k) \overset{k\to 0}{\approx} h_x^{(0)} + h_x^{(2)}k^2, \tag{3.41}$$

$$\tilde{\Delta}_{z,x}(k) \overset{k\to 0}{\approx} \Delta^{(1)}k. \tag{3.42}$$

where the expressions for $h_{z,x}^{(0,2)}$ and $\Delta^{(1)}$ are given in the Appendix A.4. As we can check from the above expansion, the functions $h(k)$ and $\tilde{\Delta}(k)$ have the following properties $h(k) = h(-k)$ and $\tilde{\Delta}(-k) = -\tilde{\Delta}(k)$, and the gap is generically vanishing at $k = 0, \pi/a$. Moreover, the coefficient of the pairing term $\Delta^(1)$ is vanishing for $\alpha \to 0$. Therefore, the existence of SOC is crucial for ferromagnetic chain to support MZM as in the semiconductor nanowire proposal [54, 69].

In the limit $a/\xi_0 \to 0$, where $\xi_0 = v_F/\Delta$ is the superconducting coherence length, these functions have singular points for some values of $k_F a$ which is a consequence of the long-range nature of the hopping matrix element in the effective Hamiltonian. The presence of a finite coherence length ξ_0, however, regularizes the singularities. Nevertheless, such a strong dependence on $k_F a$ leads to significant variations of the effective mass and Fermi velocity. As in the case of YSR states for a single atom, the effective Hamiltonian is anisotropic due to the SOC (cf. Eq.(3.37)) which might be helpful to drive the topological transition by changing the direction of the magnetization of the impurities forming the chain. We note that this effect is absent for $J_1 = 0$, in which case we recover the results of Ref. [9]. Thus, the dependence of the effective chemical potential on the angle θ, which is the only tuning parameter in the Hamiltonian (3.34), is a feature of the multichannel magnetic impurity model.

Finally, in the case c) in which $\mathbf{S} \parallel \hat{\mathbf{y}}$, projection to the on-site spinor eigenstates leads to zero off-diagonal element in $\mathcal{H}^{\hat{y}}$, and the system is gapless.

Topological phase diagram

Having derived the effective Hamiltonian, we can now study the topological phase diagram. The Hamiltonian (3.34) for a generic direction of magnetization is in the symmetry class D [6, 84, 44], and, thus, is characterized by the $\mathbb{Z}_2$ topological invariant, the

so-called Majorana number $\mathcal{M}$ [45]:

$$\mathcal{M} = \text{sgn}\left[h(0)h(\pi/a)\right]. \tag{3.43}$$

The system is in the topological superconducting phase when $\mathcal{M} = -1$, whereas $\mathcal{M} = +1$ indicates a non-topological phase. We obtain the topological phase diagram by calculating $\mathcal{M}$.

(a) Topological phase diagram for the magnetization in $\hat{\mathbf{z}}$ direction, as a function of J_0 and $k_F a$ for $\alpha = 0.3$, $J_1 = 0.4$, and $\xi_0 = 2a$. (b) Topological phase diagram for the magnetization in $\hat{\mathbf{z}}$ direction as a function of α and $k_F a$ for $J_0 = 1.025$, $J_1 = 0.4$, and $\xi_0 = 2a$. (c) The phase boundary for the magnetization in $\hat{\mathbf{z}}$ direction (blue dashed line) and for the magnetization in $\hat{\mathbf{x}}$ direction (red solid line) indicates that by changing the magnetization one can drive the topological phase transition. (d) Calculated quasiparticle excitation gap for the parameter regime in the phase diagram (a) with the phase boundary indicated by white line.

Figure 3.5 (a) shows the topological phase diagram in the $(k_F a, J_0)$ plane for the deep s-band limit for the case in which the magnetic moments of the impurities forming the chain are aligned along the z direction and $\alpha = 0.3$. The dark and light colors represent topologically phase with MZM and trivial phases, respectively. The range of values of $k_F a$ has been chosen so that the inequality $1/\sqrt{k_F a} \ll 1$, on which expansion over $1/\sqrt{k_F a}$ is well satisfied. From Fig. 3.5 (a) we see that, for $\alpha = 0.3$ there is a large fraction of the $(k_F a, J_0)$ in which the chain is expected to be in a topological phase characterized by odd number of Majoranas at its ends. In Fig. 3.5 (b), the phase diagram as a function of the spin-orbit coupling strength α and $k_F a$ for for $J_0 = 1.025$, $J_1 = 0.4$, and $\xi_0 = 2a$. One can notice the oscillatory behavior of the phase boundary in terms of α and $k_F a$. The main reason for this is the fact that all the functions in the effective

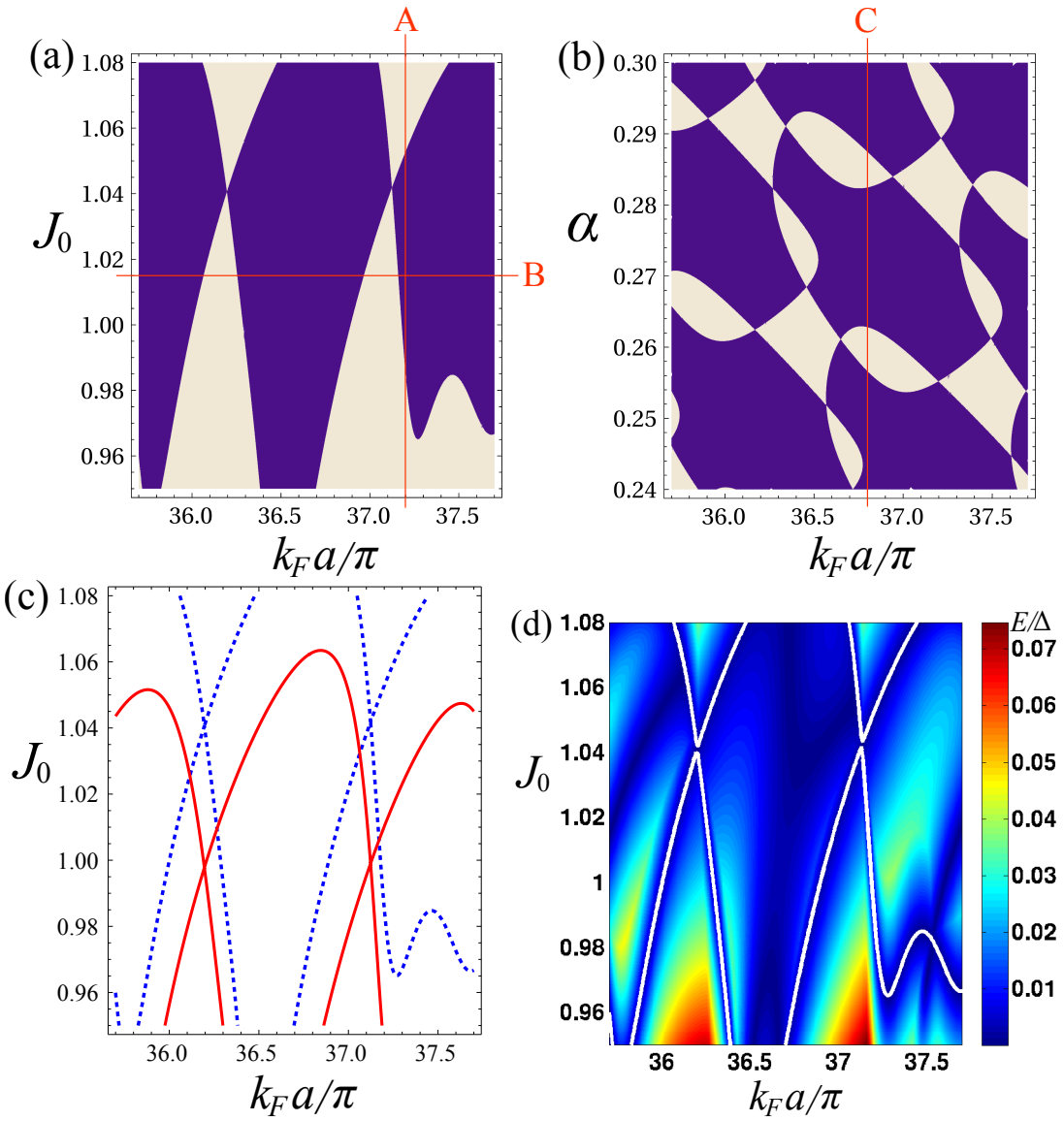

Figure 3.5: Topological phase diagram and phase boundary for the deep s band as a function of physical parameters.

Hamiltonian have oscillatory dependence on $k_{F,\lambda}a$ which again depends on both k_F and α.

Experimentally it can be challenging to vary in a controlled way parameters such as α, J_0, and k_Fa and therefore to verify the theoretical predictions shown in Fig. 3.5 (a), (b). However, our multichannel treatment, contrary to the single YSR band proposals [72, 9, 35], shows that the topological phase boundary of the system also depends on the direction of the magnetization of the chain. This is illustrated in Fig. 3.5 (c) in which we can observe that the boundaries of the topological phase in the (k_Fa, J_0) plane are different depending on the direction, z or x, of the magnetic moment of the impurities forming the chain. The phase boundary for chain with the magnetization in $\hat{\mathbf{z}}$ direction is described by blue dashed line, and the boundary for the magnetization in $\hat{\mathbf{x}}$ direction is described by red solid line. This result follows from the fact that the on-site energy, Eq.(3.37), depends on the direction of the impurity magnetization. Using this dependence of the topological index on the direction of the chain's magnetization, one may drive the topological phase transition in experiments by tuning the direction with applied magnetic field for magnetized STM tip for a chain in the dilute limit. Also, one can be able to observe the suppression of the induced gap when the magnetization direction continuously changes from $\hat{z}$ or $\hat{x}$ to $\hat{y}-$axis. Such changes in zero bias peak and localization length scale as a function of the direction of the magnetization would provide compelling evidence of the Majorana character of the observed zero energy states.

In addition to the topological index (Majorana number), we have also calculated quasiparticle excitation gap as a function of J_0, α, and k_Fa, see Fig. 3.5 (d) and Fig. 3.6 (a)-(c). One can notice that the closing of the gap is consistent with the phase boundaries between blue(topological) and white(trivial) colored region. Additionally, Fig. 3.6 (c) shows that there are gap closing points inside the topological phase which cannot be detected by just calculating the topological index. It turns out that these gapless points

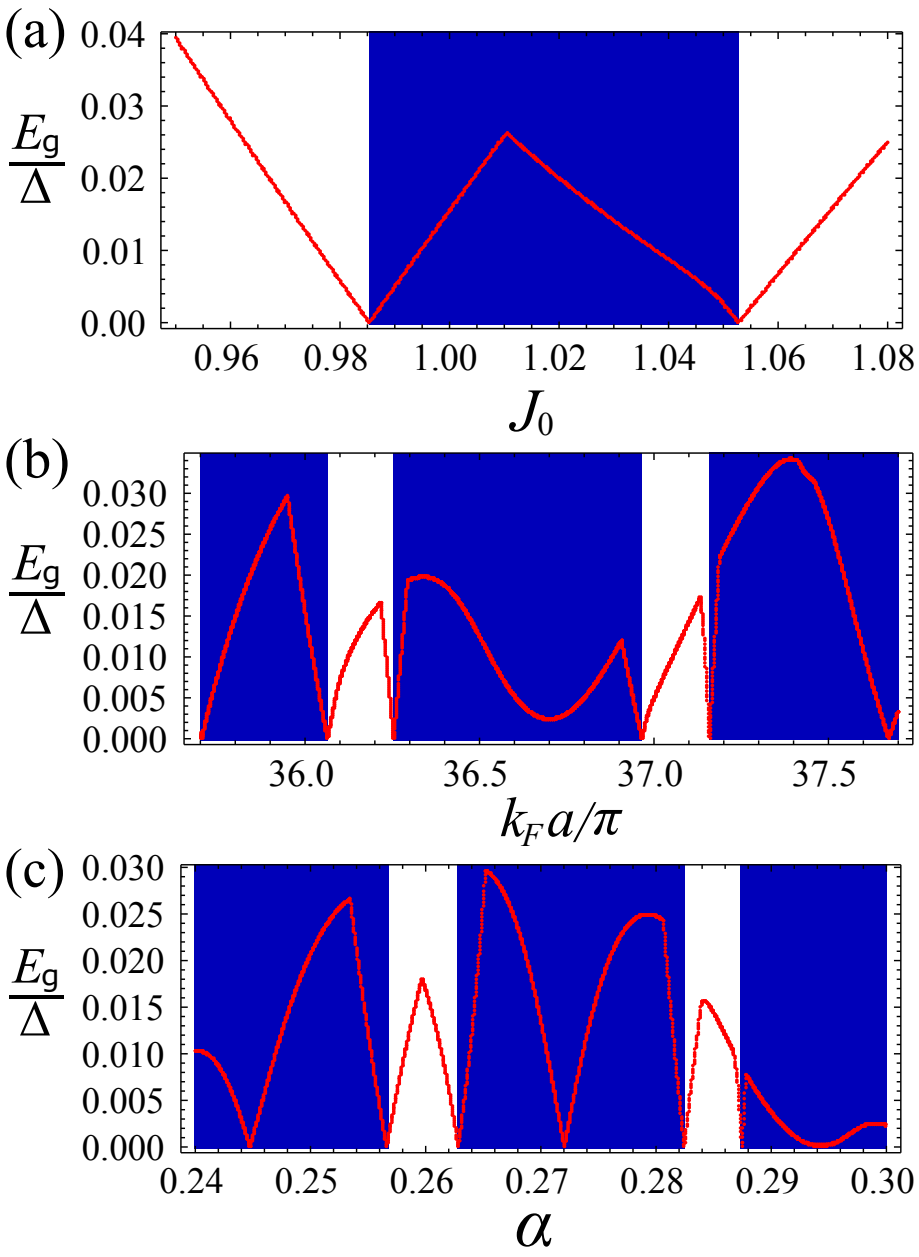

Figure 3.6: Quasiparticle excitation gap E_g along different line cuts on the phase diagrams. (a) Line-cut A in Fig. 3.5 (a). (b) Line-cut B in Fig. 3.5 (a). (c) Line-cut C in Fig. 3.5 (b)

.

inside the topological phase are related to the change of the winding number by two which leaves the $\mathbb{Z}_2$ invariant unchanged. We will discuss these gap closing points in more detail in the next section.

3.3.2 Deep p-band limit

Effective Hamiltonian

Now we study the deep p-band limit where the energy of the $l = \pm 1$ states is lower than that of $l = 0$, i.e., $J_0 \ll J_1 \sim 1$ and $\alpha^2 J_0 \ll 1$ such that the on-site energy $\epsilon \approx \Delta(1 - J_1) + \mathcal{O}(\alpha^2) \sim 0$. Once again, we assume that the $l = \pm 1$ states are well separated from the $l = 0$ state. After we integrate out $l = 0$ states, we obtain a tight-binding description for the p-bands with the s channel taken into account perturbatively by allowing for the transitions through intermediate virtual $l = 0$ states. The main difference with respect to the calculation in Sec. 3.3.1 is that there are now two particle-hole pairs of p-bands. Following the same procedure as in the previous section, we obtain the 8 dimensional matrix equation for the deep p-band limit:

$$\sum_j \mathbf{M}_p^{ij}(E)\overline{\Phi}_j = 0, \tag{3.44}$$

where $\overline{\Phi}_i = \left(\overline{\psi}_{i,-1}, \overline{\psi}_{i,1}\right)^T$ is the 8 dimensional spinor for the p-channel states. The derivation of the matrix $\mathbf{M}_p^{ij}(E)$ is presented in the Appendix A.3. Assuming that $k_F a \gg 1$ and $\epsilon \to 0$, the p-bands have narrow bandwidth with the center of the bands being close to $E = 0$. One can then linearize Eq.(3.44) with respect to E as we did in the previous section, and neglect the energy dependence of the inter-site matrix

$$\mathbf{M}_p^{i\neq j}(E) \sim \mathbf{M}_p^{i\neq j}(0) \tag{3.45}$$

by dropping the terms $\mathcal{O}\left(\frac{E}{\Delta\sqrt{k_F a}}\right)$ and $\mathcal{O}\left(\frac{\alpha^2}{\sqrt{k_F a}}\right)$ with $\alpha \ll 1$. We will keep henceforth the terms only up to $\mathcal{O}(\alpha^2)$ and $\mathcal{O}(\alpha/\sqrt{k_F a})$. After some algebra, Eq. (3.44) can be written as

$$\sum_j H_p^{ij}\overline{\Phi}_j = E\overline{\Phi}_i, . \tag{3.46}$$

Then, we project H_p^{ij} onto the local basis of YSR states: $\begin{pmatrix} \phi_{1,+}, & \phi_{2,+}, & \phi_{1,-}, & \phi_{2,-} \end{pmatrix}^T$ where $\phi_{1(2),\pm}$ are the eigenspinors of the single-impurity bound states with energy $\pm\epsilon_{1(2)}$ correspond to $l = \pm 1$. The local basis can be found by solving the single-site equation $\mathbf{M}_p^{ii}(E)\phi = 0$ as a special case of Eq. (3.44), where the bound state energies are determined from

$$\text{Det}\left[\mathbf{M}_p^{ii}(E)\right] = 0. \tag{3.47}$$

For example, when the spin of magnetic atom is along the $\hat{\mathbf{z}}-$axis, the local spinors are given by

$$\phi_{1,+} = \begin{pmatrix} 1, & 0, & 1, & 0, & 0, & 0, & 0, & 0 \end{pmatrix}^T, \tag{3.48}$$

$$\phi_{2,+} = \begin{pmatrix} 0, & 0, & 0, & 0, & 1, & 0, & 1, & 0 \end{pmatrix}^T, \tag{3.49}$$

$$\phi_{1,-} = \begin{pmatrix} 0, & 0, & 0, & 0, & 0, & 1, & 0, & -1 \end{pmatrix}^T, \tag{3.50}$$

$$\phi_{2,-} = \begin{pmatrix} 0, & 1, & 0, & -1, & 0, & 0, & 0, & 0 \end{pmatrix}^T. \tag{3.51}$$

After the projection onto the local basis and Fourier transformation we obtain the effective Hamiltonian $\mathcal{H}_p(k)$ describing the two coupled bands of the YSR chain in the deep-p band limit.

$$\frac{\mathcal{H}_p^{\hat{z}}(k)}{\Delta} = \begin{pmatrix} h_{11}(k) & h_{12}(k) & \tilde{\Delta}_{11}(k) & \tilde{\Delta}_{12}(k) \\ h_{21}(k) & h_{22}(k) & \tilde{\Delta}_{21}(k) & \tilde{\Delta}_{22}(k) \\ \tilde{\Delta}_{11}^*(k) & \tilde{\Delta}_{21}^*(k) & -h_{11}(k) & -h_{21}(k) \\ \tilde{\Delta}_{12}^*(k) & \tilde{\Delta}_{22}^*(k) & -h_{12}(k) & -h_{22}(k) \end{pmatrix}. \tag{3.52}$$

The coefficients here satisfy the following properties: $h_{ij}(k) = h_{ij}(-k)$, $\tilde{\Delta}_{ij}(-k) = -\tilde{\Delta}_{ij}(k)$ and, therefore, $\tilde{\Delta}_{ij}(k) = 0$ at $k = 0,\ \pi/a$. The effective dispersion energies and inter-band mixing, and their small k expansions can be written as

$$h_{11}(k) = \epsilon_1 + \frac{1}{2}\left[I_{0,+}(k) + I_{0,-}(k)\right] \overset{k\to 0}{\approx} h_{11}^{(0)} + h_{11}^{(2)}k^2, \tag{3.53}$$

$$h_{22}(k) = \epsilon_2 + \frac{1}{2}\left[I_{0,+}(k) + I_{0,-}(k)\right] \overset{k\to 0}{\approx} h_{22}^{(0)} + h_{22}^{(2)}k^2, \tag{3.54}$$

$$h_{12}(k) = h_{21}(k) = \frac{1}{2}\left[I_{2,+}(k) + I_{2,-}(k)\right] \overset{k\to 0}{\approx} h_{12}^{(0)} + h_{12}^{(2)}k^2 \tag{3.55}$$

with the on-site energies

$$\epsilon_1 = \frac{1 - J_1}{J_1} + \frac{\alpha^2 J_0(2 - J_1 + J_0)}{J_1(1 + J_0)^2}, \tag{3.56}$$

$$\epsilon_2 = \frac{1 - J_1}{J_1}. \tag{3.57}$$

The effective $p-$wave pairing contains both intra-band pairing

$$\tilde{\Delta}_{11}(k) = \frac{i}{2}\left[K_{1,+}(k) - K_{1,-}(k)\right] - \frac{i\alpha J_0}{1 + J_0}\left[K_{1,+}(k) + K_{1,-}(k)\right] \overset{k\to 0}{\approx} \Delta_{11}^{(1)}k, \tag{3.58}$$

$$\tilde{\Delta}_{22}(k) = \frac{i}{2}\left[K_{3,+}(k) - K_{3,-}(k)\right] \overset{k\to 0}{\approx} \Delta_{22}^{(1)}k, \tag{3.59}$$

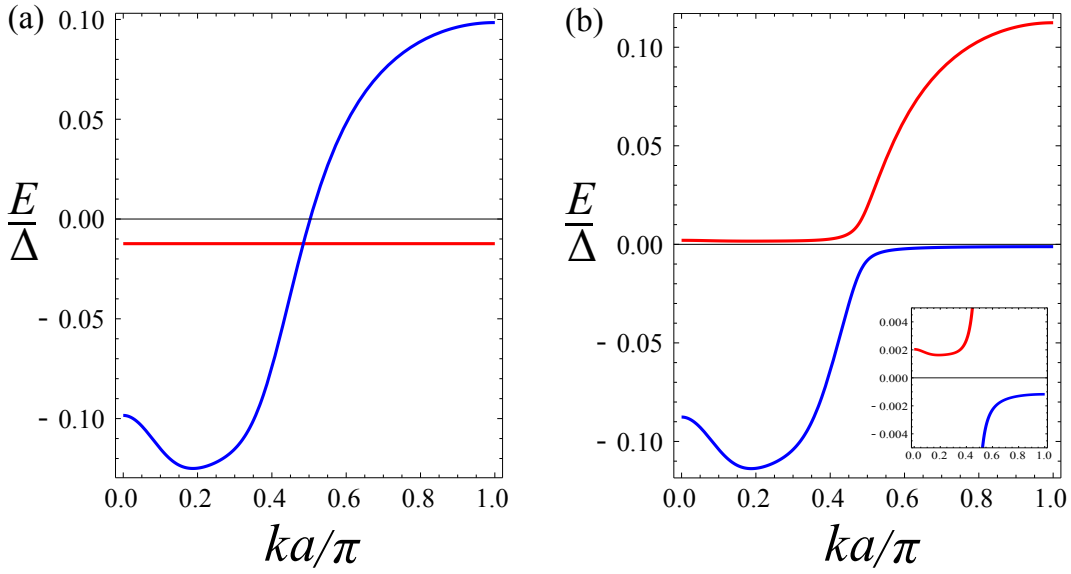

Figure 3.7: The normal-state ($\Delta_{ij} = 0$) band structure for $J_0 = 0.4$, $J_1 = 1.0125$, $k_F a = 37.5\pi$, $\xi_0 = 2a$, $\alpha = 0$(a) and $\alpha = 0.3$(b). The zoom-in figure of panel (b) near the Fermi level is shown in the inset.

and inter-band pairing

$$\begin{aligned}\tilde{\Delta}_{12}(k) &= \tilde{\Delta}_{21}(k) \\ &= \frac{i}{2}\left[K_{1,+}(k) - K_{1,-}(k)\right] - \frac{i\alpha J_0}{2\left(1+J_0\right)}\left[K_{1,+}(k) + K_{1,-}(k)\right] \overset{k\to 0}{\approx} \Delta_{12}^{(1)} k. \end{aligned} \tag{3.60}$$

The coefficients of the small k expansions are explained in the Appendix A.4. To understand the physics described by the above Hamiltonian, we first discuss the effect of SOC on the normal-state band structure (i.e. $\Delta_{ij} = 0$). The spectrum for the two bands reads

$$\frac{E_{\pm}^{N}(k)}{\Delta} = \frac{1}{2}\left[h_{11}(k) + h_{22}(k) \pm \sqrt{4h_{12}^2(k) + \left(\delta\epsilon_{12}\right)^2}\right] \tag{3.61}$$

where $\delta\epsilon_{12} = \epsilon_1 - \epsilon_2$. As shown in the Appendix A.1, to leading order in $1/\sqrt{k_F a}$, $I_{0,\lambda}(k) \approx I_{2,\lambda}(k)$. Hence h_{12} is approximately the same as h_{11} and h_{22}.

In the absence of Rashba spin-orbit coupling, $\delta\epsilon_{12}$ vanishes, and the band structure

is characterized by a flat(heavy) band $E_1^N = (1 - J_1)/J_1$ crossing with a dispersive(light) band $E_2^N = (1 - J_1)/J_1 + [I_{0,+}(k) + I_{0,-}(k)]$ with the bandwidth doubled compared to s-band, as shown in Fig. 3.7 (a). The on-site orbital structure of these two bands are symmetric(light) and anti-symmetric(heavy) combinations of $l = \pm 1$ states. The physical origin of these orbital structures reflects the degeneracy due to the isotropic magnetic potential and the asymptotically equal hopping amplitudes.

In the presence of SOC and a finite s-channel coupling (i.e. $J_0 \neq 0$ and $\alpha \neq 0$), $\delta\epsilon_{12}$ is non-zero, and a hybridization gap between the two bands develops which leads to an avoided level crossing, as shown in Fig. 3.7 (b). The induced hybridization gap gives rise to an interesting feature in the topological phase diagram that we will discuss below.

Topological Properties

The topological phase diagram for the $p-$band Hamiltonian (3.52) involves two bands which are hybridized by the SOC. Therefore, in order to compute the Z_2 topological invariant $\mathcal{M}$, we need to adopt the method developed for the multiband system [56]

$$\mathcal{M} = \mathrm{sgn}\left[\mathrm{Pf}B(0)\mathrm{Pf}B(\pi/a)\right] = \pm 1, \tag{3.62}$$

where the antisymmetric matrix, $B(p) = \mathcal{H}_p^{\hat{z}}(p)\tau_x$. For the two-band system, the corresponding expression for the Pfaffian is

$$\mathrm{Pf}B(p) = h_{12}(p)h_{21}(p) - h_{11}(p)h_{22}(p). \tag{3.63}$$

The topological phase diagram as a function of J_1 and $k_F a$ is shown in Fig. 3.8 (a). One can notice that the overall shape of the phase boundaries are similar to that of deep $s-$band limit except for the narrow trivial region in the middle which is enlarged

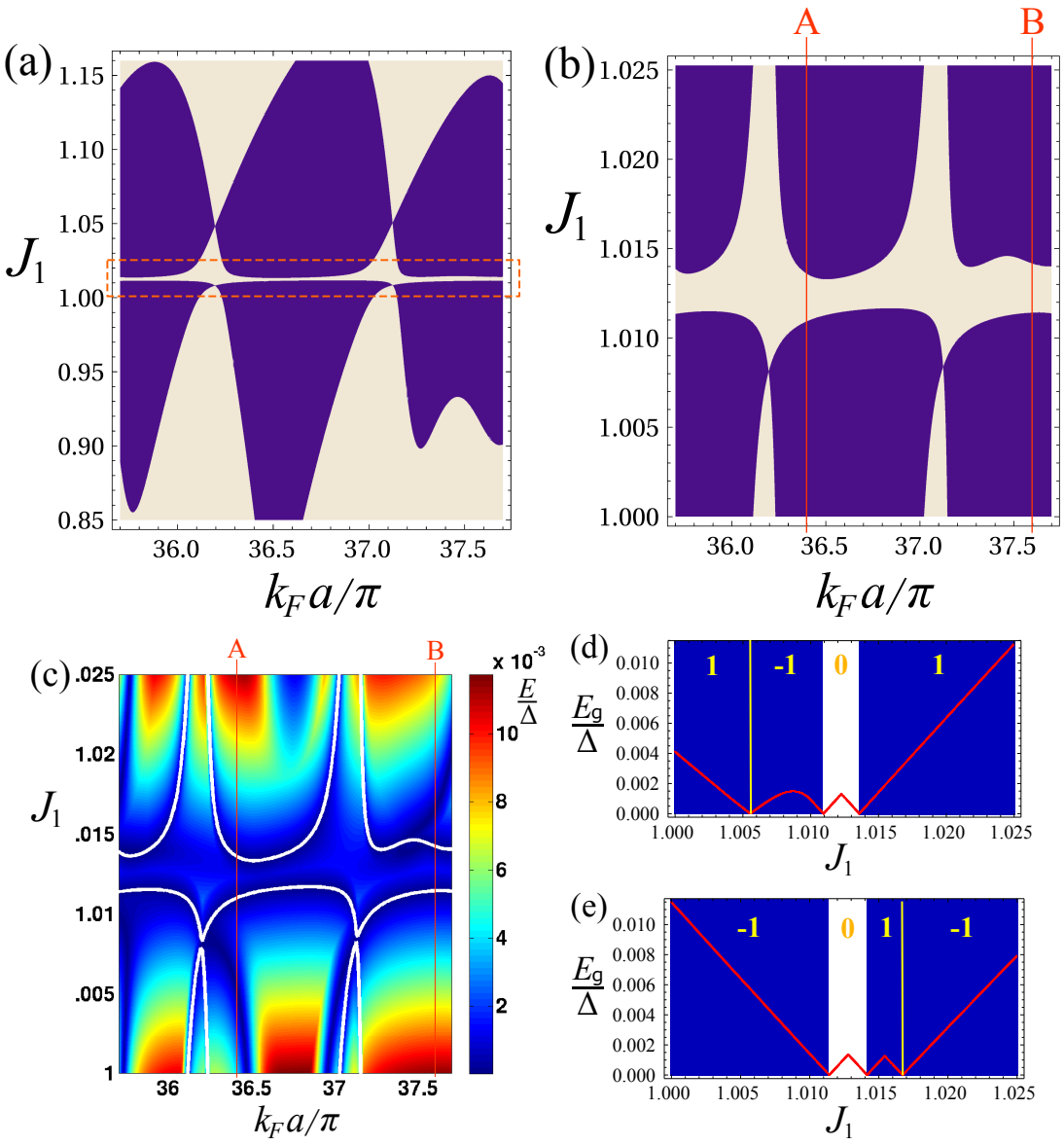

Figure 3.8: Topological phase diagram and quasiparticle gap for various parameters in the $p-$band limit. (a) Topological phase diagram in the $(k_F a, J_1)$ plane with $\mathbf{S} \parallel \hat{\mathbf{z}}$, $J_0 = 0.4$, $\alpha = 0.3$, and $\xi_0 = 2a$. (b) Enlargement of the topological phase diagram shown in (a) around the region surrounded by the dashed line rectangle. (c) Calculated quasiparticle excitation gap for the parameter regime in the phase diagram (b) with the phase boundary indicated by white line. (d) The quasiparticle excitation gap and the winding number on the line-cut A in panel (b) and (c) near the re-entrance region at $k_F a = 36.4\pi$. (e) The quasiparticle excitation gap and the winding number on the line-cut B in panel (b) and (c) near the re-entrance region at $k_F a = 37.6\pi$.

in Fig. 3.8 (b). The width of this region is controlled by the bandwidth of the heavy band which depends on the strength of SOC. Therefore, in the limit of small SOC we consider here, this trivial region is much smaller than the full area of the topological phase which is determined by $k_F a$. Indeed, the typical bandwidth of the light band is double the bandwidth of deep $s-$band limit for same $k_F a$ as we have seen above. As a result, the deep $p-$band limit support wide parameter space for realizing topological phase. This is surprising because a two-band system with similar bandwidth and energy tends to have zero $\mathbb{Z}_2$ index due to the even number of Fermi pockets. The origin of this interesting feature is due to the specific structure of inter-band mixing terms $h_{12}(k) \sim h_{11}(k) \sim h_{22}(k)$ of the YSR states.

In order to examine the stability of the topological phase, we compute the quasiparticle excitation gap E_g, see Fig. 3.8(c). Figure 3.8(d)-(e) plot the value of E_g along the two line-cuts on the phase diagram near the re-entrance region. One can see that the quasiparticle gap closing is consistent with the topological phase diagram in Fig. 3.8(b). The magnitude of the quasiparticle gap is also controlled by SOC since $\tilde{\Delta}_{ij} \sim \alpha$. Therefore, it is important to note that the SOC is a key ingredient for realizing topological superconducting phase with ferromagnetic atom chains.

In addition to the quasiparticle gap closing at the phase boundary, there are also points where the gap closes inside the topological phase, see Fig.3.8(d) at $J_1 \sim 1.005$ and Fig.3.8(e) at $J_1 \sim 1.017$. These gap closings are related to the additional symmetry of the effective Hamiltonian (3.52). In addition to the particle-hole symmetry $\mathcal{P} = \tau_x \mathcal{K}$ where $\mathcal{K}$ refers to complex conjugation, our effective spinless Hamiltonian also has a pseudo-time reversal symmetry $\mathcal{T} = \mathcal{K}$. Using these two symmetries, one can construct another symmetry - chiral symmetry $\mathcal{S} = \mathcal{T}\mathcal{P} = \tau_x$ which anticommutes with the Hamiltonian (3.52). Thus, the effective Hamiltonian belongs to the BDI symmetry class [6, 84, 44] which is characterized by the integer topological invariant, winding number $\mathcal{W}$ and supports mul-

tiple spatially-overlapping Majorana zero modes [11]. Our $\mathbb{Z}_2$ index, then, can be related to the parity of $\mathcal{W}$. In order to calculate the index $\mathcal{W}$, it is convenient to transform Eq. (3.52) into a chirality basis using a unitary transformation $\mathcal{U} = e^{-i\frac{\pi}{4}\tau_y}$ which converts the Hamiltonian to the off-diagonal form:

$$\mathcal{U}\mathcal{H}_p^{\hat{z}}(k)\mathcal{U}^\dagger = \begin{pmatrix} 0 & A(k) \\ A^\dagger(k) & 0 \end{pmatrix}. \tag{3.64}$$

Then, the winding number can be calculated by introducing a complex variable $z(k) = \det[A(k)]/|\det[A(k)]|$, and calculating the integral

$$\mathcal{W} = -\frac{i}{\pi}\int_{k=0}^{k=\pi} \frac{dz(k)}{z(k)}, \tag{3.65}$$

Using this analysis we find that, for example, the Hamiltonian at $J_1 = 1.001$ and $J_1 = 1.007$ in Fig. 3.7 (d) have different winding numbers $\mathcal{W}(J_1 = 1.001) = 1$ and $\mathcal{W}(J_1 = 1.007) = -1$ with same $\mathbb{Z}_2$ index. Thus, gap closing between these two regions corresponds to the transition between $\mathcal{W} = \pm 1$. The same argument holds for $J_1 = 1.015$. Thus, the gap closing points inside of the topological or non-topological phases are not accidental but represent the change of the winding number by an even integer.

The analysis above relies on the chiral symmetry. However, in realistic systems the chiral symmetry can be easily broken by allowing, for example, for a generic direction of magnetic moment of the chain with finite component along y-axis. The precise magnitude for the Majorana splitting energy, which is important for tunneling transport measurements, depends on the details of the chiral-symmetry-breaking perturbations.[67, 49, 23, 35, 37] As a consequence, the topological phases identified by the parity of the topological index are expected to be much more robust in realistic system.

3.4 Discussion

In Section 3.2, we have developed a formalism which allows us to understand YSR spectrum of a magnetic impurity atom with generic exchange coupling $J(|\mathbf{r}|)$ in two dimensional superconductors with $s-$wave and $p-$wave pairing symmetries and Rashba SOC. Using this formalism we have studied the effect of spin-orbit coupling on the multiple angular momentum channels of YSR states for a single magnetic atom and a dimer of two atoms.

We have shown that SOC mixes YSR states with different angular momentum and therefore strongly modifies their spectrum. In particular we have shown that, in the presence of SOC, the parity of the particle (or hole)-like YSR states is odd for $s-$wave superconductor and even for $p-$wave superconductor. We also have found that the YSR spectrum depends on the relative angle between the spin of the magnetic atom and the plane. For a chain, this property allows one to tune the chemical potential of the YSR band. In the case of a dimer, YSR spectrum oscillates as a function of the relative angle between the magnetic moments and the distance between the two atoms. These are predictions that can be tested experimentally using the scanning tunneling microscopy(STM) and have important implications for STM experiments trying to reveal the nature of the superconducting pairing in non-centrosymmetric superconductors. Since Pb has large SO coupling, our results shed some light on the measurements presented in Ref. [38, 79].

In Section 3.3, we have applied our multi-channel model to the ferromagnetic atom chain in the limit of weak SOC and well separated atoms $k_F a \gg 1$. The existence of multiple angular momentum scattering channels per each atoms and Rashba SOC leads to the multi-band theory with complicated structure for a chain of atoms. To simplify our analysis we assumed that single $s-$band mainly composed of $l = 0$ YSR states and double $p-$bands with $l = \pm 1$ YSR states are well separated and do not cross each other.

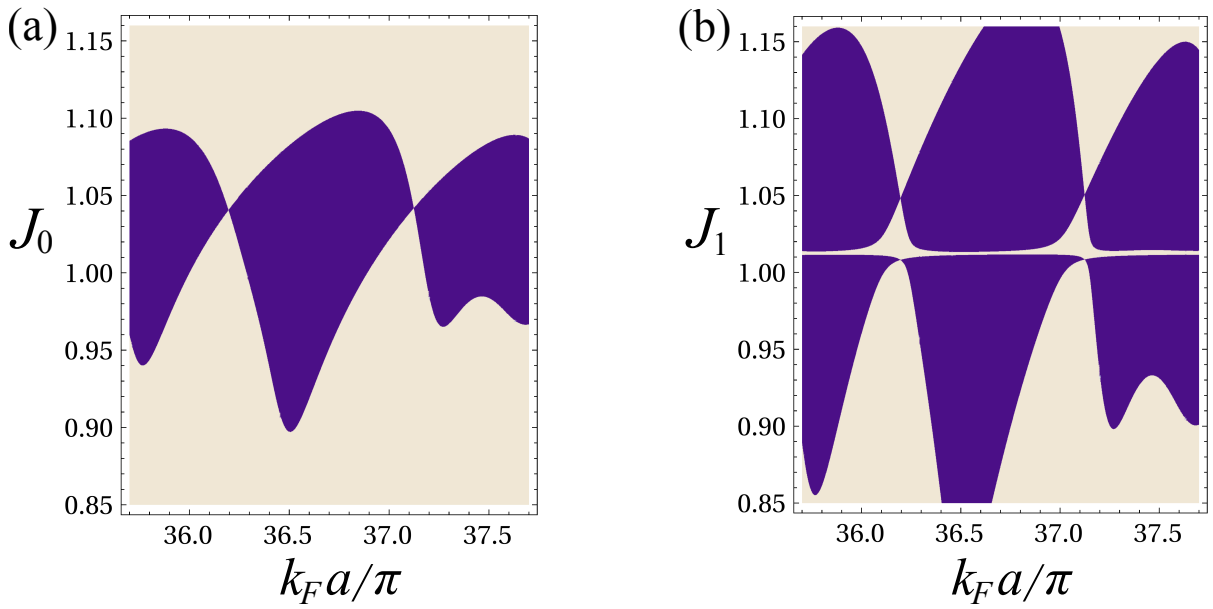

Figure 3.9: Comparison of the topological phase diagram in (a) the s band system for $\alpha = 0.3$, $J_1 = 0.4$, and $\xi_0 = 2a$; and in (b) the p band system for $\alpha = 0.3$, $J_0 = 0.4$, and $\xi_0 = 2a$.

Since the topological phase diagram are determined by partially filled band(s), we have considered two different scenarios where either $s-$band or $p-$bands are around $E = 0$. In deep $s-$band limit, the phase diagram qualitatively resembles the results from the previous single Shiba band proposals. In addition, we have found interesting features such as the dependence of phase boundaries on the direction of the magnetic moment, and these features originate from the presence of mixing to higher angular momentum channels. This feature can be used to control the magnetic atom chains in experiment to drive a topological phase transition.

We also have studied the deep $p-$band limit where two $l = \pm 1$ bands are partially filled. In contrast to the conventional wisdom, this two-band limit supports topological phase for wider region of parameter space than single band case, see Fig. 3.9. As one can notice from the figure, double bandwidth of the light $p-$band leads to larger parameter space for J_1 which means less fine tuning. This special property makes multiple YSR

bands system in two dimensional superconductor a good candidate for the observation of Majorana zero modes. We have also characterized the stability of the topological states by computing the quasiparticle excitation gap. We have found that there are gap closing points inside the topological/trivial phases and these gap closures are related to the additional symmetry in the effective Hamiltonian. The additional symmetry, however, can be easily broken by allowing the magnetic moment of the chain to have a finite component parallel to the plane but perpendicular to the chain.

For future studies, it will be interesting to study the multi-orbital Anderson model which can connect the half-metallic multiband wire limit to the multiple YSR-bands limit we have studied in this chapter. The spacing between nearby atoms in Ref. [62] is of the order of the Fermi wave length ($k_F a \sim 1$), in which case direct tunneling between iron atoms needs to be included, whereas our calculation assumes $k_F a \gg 1$. Therefore, it will be nice to understand how the band structure of dilute chain such as heavy and light bands in deep $p-$band limit transforms to multi-band half-metal as we increase the direct hopping between magnetic atoms. This can be useful to find the optimum interatomic spacing for more advanced experiments in the future.

Chapter 4

Signatures of time-reversal invariant topological superconductor

In this chapter, we study the ground state properties and transport signatures of one dimensional time-reversal invariant(TRI) topological superconductors where Majorana Kramers pair(MKP) at the ends are coupled to two different electronic systems with repulsive interactions. We first consider a case in which MKP is coupled to an interacting Luttingr liquid(LL). We analyze the ground state phase diagram as a function of interaction strength and other parameters using the renormalization group(RG) analysis, and show that Andreev reflection in spin-triplet channel is stable against weak repulsive interaction. We also study a MKP - quantum dot(QD) - normal lead(NL) junction using both RG analysis and slave-boson mean-field theory. We show that, for single QD occupancy limit, the ground state of the system can be described by strong correlation between MKP and a spin of QD.

The content in this chapter has been submitted to Physical Review B and is currently under review by APS. While the submitted manuscript was in preparation, we became aware of related independent work on this subject [74] which has some overlap with

Sec. 4.2.

4.1 Introduction

Topological superconductors show unique transport signatures due to the presence of Majorana zero modes (MZMs) at the boundaries. When a single MZM at the end of one-dimensional topological superconductor is coupled to a non-interacting lead, the quantized zero bias differential conductance of $2e^2/h$ appears due to the perfect Andreev reflection process. However, the signature of perfect Andreev reflection can be significantly modified in the presence of a strong repulsive interaction in the lead [32, 53, 26, 2]. In a MZM - QD - NL junction, the competition between Kondo correlation and coupling to the MZM leads to interesting physics such as a crossover between Kondo resonance and Majorana resonance appearing in the width of zero bias differential conductance peak [10]. Therefore, it is very important to understand the role of interactions in low dimensional systems involving MZMs.

Most previous works on the interplay between interactions and MZM has focused on the topological superconductors belonging to class D [6, 84, 44] with broken time-reversal (TR) symmetry and only one MZM at each end. However, a pair of MZMs can appear as a MKP in TRI topological superconductors belonging to class DIII [84, 44, 90]. Recently, several theoretical proposals were put forward to realize TRI topological superconductors [94, 21, 96, 64, 39, 31, 47, 85]. Transport signatures of MKPs and their detection schemes using a quantum point contact were also recently investigated in a quantum spin Hall system [50]. Most of the previous works on MKPs considered non-interacting models. For non-interacting systems, the presence of a MKP leads to a quantized conductance of $4e^2/h$ due to perfect Andreev reflection for two spin channels at the junction. The situation could be different, however, in the presence of interactions, and the fate of

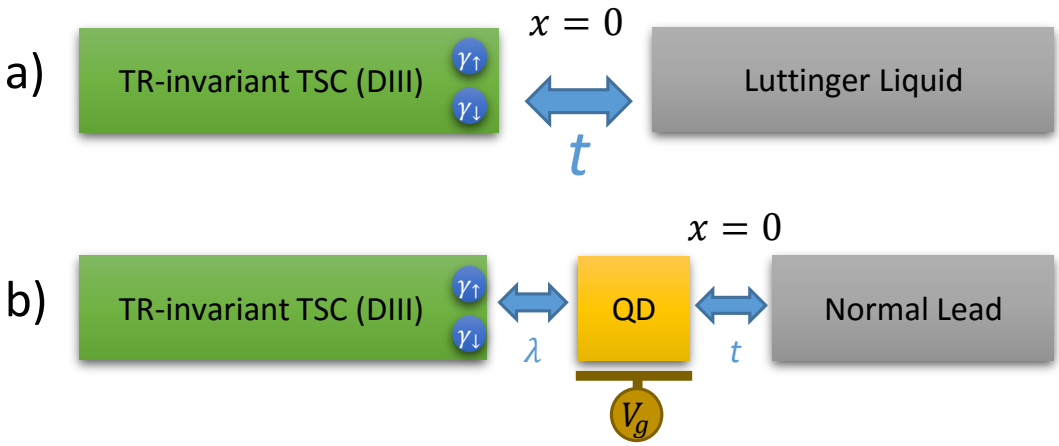

Figure 4.1: Schematic setup consisting of a) a junction between a LL and a TRI topological superconductor, and b) a QD coupled to a NL and a TRI topological superconductor. Here, $x = 0$ denotes the point in the lead which couples to the MKP or QD.

the perfect Andreev reflection is unclear. Interactions in a system containing MKP could also be very different from single MZM case since one can now introduce four fermion terms that consist of two Majoranas and two complex fermions. In this chapter, we study the signatures of MKPs in the presence of various kinds of interactions by considering two generic systems - a) MKP coupled to an interacting spinful LL (see Fig. 4.1 a)); b) MKP coupled to an interacting QD (see Fig. 4.1 b)).

In Sec. 4.2, we study a spinful LL with $\mathbb{SU}(2)$ spin symmetry coupled to a TRI topological superconductors with a single MKP per end. In the presence of an additional $\mathbb{U}(1)$ spin-rotation symmetry at the boundary, we find that for weak repulsive interactions, $1 > K_\rho \gtrsim 1/3$ with K_ρ being the Luttinger parameter, the Andreev reflection fixed point $(\mathbb{A} \times \mathbb{A})$ is stable and the normal reflection fixed point $(\mathbb{N} \times \mathbb{N})$ is unstable. For intermediate interaction strength $1/4 < K_\rho \lesssim 1/3$, the phase diagram depends on the strength of four-fermion interactions allowed by TR symmetry, which leads to a Berezinsky-Kosterlitz-Thouless (BKT) type transition between two phases characterized

by $\mathbb{A}\times\mathbb{A}$ and $\mathbb{N}\times\mathbb{N}$ fixed points. Finally, for sufficiently strong repulsive interactions $K_\rho < 1/4$, the two electron backscattering term becomes relevant, and drives the system to a stable normal reflection fixed point.

In the presence of spin-orbit coupling, the corresponding boundary theory may break $\mathbb{U}(1)$ spin-rotation symmetry. In this case, both spin-preserving Andreev reflection ($\mathbb{A}\times\mathbb{A}$) and spin-flip Andreev reflection ($\mathbb{SFA}$) are allowed, and they drive the system to different boundary conditions:

$$\mathbb{A}\times\mathbb{A}: \psi_\sigma(0) = -\psi^\dagger_\sigma(0), \tag{4.1}$$

$$\mathbb{SFA}: \psi_\sigma(0) = -i\psi^\dagger_{-\sigma}(0). \tag{4.2}$$

Therefore, the phase diagram depends on the relative strength of the corresponding Andreev scattering amplitudes. These boundary conditions, similar to those in a spin-triplet superconductor - LL junction, are stable with respect to weak repulsive interactions, and the physics is fundamentally different from an s-wave superconductor - LL junction where weak repulsive interactions destabilize Andreev reflection fixed point [26].

In Sec. 4.3, we study the effect of local interactions by considering a MKP coupled to a QD and an non-interacting NL. In the limit of large Coulomb repulsion U and single-electron occupation in the QD, the system shows competition between Kondo correlation and Majorana correlation. In the limit of strong Kondo correlation, the spin of the QD is screened by electrons in NL which leads to a boundary condition $\psi_{R\sigma}(0) = -\psi_{L\sigma}(0)$ where R/L denote right and left movers. As we increase the coupling between the QD and the MKP, the QD spin starts to form a correlation with MKP, and the system flows to a new fixed point where spin in the dot is coupled to the fermion parity of the MKP. This Majorana dominated fixed point is characterized by $\mathbb{A}\times\mathbb{A}$ boundary condition. We study the transport properties of this fixed point using a slave-boson mean-field theory [15, 7].

We show that the crossover between the Kondo dominated and Majorana dominated regimes can be understood in terms of the solutions of mean-field equations, and we analyze the stability of this mean-field solution with respect to Gaussian fluctuations [78, 16] finding that the mean field theory is stable, in the quasi-long range order sense, and can be used to calculate different observable quantities. We use this approach to calculate differential conductance at zero temperature as a function bias voltage.

4.2 Majorana Kramers pair coupled to Luttinger liquid

In this section we consider the junction shown in Fig. 4.1 a) consisting of a semi-infinite spinful LL coupled weakly to a TRI topological superconductor. We assume that the topological gap of the superconductor is much larger than the other relevant energy scales such that in the low-energy approximation, the TRI topological superconductor can be represented by only the MKPs localized at its ends. In this section, we will use $\psi_\sigma(0)$ to describe the operators at the boundary $x = 0$, and use $t(l_0)$ (similarly for $\tilde{t}$, Δ and $\tilde{\Delta}$) as the initial value in RG flow.

4.2.1 Majorana Kramers pair coupled to $\mathbb{SU}(2)$-invariant Luttinger liquid

Theoretical Model

We first consider an $\mathbb{SU}(2)$-invariant interacting spinful wire coupled to a MKP. The Hamiltonian for the wire can be written as the spinful LL model

$$H_{\text{lead}} = \sum_{j=\rho,\sigma} \frac{v_j}{2\pi} \int_0^\infty dx \left(K_j (\partial_x \theta_j)^2 + \frac{(\partial_x \phi_j)^2}{K_j} \right) \tag{4.3}$$

where $v_{\rho/\sigma}$ and $K_{\rho/\sigma}$ are velocity and Luttinger parameter for charge and spin modes, respectively. The bosonic fields satisfy the commutation relation

$$[\phi_\alpha(x), \theta_\beta(x')] = i\pi K_\alpha \delta_{\alpha\beta} \operatorname{sgn}(x - x'). \tag{4.4}$$

Here we follow the convention for the bosonization procedure [33]:

$$\psi_{R/L,s}(x) = \frac{\Gamma_{R/L,s}}{\sqrt{2\pi a}} e^{i\frac{1}{\sqrt{2}}\{\pm[\phi_\rho(x)+s\phi_\sigma(x)]+\theta_\rho(x)+s\theta_\sigma(x)\}} \tag{4.5}$$

where R/L represents right/left moving modes, a is an ultraviolet (UV) length scale, $s = \uparrow / \downarrow$ denotes fermion spin, and $\Gamma_{R/L,s}$ is the Klein factor.

The Hamiltonian for the whole system is given as

$$H = H_{\text{lead}} + H_B. \tag{4.6}$$

where H_B describes the coupling between the LL and the MKP. We neglect here the ground-state degeneracy splitting energy. The most general form of the boundary Hamiltonian with TR and $\mathbb{U}(1)$ spin-rotation symmetry including only two and four-fermion

operators can be written as

$$H_B = i\,t_\uparrow\gamma_\uparrow\left(\psi_\uparrow(0)+\psi_\uparrow^\dagger(0)\right) - i\,t_\downarrow\gamma_\downarrow\left(\psi_\downarrow(0)+\psi_\downarrow^\dagger(0)\right) \tag{4.7}$$
$$-\Delta i\gamma_\uparrow\gamma_\downarrow\left(-i\psi_\uparrow^\dagger(0)\psi_\downarrow(0)+i\psi_\downarrow^\dagger(0)\psi_\uparrow(0)\right) - \Delta_{\rm AN} i\gamma_\uparrow\gamma_\downarrow\left(-i\psi_\uparrow^\dagger(0)\psi_\downarrow^\dagger(0)+i\psi_\downarrow(0)\psi_\uparrow(0)\right).$$

The first two terms represent tunneling between the LL and the MKP with the amplitudes $t_{\uparrow/\downarrow}$. TR symmetry requires $t_\uparrow = t_\downarrow = t$. Assuming the spin-quantization axis is fixed in the whole system, the overall Hamiltonian H has $\mathbb{U}(1)$ spin rotation symmetry, leaving it invariant under the unitary transformation:

$$(\psi_\uparrow,\psi_\downarrow) \to R(\theta)(\psi_\uparrow,\psi_\downarrow) \tag{4.8}$$
$$(\gamma_\uparrow,\gamma_\downarrow) \to R(-\theta)(\gamma_\uparrow,\gamma_\downarrow). \tag{4.9}$$

Here $R(\theta)$ represents a $\mathbb{U}(1)$ rotation matrix by an angle θ. Thus, electron tunneling between LL and topological superconductor preserves the spin. The last two terms Δ and $\Delta_{\rm AN}$ represent normal, and anomalous backscattering terms, which, in fact, will also be generated by the tunneling terms in the RG flow in the presence of interactions in the LL.

Weak coupling RG analysis near normal reflection fixed point

We now study the stability of the normal reflection fixed point using weak coupling perturbative RG analysis. Around the normal reflection fixed point, the boundary conditions for lead electrons at $x = 0$ are given by $\psi_{R\sigma}(0) = \psi_{L\sigma}(0)$. In bosonization formalism, this boundary condition corresponds to $\Gamma_{L,s} = \Gamma_{R,s}$ and pinning $\phi_{\rho,\sigma}(0)$. Once we turn on the boundary couplings t, Δ and $\Delta_{\rm AN}$, boundary conditions for lead electrons may change depending on the strength of interaction in the lead. After integrating out the

fields away from $x = 0$, the corresponding imaginary-time partition function becomes

$$\mathcal{Z} = \int D[\theta_\rho] D[\theta_\sigma]\, e^{-(S_0+S_T)}, \tag{4.10}$$

with

$$S_0 = \sum_{j=\rho,\sigma} \frac{K_j}{2\pi} \int \frac{d\omega}{2\pi} |\omega| |\theta_j(\omega)|^2, \tag{4.11}$$

and the boundary coupling term reads

$$\begin{aligned} S_T = \int \frac{d\tau}{2\pi a} \Bigg[& t\big(i\gamma_\uparrow \Gamma_\uparrow \cos\frac{\theta_\rho + \theta_\sigma}{\sqrt{2}} - i\gamma_\downarrow \Gamma_\downarrow \cos\frac{\theta_\rho - \theta_\sigma}{\sqrt{2}}\big) \\ & - \Delta \gamma_\uparrow \gamma_\downarrow \Gamma_\uparrow \Gamma_\downarrow \cos\sqrt{2}\theta_\sigma - \Delta_{\mathrm{AN}} \gamma_\uparrow \gamma_\downarrow \Gamma_\uparrow \Gamma_\downarrow \cos\sqrt{2}\theta_\rho \Bigg]. \end{aligned} \tag{4.12}$$

Here we used short-hand notation $\theta_j(\tau)$ denoting the fields at $x = 0$.

We now derive the perturbative RG equations using the frequency shell integration by separating the bosonic fields θ_j into slow, and fast modes and integrating out the fast modes. After the procedure, the new effective action can be written as a cumulant expansion:

$$S_{\mathrm{eff}}[\theta_j^<] = S_0[\theta_j^<] + \langle S_T \rangle - \frac{1}{2}\left(\langle S_T^2 \rangle - \langle S_T \rangle^2 \right), \tag{4.13}$$

where the average $\langle \cdots \rangle$ describes an integration over the fast modes. For the details of this calculation, please refer to the Appendix B.1. Finally, we get the following RG equations:

$$\frac{dt}{dl} = \left(1 - \frac{1}{4K_\rho} - \frac{1}{4K_\sigma}\right) t - \frac{\Delta t}{4\pi v K_\sigma} - \frac{\Delta_{\mathrm{AN}} t}{4\pi v K_\rho}, \tag{4.14}$$

$$\frac{d\Delta}{dl} = \left(1 - \frac{1}{K_\sigma}\right) \Delta - \left(\frac{1}{K_\rho} - \frac{1}{K_\sigma}\right) \frac{t^2}{4\pi v}, \tag{4.15}$$

$$\frac{d\Delta_{\mathrm{AN}}}{dl} = \left(1 - \frac{1}{K_\rho}\right) \Delta_{\mathrm{AN}} + \left(\frac{1}{K_\rho} - \frac{1}{K_\sigma}\right) \frac{t^2}{4\pi v}. \tag{4.16}$$

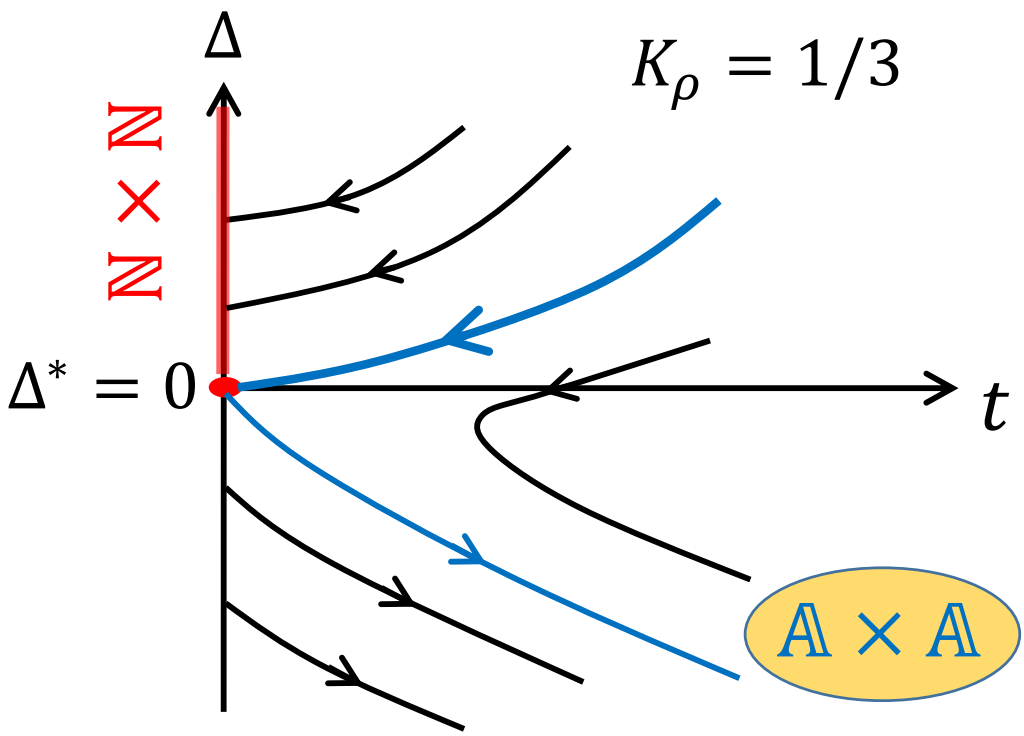

Figure 4.2: RG flow diagram near the normal reflection fixed point $\mathbb{N} \times \mathbb{N}$ for the MKP-LL junction with $U(1)$ spin-rotation symmetry and $K_\rho = 1/3$.

Here $dl = d \ln b$ where b is the ratio of the UV cutoff change from Λ to Λ/b with $\Lambda = v/a$. One can immediately see that t is a relevant perturbation in the non-interacting limit ($K_\rho = K_\sigma = 1$) and grows under RG. Therefore, in the non-interacting limit with $\Delta, \Delta_{\mathrm{AN}} \sim 0$, the system will flow to the perfect Andreev reflection fixed point ($\mathbb{A} \times \mathbb{A}$) corresponding to the boundary condition $\psi^\dagger_{L,s}(0) = -\psi_{R,s}(0)$ [26] and quantized differential conductance $G = \frac{4e^2}{h}$ at zero temperature.

Let us now try to understand the effects of interactions. For $\mathbb{SU}(2)$-invariant lead ($K_\sigma = 1$) and repulsive interactions in the nanowire $K_\rho < 1$, the coupling Δ_{AN} becomes

irrelevant and can be neglected. Then, the RG equations can be simplified to

$$\frac{dt}{dl} = \left(\frac{3}{4} - \frac{1}{4K_\rho}\right) t - \frac{\Delta t}{4\pi v}, \tag{4.17}$$

$$\frac{d\Delta}{dl} = -\left(\frac{1}{K_\rho} - 1\right) \frac{t^2}{4\pi v}. \tag{4.18}$$

The coupling t is relevant for not too strong repulsive interactions. It becomes marginal, however, if initial value of $\Delta(l_0)$ is equal to the special value $\Delta^* = \pi v(3 - \frac{1}{K_\rho})$. Indeed, then above RG equations (after a slight redefinition of variables) are identical to the anisotropic Kondo model [33], the solution of which is well-known. If the initial value of $\Delta(l_0)$ is zero, and $K_\rho \geq 1/3$, the system will flow to strong coupling $\mathbb{A} \times \mathbb{A}$ fixed point whereas for $K_\rho < 1/3$, the $\mathbb{N} \times \mathbb{N}$ fixed point is stable for small $t(l_0)$ and flow to strong coupling $\mathbb{A} \times \mathbb{A}$ for larger $t(l_0)$. The perturbative RG flow is summarized in Fig. 4.2.

Weak coupling RG analysis near perfect Andreev reflection fixed point

As we have seen in the previous section, the normal reflection fixed point is unstable for weak repulsive interactions and the system flows to the $\mathbb{A} \times \mathbb{A}$ Andreev reflection fixed point corresponding to the boundary conditions, $\psi^\dagger_{L,s}(0) = -\psi_{R,s}(0)$ which, in bosonic variables corresponds to pinning θ_ρ and θ_σ fields at $x = 0$. Thus, the fluctuating degrees of freedom are the fields ϕ_ρ and ϕ_σ and the corresponding boundary action reads

$$S_0 = \sum_{j=\rho,\sigma} \frac{1}{2\pi K_j} \int \frac{d\omega}{2\pi} |\omega| |\phi_j(\omega)|^2. \tag{4.19}$$

We now consider perturbations near the Andreev fixed point which are consistent with time-reversal and the spin-$\mathbb{SU}(2)$ symmetry of the LL lead. The only fermion bilinear

boundary perturbation preserving aforementioned symmetries is

$$\begin{aligned} H_{1B} &= \lambda_1(\psi^\dagger_{R\uparrow}(0)\psi_{L\uparrow}(0) + \psi^\dagger_{R\downarrow}(0)\psi_{L\downarrow}(0)) + h.c. \\ &= \frac{\lambda_1}{2\pi a}\cos\left(\sqrt{2}\phi_\rho\right)\cos\left(\sqrt{2}\phi_\sigma\right). \end{aligned} \tag{4.20}$$

In addition, one has to also consider the following four-fermion perturbation consistent with the above symmetries:

$$\begin{aligned} H_{2B} =& \lambda_2\psi^\dagger_{L\uparrow}(0)\psi_{R\uparrow}(0)\psi^\dagger_{L\downarrow}(0)\psi_{R\downarrow}(0) + h.c. \\ &= \frac{\lambda_2}{(2\pi a)^2}\sin(2\sqrt{2}\phi_\rho), \end{aligned} \tag{4.21}$$

which corresponds to two-electron backscattering. The perturbative RG equations for λ_1 and λ_2 are given by

$$\frac{d\lambda_1}{dl} = (1 - K_\rho - K_\sigma)\lambda_1 \tag{4.22}$$

$$\frac{d\lambda_2}{dl} = (1 - 4K_\rho)\lambda_2 \tag{4.23}$$

One can see that the first term λ_1 is irrelevant since $K_\sigma = 1$ whereas the second coupling becomes relevant for $K_\rho < 1/4$ indicating that $\mathbb{A} \times \mathbb{A}$ fixed point becomes unstable for strong repulsive interactions. Taking into account the perturbative RG analysis near both $\mathbb{N} \times \mathbb{N}$ and $\mathbb{A} \times \mathbb{A}$ fixed points, we conjecture the qualitative phase diagrams shown in Fig. 4.3. For the flow near $\mathbb{N} \times \mathbb{N}$ fixed point, the boundary perturbation Δ bends the transition line, i.e. the brown dashed line connecting $K_\rho = 1/3$ at $\mathbb{N} \times \mathbb{N}$ and $K_\rho = 1/4$ at $\mathbb{A} \times \mathbb{A}$. We also set the initial value $\Delta(l_0)$ to be zero.

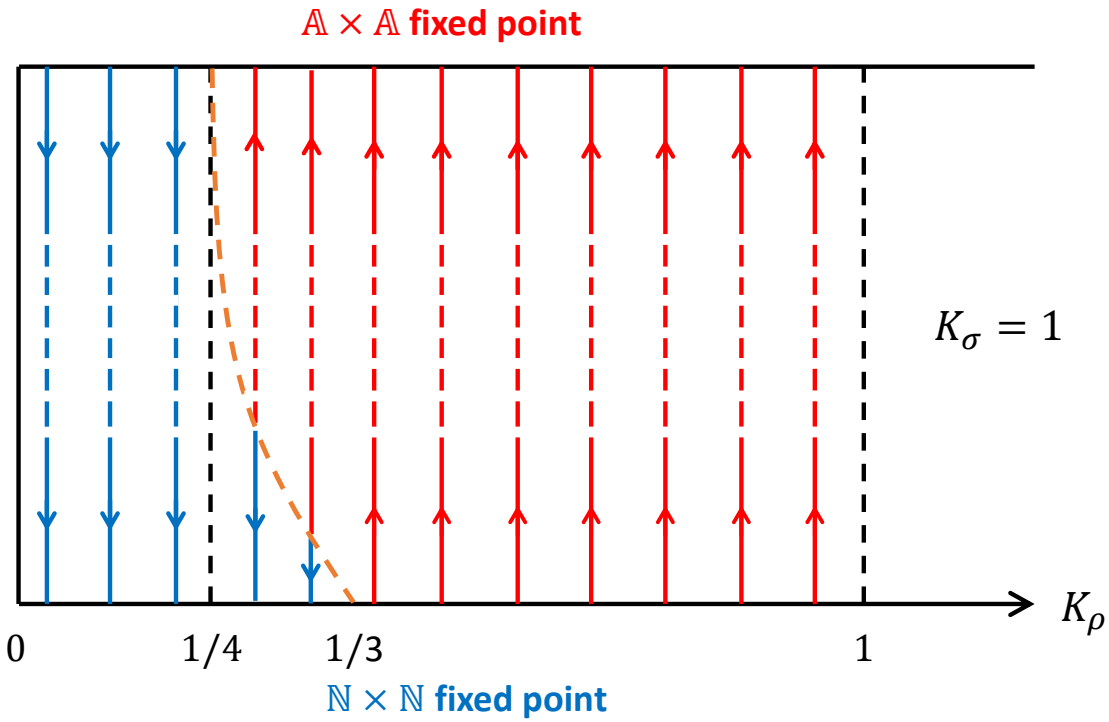

Figure 4.3: Illustration of the flow between the normal reflection fixed point $\mathbb{N} \times \mathbb{N}$ and the Andreev reflection fixed point $\mathbb{A} \times \mathbb{A}$ for the junction with $\mathbb{U}(1)$ spin-rotation symmetry.

Differential tunneling conductance

In this subsection, we discuss the qualitative behavior of the finite temperature correction on the differential conductance by calculating $G = dI/dV$ at zero voltage bias as a function of temperature. A similar analysis can be done for the linear conductance G at $V = 0$ as a function of temperature T. The RG flow between the normal $\mathbb{N} \times \mathbb{N}$ and Andreev reflection $\mathbb{A} \times \mathbb{A}$ defines a crossover temperature T^*, which roughly corresponds to the width of the zero bias peak. Although the conductance for the whole crossover regime requires involved calculations, the conductance around $\mathbb{N} \times \mathbb{N}$ and $\mathbb{A} \times \mathbb{A}$ fixed points can be obtained using a perturbative approach [55]. First of all, we consider the case $\Delta(l_0) = 0$ and $1/3 < K_\rho < 1$, where $\mathbb{A} \times \mathbb{A}$ fixed point is stable. In the UV limit near the normal reflection fixed point, the leading relevant perturbation is the coupling to the MKP, t, which has scaling dimension $\frac{3}{4} - \frac{1}{4K_\rho}$. Near the infrared (IR) limit near the Andreev reflection fixed point, the deviation from the quantized value comes from the leading irrelevant operators which is the normal backscatterings in Eq. (4.20) with scaling dimension $-K_\rho$.

We can now obtain scaling of the conductance with temperature at zero bias:

$$\left.\frac{G}{4e^2/h}\right|_{K_\rho > \frac{1}{3}} = \begin{cases} c_1(K_\rho)\left(\frac{T}{T^*}\right)^{2(\frac{1}{4K_\rho}-\frac{3}{4})}, & T \gg T^* \\ 1 - c_2(K_\rho)\left(\frac{T}{T^*}\right)^{2K_\rho}, & T \ll T^* \end{cases}, \tag{4.24}$$

where $c_{1,2}(K_\rho)$ are numerical coefficients of the order one. Similarly, one can obtain voltage corrections to the conductance at zero temperature [55].

Next, we consider the case for $K_\rho < 1/4$, where $\mathbb{N} \times \mathbb{N}$ is the stable IR fixed point. In this case, we start near the UV fixed point, $\mathbb{A} \times \mathbb{A}$, and calculate the conductance by perturbing with the two-electron backscattering operator which is the leading relevant

operator in this regime. Thus, we obtain

$$\left.\frac{G}{4e^2/h}\right|_{K_\rho \lesssim \frac{1}{3}} \sim \begin{cases} 1 - c_3(K_\rho)\left(\frac{T}{T^*}\right)^{2(4K_\rho - 1)}, & T \gg T^* \\ c_4(K_\rho)\left(\frac{T}{T^*}\right)^{2(\frac{1}{4K_\rho} - \frac{3}{4})}, & T \ll T^* \end{cases}, \tag{4.25}$$

where $c_{3/4}(K_\rho)$ are $\mathcal{O}(1)$ numerical coefficients. The calculation of the conductance in the regime $1/4 < K_\rho \lesssim 1/3$ will depend on microscopic details.

4.2.2 The effect of breaking the $\mathbb{U}(1)$ symmetry at the boundary

Theoretical Model

In this section, we study the effect of breaking the $\mathbb{U}(1)$ spin-rotation symmetry at the boundary. When we couple LL to MKP, the spin eigenstates of the MKP do not have to be the same as the spin eigenstates of the LL. Therefore, the tunneling between the LL and the TRI topological superconductor can have both spin-preserving and spin-flip components. For example, if we add Rashba spin-orbit coupling (SOC) which has an angle θ rotation compared to that of the MKP. The corresponding tight binding model can be written as

$$\begin{aligned} H =& H_{\text{lead}} + H_{\text{T}} \qquad (4.26) \\ H_{\text{lead}} =& -t\sum_j \sum_s \left(c^\dagger_{j+1,s} c_{j,s} + h.c.\right) + \mu \sum_{js} c^\dagger_{j,s} c_{j,s} \\ &+ \sum_{jss'} (-i)\alpha_R c^\dagger_{j+1,s} \left(\cos\theta\sigma_z + \sin\theta\sigma_y\right)_{ss'} c_{j,s'} + h.c., \\ H_{\text{T}} =& it_0 \left[\gamma_\uparrow (c_{0\uparrow} + c^\dagger_{0\uparrow}) - \gamma_\downarrow (c_{0\downarrow} + c^\dagger_{0\downarrow})\right]. \qquad (4.27) \end{aligned}$$

One can see that the above Hamiltonian respects TR symmetry. We apply the following unitary transformation

$$\begin{pmatrix} \psi_{i\uparrow} \\ \psi_{i\downarrow} \end{pmatrix} = e^{-i\frac{\theta}{2}\sigma_x} \begin{pmatrix} c_{i\uparrow} \\ c_{i\downarrow} \end{pmatrix}, \tag{4.28}$$

and then the bulk and boundary Hamiltonian become

$$H_{\text{lead}} = \mu \sum_{js} \psi^\dagger_{j,s}\psi_{j,s} + \sum_j \Big[(-t - i\alpha_R)\psi^\dagger_{j+1,\uparrow}\psi_{j,\uparrow} + (-t + i\alpha_R)\psi^\dagger_{j+1,\downarrow}\psi_{j,\downarrow} + h.c.\Big], \tag{4.29}$$

$$H_{\text{T}} = it \sum_{s=\uparrow,\downarrow} s\gamma_s(\psi_{0,s} + \psi^\dagger_{0,s}) + \tilde{t}\sum_s s\gamma_s(\psi^\dagger_{0,-s} - \psi_{0,-s}), \tag{4.30}$$

where $t = t_0\cos\theta$ and $\tilde{t} = t_0\sin\theta$, and $s = 1(-1)$ for spin-$\uparrow$ ($\downarrow$). Therefore, the spin-flip tunneling naturally arises in the presence of SOC. In addition, one can also have different types of interactions such that the new boundary Hamiltonian in continuum limit has more general form:

$$\begin{aligned} H_{\text{B}} =& it \sum_{s=\uparrow,\downarrow} s\gamma_s \left(\psi_s(0) + \psi^\dagger_s(0)\right) + \tilde{t}\sum_s s\gamma_s \left(\psi^\dagger_{-s}(0) - \psi_{-s}(0)\right) \\ &- \Delta i\gamma_\uparrow\gamma_\downarrow \left(-i\psi^\dagger_\uparrow(0)\psi_\downarrow(0) + i\psi^\dagger_\downarrow(0)\psi_\uparrow(0)\right) + \tilde{\Delta} i\gamma_\uparrow\gamma_\downarrow \left(\psi^\dagger_\uparrow(0)\psi_\uparrow(0) - \psi^\dagger_\downarrow(0)\psi_\downarrow(0)\right). \end{aligned} \tag{4.31}$$

Note that we did not include the irrelevant terms such as Δ_{AN}. One can simply check that, for generic values of t, $\tilde{t}$, Δ and $\tilde{\Delta}$ the $U(1)$ symmetry shown in Eq. (4.9) is broken. In this case, the boundary condition at the Andreev reflection fixed point is determined by the relative magnitude of t and $\tilde{t}$ as we discuss in the next subsection.

Scattering matrix analysis for the non-interacting lead

First, we analyze the boundary conditions in the non-interacting case with $\Delta = \tilde{\Delta} = 0$ using the scattering matrix approach. The unitary scattering matrix is defined as [66]

$$S(\omega) = \hat{I} + 2\pi i \hat{W}^\dagger \left(H_{MK} - \omega - i\pi \hat{W}\hat{W}^\dagger \right)^{-1} \hat{W}, \tag{4.32}$$

where H_{MK} is the Hamiltonian for the MKP (2 by 2 matrix) which vanishes in the limit of zero splitting energy for MKP. Note that the local term $i\delta_0 \gamma_\uparrow \gamma_\downarrow$ is not allowed by TR symmetry. The matrix $\hat{W}$ describes the coupling between the MKP $\gamma_\uparrow, \gamma_\downarrow$ and the lead degrees of freedom in the basis $(\psi_\uparrow, \psi_\downarrow, \psi_\uparrow^\dagger, \psi_\downarrow^\dagger)$:

$$\hat{W} = \begin{pmatrix} it & \tilde{t} & it & -\tilde{t} \\ -\tilde{t} & -it & \tilde{t} & -it \end{pmatrix}. \tag{4.33}$$

Note that we assume the lead Hamiltonian is diagonal in this basis. Using Eq. (4.32), we can represent the scattering matrix at $\omega = 0$ as

$$S(0) = \begin{pmatrix} S^{ee}(0) & S^{eh}(0) \\ S^{he}(0) & S^{hh}(0) \end{pmatrix}. \tag{4.34}$$

The components $S^{ee}(0)$ and $S^{eh}(0)$ describe normal and Andreev reflection, respectively. As pointed out in Ref. [50], the normal part $S^{ee}(0)$ is zero so we focus on the non-diagonal components:

$$\begin{aligned} S^{eh}(0) &= \begin{pmatrix} \frac{\tilde{t}^2 - t^2}{t^2 + \tilde{t}^2} & -\frac{2i\tilde{t}t}{t^2 + \tilde{t}^2} \\ -\frac{2i\tilde{t}t}{t^2 + \tilde{t}^2} & \frac{\tilde{t}^2 - t^2}{t^2 + \tilde{t}^2} \end{pmatrix}, \\ &= -\cos 2\theta - i\sigma_x \sin 2\theta \end{aligned} \tag{4.35}$$

where the diagonal term is the coefficient of the same-spin Andreev reflection $\psi_\uparrow \to \psi_\uparrow^\dagger$, and the off-diagonal term is the coefficient of the spin-flip Andreev reflection $\psi_\uparrow \to \psi_\downarrow^\dagger$. As we change the angle of SOC, θ, from $0\,(\tilde{t}=0)$ to $\pi/4\,(t=\tilde{t})$, the Andreev reflection boundary condition changes continuously from $\psi_{L,s}(0) = -\psi_{R,s}^\dagger(0)$ $(\mathbb{A}\times\mathbb{A})$ to $\psi_{L\uparrow}(0) = -i\psi_{R\downarrow}^\dagger(0)$ and $\psi_{L\downarrow}(0) = -i\psi_{R\uparrow}^\dagger(0)$. We denote this boundary condition for $t=\tilde{t}$ as spin flip Andreev reflection ($\mathbb{SFA}$) boundary condition. Upon increasing θ to $\pi/2$, the boundary condition becomes $\psi_{L,s}(0) = \psi_{R,s}^\dagger(0)(\tilde{\mathbb{A}}\times\tilde{\mathbb{A}})$ (i.e. $t=0$ and $\tilde{t}\neq 0$).

Here we would like to emphasize that the $\mathbb{SFA}$ boundary condition is different from the Andreev boundary condition in s-wave spin-singlet superconducting junction where $\psi_{L\uparrow}(0) = \mp i\psi_{R\downarrow}^\dagger(0)$ and $\psi_{L\downarrow}(0) = \pm i\psi_{R\uparrow}^\dagger(0)$ (see, e.g., Ref. [57]). Notice different signs in this case for spin-up and spin-down components. The $\mathbb{SFA}$ boundary condition in our case corresponds to spin-triplet Andreev reflection which typically is realized at junctions between a normal lead and a spin-triplet p-wave superconductor. Indeed, if we denote spin-triplet pair potential as $\Delta(p) \propto (\overrightarrow{d}(p)\cdot\overrightarrow{\sigma})i\sigma_y$, then different orientations of the $\overrightarrow{d}$-vector correspond to $\mathbb{SFA}$ ($\overrightarrow{d} \propto (0,0,1)$) and $\mathbb{A}\times\mathbb{A}$ ($\overrightarrow{d} \propto (0,\pm 1,0)$) boundary conditions. This difference between conventional (s-wave) spin-singlet Andreev boundary conditions and $\mathbb{SFA}$ boundary conditions considered here becomes very important later when we consider allowed boundary perturbations.

Weak coupling RG analysis near normal reflection fixed point

Now we study the effects of interactions in the lead using RG analysis. In the absence of U(1) spin-rotation symmetry, the boundary Hamiltonian in (4.31) leads to boundary

action after the bosonization,

$$\begin{aligned} S_T &= \int d\tau \Bigg[\frac{t}{2\pi a} \left(i\gamma_\uparrow \Gamma_\uparrow \cos \frac{\theta_\rho + \theta_\sigma}{\sqrt{2}} - i\gamma_\downarrow \Gamma_\downarrow \cos \frac{\theta_\rho - \theta_\sigma}{\sqrt{2}} \right) \\ &+ \frac{\tilde{t}}{2\pi a} \left(i\gamma_\downarrow \Gamma_\uparrow \sin \frac{\theta_\rho + \theta_\sigma}{\sqrt{2}} - i\gamma_\uparrow \Gamma_\downarrow \sin \frac{\theta_\rho - \theta_\sigma}{\sqrt{2}} \right) \\ &- \frac{\Delta}{2\pi a} \gamma_\uparrow \gamma_\downarrow \Gamma_\uparrow \Gamma_\downarrow \cos \sqrt{2}\theta_\sigma + \frac{\tilde{\Delta}}{2\pi v} i\gamma_\uparrow \gamma_\downarrow \frac{i\partial_\tau \theta_\sigma}{\sqrt{2}} \Bigg]. \end{aligned} \tag{4.36}$$

Note the appearance of the new marginal term described by coupling constant $\tilde{\Delta}$. We now perform a perturbative RG analysis up to the second-order in coupling coefficients. The details of the calculations are presented in Appendix B.2. Here we summarize our results for $K_\sigma = 1$:

$$\frac{dt}{dl} = \left(\frac{3}{4} - \frac{1}{4K_\rho} - \frac{\Delta}{4\pi v} \right) t - \frac{\tilde{\Delta}\tilde{t}}{2\pi v}, \tag{4.37}$$

$$\frac{d\tilde{t}}{dl} = \left(\frac{3}{4} - \frac{1}{4K_\rho} + \frac{\Delta}{4\pi v} \right) \tilde{t} - \frac{\tilde{\Delta} t}{2\pi v}, \tag{4.38}$$

$$\frac{d\Delta}{dl} = -\left(\frac{1}{K_\rho} - 1 \right) \frac{t^2 - \tilde{t}^2}{4\pi v}, \tag{4.39}$$

$$\frac{d\tilde{\Delta}}{dl} = -B(K_\rho) \frac{t\tilde{t}}{4\pi v}. \tag{4.40}$$

The generation of the Δ term (proportional to $t^2 - \tilde{t}^2$) originates from the processes involving two different spin channels of the lead whereas the generation of the $\tilde{\Delta}$ term (proportional to $t\tilde{t}$) comes from the processes within the same spin channel. Both of these terms can be generated only in the presence of the interaction in the lead. This fact follows from the definition of the function $B(K_\rho)$

$$B(K_\rho) = \frac{C(1/2K_\rho - 1/2)}{C(1/2)\, C(1/2K_\rho)} \left(\frac{1}{K_\rho} + 1 \right) > 0. \tag{4.41}$$

Here the function $C(\nu)$ is defined as

$$C(\nu) = \lim_{\delta \to 0^+} \int_0^\infty \frac{e^{-\delta z} \cos(z)}{(z+1)^\nu} dz, \tag{4.42}$$

and originates from the integration over relative coordinate, $\tau - \tau'$ during the RG procedure, see Appendix B.2. In the non-interacting limit, $K_\rho \to 1$, $C(\nu \to 0^+) \propto \nu$, and thus, the RG equation for $\tilde{\Delta}$ becomes

$$\frac{d\tilde{\Delta}}{dl} \approx -\frac{c_5}{4\pi v} \left(\frac{1}{K_\rho} - 1 \right) \widetilde{tt}, \tag{4.43}$$

where numerical constant $c_5 \approx 11.5$. As mentioned, both Δ and $\tilde{\Delta}$ cannot be generated in the RG in the absence of interactions in the lead ($K_\rho = 1$).

Using Eq. (4.37) it is instructive to analyze first the flow in the non-interacting limit, in which case $\Delta = \tilde{\Delta} = 0$. Both t and $\tilde{t}$ are relevant and growing under RG. As follows from the discussion in the previous section, the exact boundary condition at the IR fixed point is determined by the initial values of t and $\tilde{t}$ and we can identify the corresponding limits by looking at the scattering matrix, i.e. $t \gg \tilde{t}$ corresponds to $\psi_\sigma(0) = -\psi^\dagger_\sigma(0)$, $t \ll \tilde{t}$ corresponds to $\psi_\sigma(0) = \psi^\dagger_\sigma(0)$ and finally $t = \tilde{t}$ corresponds to $\psi_\sigma(0) = -i\psi^\dagger_{-\sigma}(0)$.

We now analyze the RG flow for not-too-strong repulsive interactions $1/3 \lesssim K_\rho < 1$. First of all, one can notice that even if we start with initial conditions $\Delta(l_0) = 0$, $\tilde{\Delta}(l_0) = 0$, the corresponding four-fermion terms are going to be generated by the RG procedure. Here l_0 is initial length scale. Since the couplings Δ and $\tilde{\Delta}$ affect the RG flow differently, we now have 4-parameter phase diagram. Based on the perturbative RG equations, one can see that both t and $\tilde{t}(l)$ will grow under RG, see Fig. 4.4 (a). Thus, normal reflection fixed point is unstable in this parameter regime.

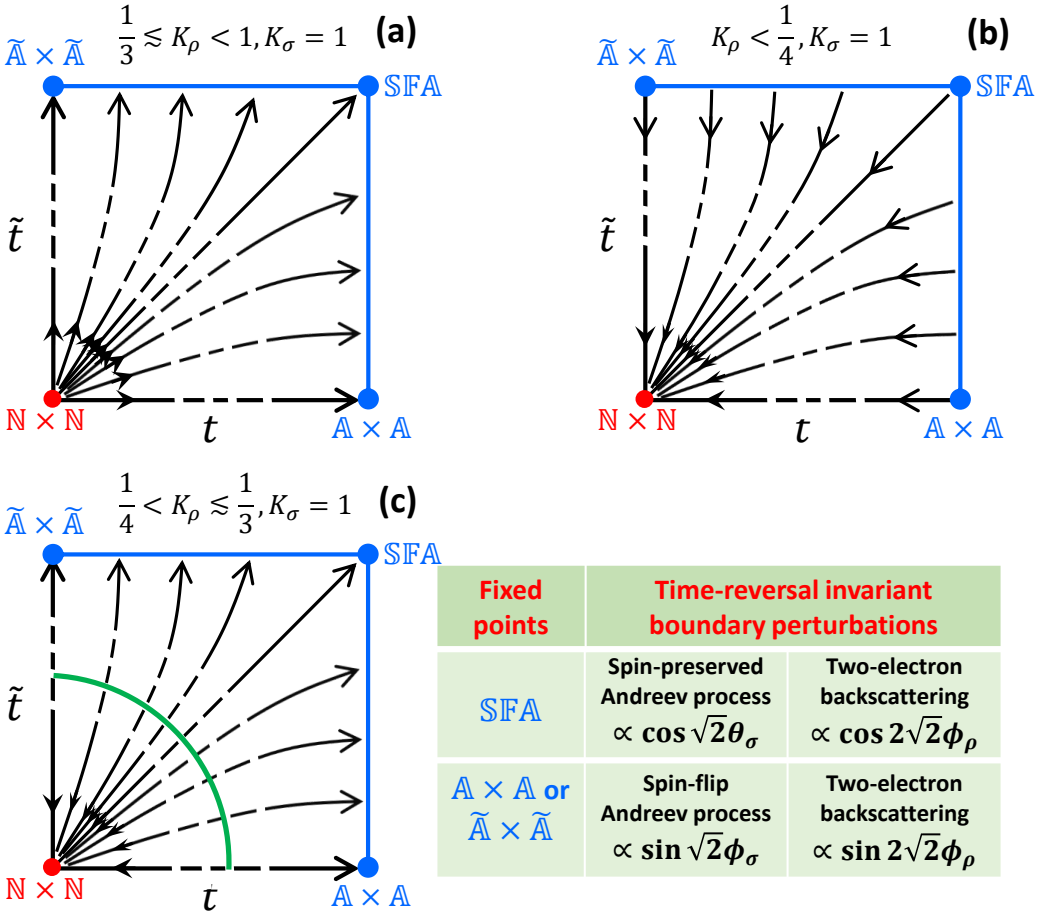

Fixed points	Time-reversal invariant boundary perturbations	
$\mathbb{SFA}$	Spin-preserved Andreev process $\propto \cos\sqrt{2}\theta_\sigma$	Two-electron backscattering $\propto \cos 2\sqrt{2}\phi_\rho$
$\mathbb{A} \times \mathbb{A}$ or $\widetilde{\mathbb{A}} \times \widetilde{\mathbb{A}}$	Spin-flip Andreev process $\propto \sin\sqrt{2}\phi_\sigma$	Two-electron backscattering $\propto \sin 2\sqrt{2}\phi_\rho$

Figure 4.4: RG flow diagram for the junction without $U(1)$ symmetry: (a) for $1/3 < K_\rho < 1$ and $K_\sigma = 1$, (b) for $K_\rho < 1/4$ and $K_\sigma = 1$, and (c) for $1/4 < K_\rho \lesssim 1/3$ and $K_\sigma = 1$, and the green line indicates the conjectured BKT phase transition. The inset table summarizes the important time-reversal invariant boundary perturbations near $\mathbb{SFA}$, $\mathbb{A} \times \mathbb{A}$, and $\tilde{\mathbb{A}} \times \tilde{\mathbb{A}}$ fixed points. For $K_\sigma = 1$, along each line of the RG flow, the phase diagram as a function of K_ρ is similar to the that shown in Fig. 4.2.

RG analysis near spin-flip Andreev reflection fixed point

We now analyze the stability of the spin-flip Andreev reflection $\mathbb{SFA}$ fixed point which corresponds to the following boundary conditions:

$$\psi_{L\uparrow}(0) = -i\psi^\dagger_{R\downarrow}(0), \tag{4.44}$$

$$\psi_{L\downarrow}(0) = -i\psi^\dagger_{R\uparrow}(0). \tag{4.45}$$

In terms of the bosonization language, the boson fields $\phi_\sigma(0) = 0$ and $\theta_\rho(0) = -\pi/(2\sqrt{2})$ are pinned, and the Klein factors have the relation $\Gamma_{\uparrow L} = \Gamma_{\downarrow R}$ and $\Gamma_{\downarrow L} = \Gamma_{\uparrow R}$. Now we study all the fermion bilinear perturbations at the boundary allowed by TR symmetry. First, one can show that the normal backscattering is not allowed in this case, in agreement with the scattering matrix calculation in Sec. 4.2.2. Indeed, using the boundary condition (4.44) one can show that

$$\begin{aligned}\psi^\dagger_{L\uparrow}(0)\psi_{\uparrow,R}(0) + \psi^\dagger_{R\downarrow}(0)\psi_{L\downarrow}(0) + h.c. &= -i\psi^\dagger_{L\uparrow}(0)\psi^\dagger_{L\downarrow}(0) + i\psi_{L\uparrow}(0)\psi_{L\downarrow}(0) + h.c. \\ &= 0\end{aligned} \tag{4.46}$$

Note that for s-wave spin-singlet superconductor the boundary conditions are different:

$$\psi_{L\uparrow}(0) = \mp i\psi^\dagger_{R\downarrow}(0) \text{ and } \psi_{L\downarrow}(0) = \pm i\psi^\dagger_{R\uparrow}(0), \tag{4.47}$$

and the backscattering term $\sim \sin\sqrt{2}\phi_\rho$ does not vanish. Since this term is relevant for $K_\rho < 1$, the Andreev reflection fixed point is unstable in an s-wave superconductor-LL junction.

Let us now consider the allowed operators. The only allowed bilinear term is spin-

conserving Andreev reflection:

$$\begin{aligned} H_{1B}^{SFA} &= \lambda_1^{SFA}(\psi_{L\uparrow}^\dagger \psi_{\uparrow,R}^\dagger + \psi_{R\downarrow}^\dagger \psi_{L\downarrow}^\dagger + h.c.) \\ &= \lambda_1^{SFA}(i\psi_{L\uparrow}^\dagger \psi_{L\downarrow} + i\psi_{R\downarrow}^\dagger \psi_{\uparrow,R} + h.c.) \\ &= 2\frac{\lambda_1^{SFA}}{2\pi a}\left(i\Gamma_{L\uparrow}\Gamma_{L\downarrow} + i\Gamma_{R\downarrow}\Gamma_{R\uparrow}\right)\cos\sqrt{2}\theta_\sigma. \end{aligned} \tag{4.48}$$

Additionally, we also consider the following four-fermion term

$$\begin{aligned} H_{2B}^{SFA} &= \frac{\lambda_2^{SFA}}{(2\pi a)^2}(\psi_{L\uparrow}^\dagger \psi_{R\uparrow} \psi_{L\downarrow}^\dagger \psi_{R\downarrow} + h.c.) \\ &= 2\lambda_2^{SFA}\,\Gamma_{L\uparrow}\Gamma_{R\uparrow}\Gamma_{L\uparrow}\Gamma_{L\downarrow}\Gamma_{R\downarrow}\cos 2\sqrt{2}\phi_\rho, \end{aligned} \tag{4.49}$$

which corresponds to two-electron backscattering. The leading order perturbative RG equations for λ_1^{SFA} and λ_2^{SFA} are give by

$$\frac{d\lambda_1^{SFA}}{dl} = \left(1 - \frac{1}{K_\sigma}\right)\lambda_1^{SFA}, \tag{4.50}$$

$$\frac{d\lambda_1^{SFA}}{dl} = (1 - 4K_\rho)\lambda_2^{SFA}. \tag{4.51}$$

One can see that the first term λ_1^{SFA} is marginal for $\mathbb{SU}(2)$ symmetric LL with $K_\sigma = 1$ while the second coupling becomes relevant for $K_\rho < 1/4$ indicating that the $\mathbb{SFA}$ fixed point becomes unstable for strong repulsive interactions. If the $SU(2)$ spin symmetry is broken in the lead, the $\mathbb{SFA}$ fixed point becomes unstable for $K_\sigma > 1$, and the system will flow towards the $\mathbb{A} \times \mathbb{A}$ fixed point. On the other hand, the $\mathbb{SFA}$ is stable for $K_\sigma < 1$.

RG analysis near spin-conserving Andreev fixed point

As shown in Sec. 4.2.2, the boundary conditions near $\mathbb{A} \times \mathbb{A}$ or $\tilde{\mathbb{A}} \times \tilde{\mathbb{A}}$ fixed point are $\psi_{L,s}(0) = e^{i\alpha}\psi_{R,s}^\dagger(0)$ with $\alpha = \pi$ or 0. Thus, the boson fields are $\theta_\rho = \pm\pi/\sqrt{2}$ and $\theta_\sigma = 0$

are pinned at the boundary, and the Klein factors satisfy the relations $\Gamma_{L,s} = \Gamma_{R,s}$. In the $\mathbb{U}(1)$-conserving case, we have seen that the leading perturbations for $1/3 < K_\rho < 1$ is the two-electron backscattering

$$\begin{aligned} H_{2B}^{A\times A} =& \lambda_2^{A\times A}\psi_{L\uparrow}^\dagger(0)\psi_{R\uparrow}(0)\psi_{L\downarrow}^\dagger(0)\psi_{R\downarrow}(0) + h.c. \\ =& \frac{\lambda_2}{(2\pi a)^2}\sin(2\sqrt{2}\phi_\rho). \end{aligned} \tag{4.52}$$

In addition, if $\mathbb{U}(1)$ symmetry is broken, the spin-flip Andreev reflection is allowed

$$\begin{aligned} H_{1B}^{A\times A} &= \lambda_1^{A\times A}\psi_{R,\uparrow}^\dagger(0)\psi_{L,\downarrow}^\dagger(0) - \psi_{R,\downarrow}^\dagger(0)\psi_{L,\uparrow}^\dagger(0) + h.c. \\ &= 4i\lambda_1^{A\times A}\Gamma_\uparrow\Gamma_\downarrow \sin\sqrt{2}\phi_\sigma. \end{aligned} \tag{4.53}$$

The leading order perturbative RG equations for $\lambda_1^{A\times A}$ and $\lambda_2^{A\times A}$ are give by

$$\frac{d\lambda_1^{A\times A}}{dl} = (1-K_\sigma)\lambda_1^{A\times A}, \tag{4.54}$$

$$\frac{d\lambda_2^{A\times A}}{dl} = (1-4K_\rho)\lambda_2^{A\times A}. \tag{4.55}$$

One can see that the first term $\lambda_1^{A\times A}$ is marginal for $SU(2)$ symmetric LL $K_\sigma = 1$, whereas the second coupling becomes relevant for $K_\rho < 1/4$ indicating that $\mathbb{A}\times\mathbb{A}$ fixed point becomes unstable for strong repulsive interactions. If the $SU(2)$ spin symmetry is broken in the lead, the $\mathbb{A}\times\mathbb{A}$ fixed point becomes unstable for $K_\sigma < 1$, and the system will flow towards the $\mathbb{SFA}$ fixed point. On the other hand, the $\mathbb{A}\times\mathbb{A}$ is stable for $K_\sigma > 1$. Exactly at $K_\sigma = 1$, both $\lambda_1^{A\times A}$ and λ_1^{SFA} terms are marginal and compete with each other. Thus, generically both spin-conserving and spin-flip Andreev reflection processes will be present and their relative strength depends on microscopic details. This conclusion is consistent with the non-interacting results ($K_\rho = 1$) discussed in Sec.4.2.2.

Our main results are summarized in Fig. 4.4.

4.3 Majorana Kramers pair-quantum dot-normal lead system

4.3.1 Theoretical model

In this section we study effect of local electron-electron interactions and consider the system consisting of a QD with a single spin-degenerate level coupled to a MKP $\gamma_{\uparrow,\downarrow}$, localized at the end of a TRI topological superconductor, and a NL. The schematic plot of the device is shown in Fig. 4.1 b). Assuming that TR symmetry and $\mathbb{U}(1)$-spin rotation symmetry are preserved and the induced gap in the topological superconductor is sufficiently larger than other energy scales of the problem, the low-energy effective Hamiltonian of the system can be written as

$$H = \sum_{\sigma} \epsilon d_{\sigma}^{\dagger} d_{\sigma} + U n_{\uparrow} n_{\downarrow} + V + H_{NL} \tag{4.56}$$

$$V = \sum_{\sigma} [i\lambda_{\sigma}\gamma_{\sigma}(d_{\sigma} + d_{\sigma}^{\dagger}) + t_{\sigma}(d_{\sigma}^{\dagger}\psi_{\sigma}(0) + \text{h.c.})] \tag{4.57}$$

where $d_{\sigma}^{\dagger}$ and d_{σ} are creation and annihilation operators on the QD, $n_{\sigma} = d_{\sigma}^{\dagger} d_{\sigma}$, ϵ is the chemical potential of the QD, U is the strength of the electron-electron interaction on the QD, $\psi_{\sigma}^{\dagger}$ and ψ_{σ} are fermion creation and annihilation operators in the NL, and $t(\lambda_{\sigma})$ is the tunneling coefficient between the NL(MKP) and the QD. For the perturbative RG analysis, we adopted the same Hamiltonian for NL as Eq. (4.3) with $K_{\rho} = K_{\sigma} = 1$. For slave-boson mean-field theory analysis, we assumed quadratic dispersion ξ_k for the NL. We set t_{σ} and λ_{σ} to be real. Time-reversal symmetry requires $t_{\uparrow} = t_{\downarrow} = t$ and $\lambda_{\uparrow} = -\lambda_{\downarrow} = \lambda$. The Hamiltonian H_{NL} represents semi-infinite NL ($x \geq 0$) with hopping

t_0. We are interested in the limit where $\epsilon < 0$, $U + \epsilon > 0$ such that the QD favors single occupation, and weak coupling regime $|t|, |\lambda| \ll \min(-\epsilon, U - \epsilon)$. In this limit, one can simplify the effective Hamiltonian by projecting it onto single-occupation subspace [86]. The projection operators to the n-occupation subspace P_n are given by

$$P_0 = (1 - n_\uparrow)(1 - n_\downarrow), \tag{4.58}$$

$$P_1 = ((1 - n_\uparrow)n_\downarrow + (1 - n_\downarrow)n_\uparrow, \tag{4.59}$$

$$P_2 = n_\uparrow n_\downarrow. \tag{4.60}$$

Then, the effective Hamiltonian can be written as

$$H_{\text{eff}} = H_{11} + \sum_{n=0,2} H_{1n} \frac{1}{E - H_{nn}} H_{n1}, \tag{4.61}$$

where

$$H_{mn} = P_m H P_n. \tag{4.62}$$

After some algebra, we find

$$H_{11} = H_{NL} \tag{4.63}$$

$$H_{01} = \sum_\sigma (t\psi_\sigma^\dagger + i\lambda_\sigma \gamma_\sigma) d_\sigma (1 - n_{-\sigma}), \tag{4.64}$$

$$H_{10} = \sum_\sigma (-t\psi_\sigma + i\lambda_\sigma \gamma_\sigma) d_\sigma^\dagger (1 - n_{-\sigma}), \tag{4.65}$$

$$H_{12} = \sum_\sigma (t\psi_\sigma^\dagger + i\lambda_\sigma \gamma_\sigma) d_\sigma n_{-\sigma}, \tag{4.66}$$

$$H_{21} = \sum_\sigma (-t\psi_\sigma + i\lambda_\sigma \gamma_\sigma) d_\sigma^\dagger n_{-\sigma}. \tag{4.67}$$

Using the Eq. (4.61) with the low energy assumption $E \ll \min(-\epsilon, U-\epsilon)$, we get second order in t and λ corrections to the Hamiltonian:

$$H_{12}\frac{1}{E-H_{22}}H_{21} = \frac{1}{|\epsilon|-U}\sum_{\sigma,\sigma'}\left[t^2\psi^\dagger_\sigma\psi_{\sigma'} + \lambda_\sigma\lambda_{\sigma'}\gamma_\sigma\gamma_{\sigma'} + i\lambda_\sigma t\gamma_\sigma\psi_{\sigma'} + i\lambda_{\sigma'}t\gamma_{\sigma'}\psi^\dagger_\sigma\right] \times d_\sigma n_{-\sigma}d^\dagger_{\sigma'}n_{-\sigma'} \tag{4.68}$$

$$H_{10}\frac{1}{E-H_{00}}H_{01} = -\frac{1}{|\epsilon|}\sum_{\sigma,\sigma'}\left[t^2\psi_\sigma\psi^\dagger_{\sigma'} + \lambda_\sigma\lambda_{\sigma'}\gamma_\sigma\gamma_{\sigma'} - i\lambda_\sigma t\gamma_\sigma\psi^\dagger_{\sigma'} - i\lambda_{\sigma'}t\gamma_{\sigma'}\psi_\sigma\right] \times d^\dagger_\sigma\bar{n}_{-\sigma}d_{\sigma'}\bar{n}_{-\sigma'}, \tag{4.69}$$

where $\bar{n}_\sigma = 1-n_\sigma$. Finally, we obtain the effective Hamiltonian $H = H_{\rm NL} + H_b$ with the boundary Hamiltonian H_b being

$$H_b = \xi_+\left[\frac{t^2}{2}\mathbf{S}\cdot\mathbf{s}(0) - \frac{\lambda^2}{2}S_yS^\gamma_y + \frac{i\lambda t}{2}\Big(\gamma_\uparrow(\psi_\uparrow+\psi^\dagger_\uparrow)S_z + \gamma_\downarrow(\psi_\downarrow+\psi^\dagger_\downarrow)S_z + \gamma_\uparrow(\psi_\downarrow S^- + \psi^\dagger_\downarrow S^+) - \gamma_\downarrow(\psi_\uparrow S^+ + \psi^\dagger_\uparrow S^-)\Big)\right] + \xi_-\left[\frac{i\lambda t}{2}\Big(\gamma_\uparrow(\psi_\uparrow+\psi^\dagger_\uparrow) - \gamma_\downarrow(\psi_\downarrow+\psi^\dagger_\downarrow)\Big)\right], \tag{4.70}$$

where

$$\mathbf{S} = d^\dagger_\alpha\boldsymbol{\sigma}_{\alpha\beta}d_\beta, \quad \mathbf{s}(\mathbf{0}) = \psi^\dagger_\alpha(0)\boldsymbol{\sigma}_{\alpha\beta}\psi_\beta(0), \quad \mathbf{S}^\gamma = \gamma_\alpha\boldsymbol{\sigma}_{\alpha\beta}\gamma_\beta,$$
$$S^+ = S_x + iS_y, \quad S^- = S_x - iS_y, \tag{4.71}$$

and the coefficients $\xi_\pm$ are defined as

$$\xi_\pm = \frac{1}{|\epsilon|} \pm \frac{1}{U-|\epsilon|}. \tag{4.72}$$

In the limit $\lambda \to 0$, the first term $\sim t^2$ drives the system to the Kondo fixed point where a spin in QD and a spin in the lead form a spin-singlet state. In the presence of the Majorana coupling λ, the other terms in the Hamiltonian appear. These Majorana-induced couplings favor the strong-correlation between QD spin and MKP, and, as a result, compete with Kondo coupling.

The critical difference between the present Hamiltonian (4.70) and that of time-reversal broken case with single MZM in Ref. [10], is the presence of the four fermion interaction term proportional to λ^2. This time-reversal preserving interaction term between QD and MKP replaces the Zeeman-like coupling in the single MZM case. While the Zeeman-like coupling becomes zero at the particle-hole symmetric point in the previous study [10], this interaction term is proportional to ξ_+ and is always non-zero for any position of the level ϵ in the dot. Therefore, one cannot apply the same method as in Ref. [10] to find the exact solution at the particle-hole symmetric point. To understand low-energy properties of the system, we present below the results from two complementary calculations: perturbative RG analysis and slave-boson mean field theory in the limit of infinite U.

4.3.2 Weak coupling RG analysis for quantum dot

In order to understand the effect of Majorana induced interaction on the IR fixed point the system flows to, we study RG flow of the boundary couplings in the weak-coupling limit. First, we introduce the following rescaled couplings: $M(l_0) = \xi_+\lambda^2$, $T_1(l_0) = \lambda t\xi_-$, $T_2(l_0) = \lambda t\xi_+$ and $J(l_0) = t^2\xi_+$. After the standard bosonization procedure and the

rescaling of the parameters, we obtain the following effective action at the boundary:

$$\begin{aligned} S_b = \int \frac{d\tau}{2\pi a} \Bigg\{ & iM\gamma_\uparrow\gamma_\downarrow S_y + iT_1 \left[\gamma_\uparrow\Gamma_\uparrow \cos\left(\frac{\theta_\rho+\theta_\sigma}{\sqrt{2}}\right) - \gamma_\downarrow\Gamma_\downarrow \cos\left(\frac{\theta_\rho-\theta_\sigma}{\sqrt{2}}\right)\right] \\ & + iT_2^z S_z \left[\gamma_\uparrow\Gamma_\uparrow \cos\left(\frac{\theta_\rho+\theta_\sigma}{\sqrt{2}}\right) + \gamma_\downarrow\Gamma_\downarrow \cos\left(\frac{\theta_\rho-\theta_\sigma}{\sqrt{2}}\right)\right] \\ & + iT_2^\perp \Bigg[\gamma_\uparrow\Gamma_\downarrow \left(S_x \cos\left(\frac{\theta_\rho-\theta_\sigma}{\sqrt{2}}\right) + S_y \sin\left(\frac{\theta_\rho-\theta_\sigma}{\sqrt{2}}\right)\right) \\ & - \gamma_\downarrow\Gamma_\uparrow \left(S_x \cos\left(\frac{\theta_\rho+\theta_\sigma}{\sqrt{2}}\right) - S_y \sin\left(\frac{\theta_\rho+\theta_\sigma}{\sqrt{2}}\right)\right)\Bigg] \\ & - \frac{iaJ^z S_z}{\sqrt{2}v}\partial_\tau\theta_\sigma - iJ^\perp\Gamma_\uparrow\Gamma_\downarrow \left(S_x \sin\sqrt{2}\theta_\sigma + S_y \cos\sqrt{2}\theta_\sigma\right) \Bigg\} \end{aligned} \tag{4.73}$$

Here we have introduced couplings $T_2^{z,\perp}$ and $J^{z,\perp}$ for RG procedure. Once we set $T_2^z(l_0) = T_2^\perp(l_0)$ and $J^z(l_0) = J^\perp(l_0)$, we recover the spin-rotation symmetry. We will focus on the limit of non-interacting lead, but adding small repulsive interaction in NL does not change our conclusion.

Let us now perform perturbative RG analysis up to the second order in couplings near normal reflection fixed point. The procedure of the calculations is similar to the one presented in Appendix B.1 and B.2. The RG equations for the couplings read

$$\frac{dM}{dl} = M + \frac{T_2^2}{\pi v} \tag{4.74}$$

$$\frac{dT_1}{dl} = \frac{T_1}{2} \tag{4.75}$$

$$\frac{dT_2}{dl} = \frac{T_2}{2} + \frac{T_2 J}{\pi v} \tag{4.76}$$

$$\frac{dJ}{dl} = \frac{J^2}{\pi v} \tag{4.77}$$

From these RG equations, we can see that the Majorana interaction, M, is the most relevant coupling while the Kondo coupling, J, is only marginally relevant. Thus, the system generically flows to the strong Majorana correlation fixed point. If initially

$M(l_0) \ll J(l_0)$, the system can still reach the Kondo strong coupling fixed point. One can estimate the crossover scale, λ_c, by solving $M(l^*) = J(l^*) \sim 1$ (l^* is the crossover length scale) which leads to the following estimate for the critical coupling

$$\lambda_c \sim \frac{1}{\xi_+} \exp\left(-\frac{\pi v}{2\xi^+ t^2}\right), \tag{4.78}$$

which defines a crossover between the two regimes. In deriving this estimate, we have ignored the second order contributions from T_2^2 term assuming that it is small.

Let us now study the nature of the strong Majorana correlation fixed point defined by $M(l^*) \sim 1$ and $J(l^*) \ll 1$. The two degenerate (Kramers) states that minimize $iM\gamma_\uparrow\gamma_\downarrow S_y$ term are

$$|\psi_1\rangle = |i\gamma_\uparrow\gamma_\downarrow = -1, S_y = 1\rangle \text{ and } |\psi_2\rangle = |i\gamma_\uparrow\gamma_\downarrow = 1, S_y = -1\rangle. \tag{4.79}$$

Assuming that $M(l^*)$ is large, one can project the rest of the boundary terms on to this low-energy manifold and simplify the boundary problem. Since the ground state is an eigenstate of S_y and $i\gamma_\uparrow\gamma_\downarrow$, the terms that are proportional to $\gamma \otimes I$ and $\gamma \otimes S_y$ will be projected to zero. The remaining boundary terms at particle-hole symmetric point (i.e. $T_1 = 0$) are

$$H_M = iT_2(l^*)\left[\beta_\uparrow(\psi_\uparrow + \psi_\uparrow^\dagger) - \beta_\downarrow(\psi_\downarrow + \psi_\downarrow^\dagger)\right] + \frac{iJ(l^*)}{2}\beta_\uparrow\beta_\downarrow(-i\psi_\uparrow^\dagger\psi_\downarrow + i\psi_\downarrow^\dagger\psi_\uparrow), \tag{4.80}$$

where we have introduced generalized Majorana operators $\beta_\uparrow = (\gamma_\uparrow S_z - \gamma_\downarrow S_x)/2$ and $\beta_\downarrow = -(\gamma_\downarrow S_z + \gamma_\uparrow S_x)/2$. Note that these new Majorana operators follow the Majorana operator algebra only in the degenerate ground states manifold. One can notice that the above effective Hamiltonian (4.80) is exactly the same as that in Eq. (4.8) with $K_\rho = 1$ and $\delta = 0$. Therefore, using the results from the previous section and the condition

$T_2(l^*) \gg J(l^*)$, we can immediately conclude that the system will flow to the IR fixed point governed by the $\mathbb{A} \times \mathbb{A}$ boundary condition $\psi_\sigma(0) = -\psi_\sigma^\dagger(0)$.

As follows from the RG analysis, the coupling of QD to MKP leads to a non-trivial many-body ground-state where the spin on the QD gets entangled with the fermion parity of the MKP. Due to the change in the boundary conditions for lead electrons, the zero-bias tunneling conductance is $G = 4e^2/h$ due to perfect Andreev reflection phenomenon. Further insight about the physical properties of the system can be obtained using a complementary approach - slave-boson mean field theory.

4.3.3 Slave-boson mean field theory

In this section, we develop a slave-boson mean field theory for MKP-QD-NL junction with infinite repulsive interaction in QD, $U \to \infty$. In this limit, one can completely exclude the double occupancy state from the Hilbert space, and one can represent the creation and annihilation operators for the QD as $d_\sigma^\dagger \to f_\sigma^\dagger b$ and $d_\sigma \to f_\sigma b^\dagger$ with an additional constraint [63]

$$b^\dagger b + \sum_\sigma f_\sigma^\dagger f_\sigma = 1 \tag{4.81}$$

where b is a boson operator representing an empty state. Thus, the effective action of the system in terms of new fields variables reads

$$\begin{aligned} S_{\rm sb} = \int d\tau \sum_\sigma \Bigg[& \sum_k \psi_{k,\sigma}^*(\partial_\tau + \xi_k)\psi_{k,\sigma} + f_\sigma^*(\partial_\tau + \epsilon) f_\sigma + i\lambda_\sigma \gamma_\sigma^1 (f_\sigma b^* + f_\sigma^* b) \\ & + \sum_k t(f_\sigma^* \psi_{k,\sigma} b + \psi_{k,\sigma}^* f_\sigma b^*) + \frac{1}{2} b^* \partial_\tau b + \frac{1}{2} \sum_{i=1,2} \gamma_\sigma^i \partial_\tau \gamma_\sigma^i \\ & + i\delta_{1\sigma} \gamma_\sigma^1 \gamma_\sigma^2 + i\delta_2 \gamma_\sigma^1 \gamma_{-\sigma}^2 + \eta \left(\frac{b^* b - 1}{2} + f_\sigma^* f_\sigma \right) \Bigg], \end{aligned} \tag{4.82}$$

where η is the Lagrange multiplier that we have introduced for the constraint. Here we consider a realistic situation where the TRI topological superconductor has a finite length. γ^1 and γ^2 correspond to the Majorana modes at the end near the QD and at the opposite end. $\delta_{1\uparrow} = -\delta_{1\downarrow} = \delta_1$ and δ_2 represent mixing between the MKPs at the opposite ends.

Mean-field solution

We now develop self-consistent mean-field theory for the problem. We first replace boson fields in Eq. (4.82) with their mean-field value $\langle b \rangle = \langle b^* \rangle = b$ and solve for b and η. Here, without loss of generality, we assumed that b is real since the phase can be gauged away by fixing the internal $\mathbb{U}(1)$ gauge. In the next section, we will study effect fluctuations around the mean-field saddle point and the meaning of breaking $\mathbb{U}(1)$ gauge symmetry in this low-dimensional system.

The mean-field equations can be obtained by minimizing the action (4.82):

$$\frac{\partial S}{\partial \eta} = b^2 + \sum_\sigma \langle f_\sigma^* f_\sigma \rangle - 1 = 0 \tag{4.83}$$

$$\frac{\partial S}{\partial b} = 2b\eta + t \sum_{k,\sigma} (\langle f_\sigma^* \psi_{k,\sigma} \rangle + \langle \psi_{k,\sigma}^* f_\sigma \rangle) + i \sum_\sigma \lambda_\sigma \langle \gamma_\sigma^1 (f_\sigma^* + f_\sigma) \rangle = 0 \tag{4.84}$$

The details of the calculation of the correlation functions are presented in the Appendix C.1. We first consider the limit $T, \delta_1, \delta_2 \to 0$ and assume that $|\epsilon| \gg |\lambda|, |t|$ such that the probability for empty state in QD b^2 is small. In this limit, the first equation becomes

$$\epsilon + \eta \approx \frac{\pi}{2} \Gamma b^4, \tag{4.85}$$

where $\Gamma = \pi \nu_F |t|^2$. Substituting $\eta \approx -\epsilon$ back into Eq.(4.84) and neglecting terms $O(b^4)$,

one finds

$$\eta - \frac{2\Gamma}{\pi} \ln \frac{\Lambda}{\Gamma b^2} - \frac{|\lambda|}{\sqrt{2}b} = 0. \tag{4.86}$$

For $\lambda \to 0$ we recover the solution for the Kondo-dominated regime:

$$T_K \equiv \Gamma b^2 = \Lambda e^{-\frac{\pi|\epsilon|}{2\Gamma}}. \tag{4.87}$$

If Majorana coupling $\lambda \gg \lambda_c$, b is determined by the last term in Eq. (4.86):

$$b \approx \frac{|\lambda|}{\sqrt{2}|\epsilon|}. \tag{4.88}$$

The crossover between two regimes occurs at

$$\lambda_c \approx \sqrt{\frac{2\Lambda}{\Gamma}} |\epsilon| e^{-\frac{\pi|\epsilon|}{4\Gamma}} \tag{4.89}$$

which qualitatively agrees with the estimate for λ_c from the RG analysis, see Eq. (4.78).

In the presence of the Majorana splitting δ_1 and δ_2, we can solve the mean-field equations numerically. In terms of $\delta_1^2 + \delta_2^2 \equiv \delta^2$, the second mean-field equation(4.84) now becomes

$$\frac{|\epsilon|}{\Gamma} - \frac{2}{\pi} \ln \frac{\Lambda}{\Gamma b^2} - 2I(b, \tilde{\lambda}, \tilde{\delta}) = 0, \tag{4.90}$$

where

$$I(b,\tilde{\lambda}, \tilde{\delta}) = \frac{b^2 \tilde{\lambda}^2}{\pi} \times \int_0^\infty dx \frac{x(x - \tilde{\delta}^2 - b^2\tilde{\lambda}^2)}{(x + b^4)(x(x - \tilde{\delta}^2 - 2b^2\tilde{\lambda}^2)^2 + b^4(x - \tilde{\delta}^2)^2)} \tag{4.91}$$

One can numerically solve the Eq. (4.90) for self-consistent solution b as a function of $\tilde{\lambda} = \lambda/\Gamma$ and $\tilde{\delta} = \delta/\Gamma$, see Fig. 4.5 for results. One can see that if we increase the splitting

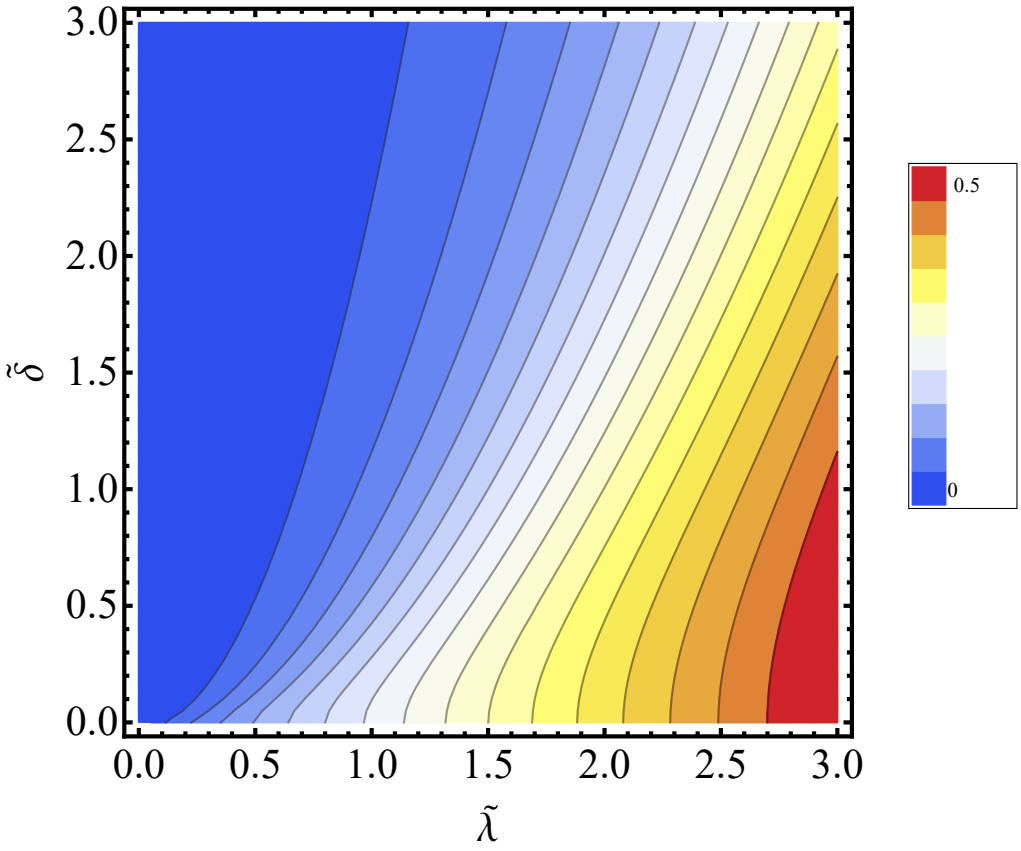

Figure 4.5: The solution b of the mean-field equation as a function of $\tilde{\lambda}$ and $\tilde{\delta}$. We set $\epsilon = -6\Gamma$ and $\Lambda = 50\Gamma$.

for Majoranas δ, the Kondo correlations become more important and eventually start to dominate. As a result, the magnitude of λ_c defining the crossover between two different fixed points is increased.

Gaussian fluctuations around mean-field solution

We now analyze the stability of the mean-field solutions with respect to fluctuations. This issue is rather subtle, and has been discussed extensively in the context of the Kondo problems [78, 77, 16]. Indeed, one can check that the action (4.82) is invariant with respect to local gauge transformations $b \to be^{i\theta}$ and $f \to e^{i\theta} f$. The mean-field solution appears to break this $\mathbb{U}(1)$ symmetry. However, as we will show below, the fluctuations will restore this symmetry.

We now make a transformation to the "radial coordinates" and rewrite $b(\tau) = s(\tau)e^{i\theta(\tau)}$. One can check that the action (4.82) is invariant with respect to local gauge transformations $s \to s$, $f \to e^{i\theta} f$ and $\eta(\tau) \to \eta + i\partial_\tau \theta$. Therefore, we can absorb the phase into η and expand the action in terms of fluctuations $\delta s(\tau)$ and $\delta\eta(\tau) = i\partial_\tau\theta(\tau)$ such that

$$s(\tau) = \bar{s} + \delta s(\tau), \quad \eta(\tau) = \bar{\eta} + i\partial_\tau\theta(\tau), \tag{4.92}$$

around the corresponding saddle point. Here $\bar{s}$ is the mean-field solution for b, defined in the previous section. After integrating out fermions, the effective action can be written in the following form

$$S_{\text{eff}} = -\operatorname{Tr}\ln\left[\mathcal{G}^{-1}(s,\eta)\right] + \int d\tau \left[\eta(s^2-1) + s\partial_\tau s\right] \tag{4.93}$$

After we introduce the Fourier transform

$$\delta s(\tau) = \frac{1}{\beta}\sum_{\nu} \delta s_{\nu} e^{-i\omega_{\nu}\tau}, \quad \dot{\theta}(\tau) = \frac{1}{\beta}\sum_{\nu} \dot{\theta}_{\nu} e^{-i\omega_{\nu}\tau} \tag{4.94}$$

with bosonic Matsubara frequency $\omega_\nu = 2\pi\nu/\beta$, we can expand the $\mathrm{Tr}\ln[\mathcal{G}^{-1}(s,\eta)]$ around the mean field solution in Matsubara frequency space up to the second order in δs and $\partial_\tau\theta$.

$$\begin{aligned} S^{(2)}_{\mathrm{eff}} = &-\frac{2}{\beta^2}\sum_{n>0,\nu} \mathrm{Tr}\left[\mathcal{G}_n(\bar{s},\bar{\eta})\delta\mathcal{G}^{-1}_{2,n,\nu}\right] + \frac{1}{\beta^2}\sum_{n>0,\nu} \mathrm{Tr}\left[\mathcal{G}_n(\bar{s},\bar{\eta})\delta\mathcal{G}^{-1}_{1,n,-\nu}\mathcal{G}_{n+\nu}(\bar{s},\bar{\eta})\delta\mathcal{G}^{-1}_{1,n,\nu}\right] \\ &+ \frac{1}{\beta}\sum_{\nu}\left[\delta s_{-\nu}(-i\omega_\nu + \bar{\eta})\delta s_\nu + 2i\bar{s}\delta\dot{\theta}_{-\nu}\delta s_\nu\right] \end{aligned} \tag{4.95}$$

where the correlation functions are defined as

$$\mathcal{G}_n(\bar{s},\bar{\eta})_{1,1} = -(G^{-1}_{f,n}\tilde{G}^{-1}_{f,n}\big|_{\bar{s},\bar{\eta}} - \bar{s}^4 G^2_{\gamma,n})^{-1}\tilde{G}^{-1}_{f,n} \equiv -G^p_n \tag{4.96}$$

$$\mathcal{G}_n(\bar{s},\bar{\eta})_{1,2} = -(G^{-1}_{f,n}\tilde{G}^{-1}_{f,n}\big|_{\bar{s},\bar{\eta}} - \bar{s}^4 G^2_{\gamma,n})^{-1}\bar{s}^2 G_{\gamma,n} \equiv -\Delta_\sigma \tag{4.97}$$

$$\mathcal{G}_n(\bar{s},\bar{\eta})_{2,1} = \mathcal{G}_n(\bar{s},\bar{\eta})_{1,2} \equiv -\Delta_n \tag{4.98}$$

$$\mathcal{G}_n(\bar{s},\bar{\eta})_{2,2} = -(G^{-1}_{f,n}\tilde{G}^{-1}_{f,n}\big|_{\bar{s},\bar{\eta}} - \bar{s}^4 G_{\gamma,n}G_{\gamma,n})^{-1}G^{-1}_{f,n} \equiv -G^h_n, \tag{4.99}$$

and

$$\delta\mathcal{G}^{-1}_{1,n,-\nu} = \begin{pmatrix} i\dot{\theta}_{-\nu}+\delta s_{-\nu}(G_{\psi,n+\nu}+G_{\psi,n})\bar{s} & 0 \\ 0 & -i\dot{\theta}_{-\nu}+\delta s_{-\nu}(\tilde{G}_{\psi,n+\nu}+\tilde{G}_{\psi,n})\bar{s} \end{pmatrix} + \begin{pmatrix} \delta s_{-\nu}(G_{\gamma,n+\nu}+G_{\gamma,n})\bar{s} & \delta s_{-\nu}(G_{\gamma,n+\nu}+G_{\gamma,n})\bar{s} \\ \delta s_{-\nu}(G_{\gamma,n+\nu}+G_{\gamma,n})\bar{s} & \delta s_{-\nu}(G_{\gamma,n+\nu}+G_{\gamma,n})\bar{s} \end{pmatrix}, \tag{4.100}$$

$$\delta\mathcal{G}^{-1}_{1,n,\nu} = \begin{pmatrix} i\dot{\theta}_{\nu}+\delta s_{\nu}(G_{\psi,n}+G_{\psi,n+\nu})\bar{s} & 0 \\ 0 & -i\dot{\theta}_{\nu}+\delta s_{\nu}(\tilde{G}_{\psi,n}+\tilde{G}_{\psi,n+\nu})\bar{s} \end{pmatrix} + \begin{pmatrix} \delta s_{\nu}(G_{\gamma,n+\nu}+G_{\gamma,n})\bar{s} & \delta s_{\nu}(G_{\gamma,n+\nu}+G_{\gamma,n})\bar{s} \\ \delta s_{\nu}(G_{\gamma,n+\nu}+G_{\gamma,n})\bar{s} & \delta s_{\nu}(G_{\gamma,n+\nu}+G_{\gamma,n})\bar{s} \end{pmatrix}, \tag{4.101}$$

$$\delta\mathcal{G}^{-1}_{2,n,\nu} = \begin{pmatrix} \delta s_{-\nu}(G_{\psi,n+\nu}+G_{\gamma,n+\nu})\delta s_{\nu} & \delta s_{-\nu}G_{\gamma,n+\nu}\delta s_{\nu} \\ \delta s_{-\nu}G_{\gamma,n+\nu}\delta s_{\nu} & \delta s_{-\nu}(\tilde{G}_{\psi,n+\nu}+G_{\gamma,n+\nu})\delta s_{\nu} \end{pmatrix}, \tag{4.102}$$

with

$$G_{f,n} = \frac{1}{i\omega_n - \epsilon - \eta - \bar{s}^2(G_{\psi,n}+G_{\gamma,n})}, \tag{4.103}$$

$$\tilde{G}_{f,n} = \frac{1}{i\omega_n + \epsilon + \eta - \bar{s}^2(\tilde{G}_{\psi,n}+G_{\gamma,n})}, \tag{4.104}$$

$$G_{\psi,n} = \tilde{G}_{\psi,n} = -i\Gamma\,\mathrm{sgn}(n), \quad G_{\gamma,n} = -\frac{i\lambda^2\omega_n}{\omega_n^2+\delta^2}. \tag{4.105}$$

After some manipulation, we get

$$S^{(2)}_{\text{eff}} = \frac{1}{2\beta}\sum_{\nu}(\dot{\theta}_{-\nu}\ \delta s_{-\nu}) \begin{pmatrix} \Gamma^{\dot{\theta}\dot{\theta}}_{\nu} & \Gamma^{\dot{\theta}s}_{\nu} \\ \Gamma^{\dot{\theta}s}_{\nu} & \Gamma^{ss}_{\nu} \end{pmatrix} \begin{pmatrix} \dot{\theta}_{\nu} \\ \delta s_{\nu} \end{pmatrix} \tag{4.106}$$

The full expressions of the above matrix elements Γ^{ij} are given in Appendix C.2. We first note that $\Gamma^{\dot{\theta}s}_{\nu} \approx 2i\bar{s}$ near the mean-field solution $\bar{\eta} \approx -\epsilon$. Diagonal element Γ^{ss}_{ν} and

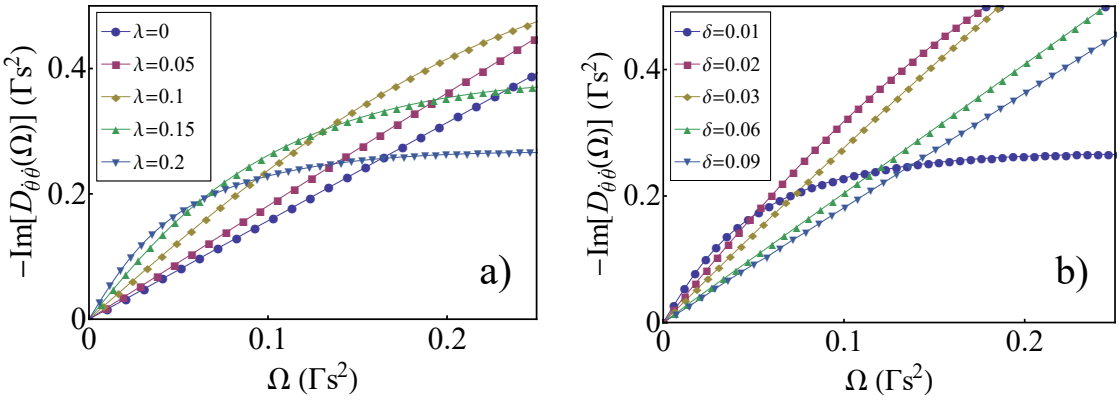

Figure 4.6: The function $\mathrm{Im}[D_{\dot\theta\dot\theta}(\Omega)]$ for different values of λ and δ. Here panels a) and b) correspond to $\delta = 0.01$ and $\lambda = 0.2$; we used $\Gamma = 1$, $\epsilon = -5$, $\Lambda = 50$ here.

$\Gamma^{\theta\theta}_\nu$ can be obtained using the analytic continuation of fermionic Matsubara frequency $i\omega_n \to \omega$ and integrating around the two branch cuts $\mathrm{Im}[\omega] = 0$ and $\mathrm{Im}[\omega] = -\omega_\nu$. The correlation function of δs and $\dot\theta$ is given by

$$D_{\dot\theta\dot\theta}(i\omega_\nu) = \frac{\Gamma^{ss}_\nu}{\Gamma^{\dot\theta\dot\theta}_\nu \Gamma^{ss}_\nu + 4\bar{s}^2}, \tag{4.107}$$

$$D_{ss}(i\omega_\nu) = \frac{\Gamma^{\dot\theta\dot\theta}_\nu}{\Gamma^{\dot\theta\dot\theta}_\nu \Gamma^{ss}_\nu + 4\bar{s}^2}, \tag{4.108}$$

and govern the dynamics of the fluctuating fields $\delta s(\tau)$ and $\dot\theta(\tau)$. We can now address the question regarding the restoration of the broken $\mathbb{U}(1)$ symmetry.

Let us consider the correlation function $\langle b(\tau) b^*(0)\rangle$. The mean-field solution assumes that $\langle b(\tau) b^*(0)\rangle \to \bar{s}^2$ for $\tau \to \infty$. It has been shown, however, in Ref. [77, 16] that the above correlation function for the generalized Anderson model decays as a power-law $\langle b(\tau) b^*(0)\rangle \propto |\tau|^{-\alpha}$ with some non-universal exponent. We now perform a similar analysis for QD-MKP problem at hand. Since $\langle s(\tau) s(0)\rangle \sim \bar{s}^2$ in the long time limit, one

can decouple amplitude and phase fluctuations

$$\begin{aligned}\langle b(\tau)b^*(0)\rangle &\approx \bar{s}^2\langle e^{i(\theta(\tau)-\theta(0))}\rangle \\ &= \bar{s}^2\exp(-\frac{1}{2}\langle[\theta(\tau)-\theta(0)]^2\rangle). \end{aligned} \tag{4.109}$$

We can evaluate the exponent, following Ref.[16], as

$$\frac{1}{2}\langle[\theta(\tau)-\theta(0)]^2\rangle = \frac{1}{\beta}\sum_{\nu\neq 0}\frac{D_{\dot{\theta}\dot{\theta}}}{\omega_\nu^2}(1-e^{-i\omega_\nu\tau}) \tag{4.110}$$

$$= -\oint\frac{d\Omega}{2\pi i}\frac{1-e^{-\Omega\tau}}{1-e^{-\beta\Omega}}\frac{D_{\dot{\theta}\dot{\theta}}(\Omega)}{\Omega^2} \tag{4.111}$$

$$\overset{T\to 0}{=} -\int_0^\infty\frac{d\Omega}{\pi}\frac{1-e^{-\Omega\tau}}{\Omega^2}\mathrm{Im}[\lim_{\xi\to 0^+}D_{\dot{\theta}\dot{\theta}}(\Omega+i\xi)]. \tag{4.112}$$

Here Matsubara sum was evaluated by integrating along the branch cut $\mathrm{Im}[\Omega]=0$ using the analytic continuation for bosonic Matsubara frequency $i\omega_\nu\to\Omega$. See Appendix C.2 for more detail. We find that $\mathrm{Im}[D_{\dot{\theta}\dot{\theta}}(\Omega+i\epsilon)]\propto -\alpha\Omega$ in low frequency limit, see Fig. 4.6. Here we eventually take $\epsilon\to 0$. Thus, the correlation function

$$\langle b(\tau)b^*(0)\rangle \propto \tau^{-\alpha} \tag{4.113}$$

decays as a power law in long-time limit, which is a key result of this section. In this sense, the situation is analogous to the slave-boson theory for the Kondo problem. The expression for α as a function of $\lambda_0=\lambda/\Gamma\bar{s}$ in the limit of zero splitting for MKP, $\delta\to 0$, is given by

$$\alpha = \frac{1}{2}\frac{1}{(f(\lambda_0)+\bar{s}^2\pi^2/4)} \tag{4.114}$$

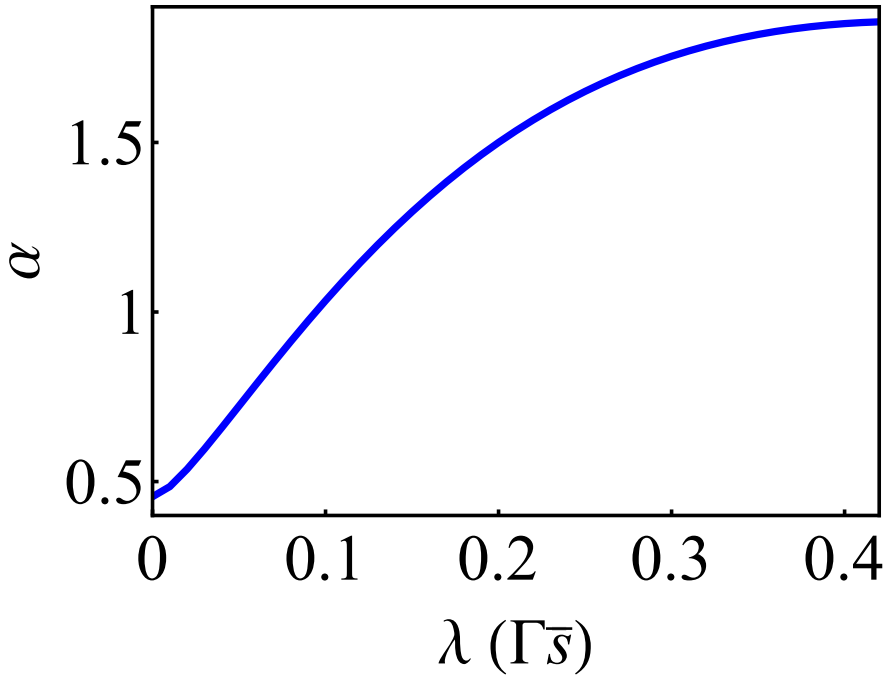

Figure 4.7: The exponent α as a function of Majorana coupling strength λ.

$$f(\lambda)=\begin{cases} -\frac{\ln[4\lambda^4]}{8\lambda^2}-\frac{1-4\lambda^2}{8\lambda^2\sqrt{1-8\lambda^2}}\ln\left[\frac{1-4\lambda^2+\sqrt{1-8\lambda^2}}{1-4\lambda^2-\sqrt{1-8\lambda^2}}\right], & \lambda<\frac{1}{2} \\ -\frac{\ln[4\lambda^4]}{8\lambda^2}-\frac{1-4\lambda^2}{4\lambda^2\sqrt{1-8\lambda^2}}\left(\frac{\pi}{2}-\tan^{-1}\frac{1-4\lambda^2}{\sqrt{1-8\lambda^2}}\right), & \lambda\geq\frac{1}{2} \end{cases} \tag{4.115}$$

Using the corresponding mean-field solution of Eq. (4.84), one can evaluate the exponent α, see Fig. 4.7. We find that the exponent α moderately increases with λ. When the Majorana splitting energy δ becomes larger, α decreases and eventually approaches the value in the Kondo limit $\alpha=\frac{1}{2}+O(\bar{s}^2)$.

Overall, we find that the correlation function (4.109) decays as a power law in the long-time limit which is qualitatively similar to phase fluctuations in the Kondo problem. This is the main result of this section showing that fluctuations ultimately restore $\mathbb{U}(1)$ symmetry, in agreement with the Mermin-Wagner theorem, but the correlation function decays slowly in comparison with the "disordered" high-temperature limit. The situation

is reminiscent of quasi-long range order where the fluctuations ultimately restore the broken symmetry but, at the same time, there is a well-defined mean-field amplitude of fluctuations (i.e. $\bar{s} \neq 0$) which opens up a gap in the spectrum.

4.3.4 Differential tunneling conductance

Using the mean-field theory developed in the previous sections, one can now calculate transport properties of the NL-QD-TSC junction. To compute the differential conductance G, one needs to compute scattering matrix of the system within the mean-field approximation. The slave-boson mean-field Hamiltonian can be written as

$$H_{sb} = H_{NL} + \sum_{\sigma} \left[\sum_{k} tb(f_{\sigma}^{\dagger}\psi_{k,\sigma} + \psi_{k,\sigma}^{\dagger} f_{\sigma}) + \tilde{\epsilon} f_{\sigma}^{\dagger} f_{\sigma} + i\lambda_{\sigma} b \gamma_{\sigma}^{1}(f_{\sigma}^{\dagger} + f_{\sigma}) + i\delta_{1\sigma}\gamma_{\sigma}^{1}\gamma_{\sigma}^{2} + i\delta_{2}\gamma_{\sigma}^{1}\gamma_{-\sigma}^{2} \right]. \tag{4.116}$$

The scattering matrix for electrons close to the Fermi level is given by

$$S(E) = 1 + 2\pi i \hat{W}^{\dagger}(H_{local} - E - \pi i \hat{W}\hat{W}^{\dagger})^{-1}\hat{W}, \tag{4.117}$$

where H_{local} is the Hamiltonian describing the "local impurity" and $\hat{W} \propto tb$ is the matrix of coupling constants between local degrees of freedom and lead electrons.

Using the scattering matrix one can compute the probability for Andreev reflection and ultimately obtain differential conductance $G(V)$. In agreement with the analysis in Sec. 4.3.2, we find that zero-bias differential conductance is quantized $G(0) = 4e^2/h$. In the limit of small bias voltage and zero splitting $\delta \to 0$, the differential conductance $G(V)$ reads

$$G(V) \approx \frac{4e^2}{h} \frac{\Gamma_{\text{eff}}^2}{\Gamma_{\text{eff}}^2 + (eV)^2} \tag{4.118}$$

with the width of the zero-bias peak changing from $\Gamma_{\text{eff}} = \min\{T_K, \frac{2\lambda^2}{\Gamma}\}$ in Kondo-

dominated to $\Gamma_{\text{eff}} = \frac{\Gamma\lambda^2}{2\epsilon^2}$ in the Majorana-dominted regime.

In addition to the differential conductance, the signatures of MKP should be observable in shot noise and full counting statistics measurements as have been discussed in the context of a quantum dot coupled to a single MZM, see, e.g., Refs. [51, 52].

4.4 Discussion

In this chapter we have studied two systems involving MKPs: LL-MKP and NL-QD-MKP junctions. At the level of single-particle Hamiltonian, the presence of MKP leads to a quantized zero bias differential conductance of $4e^2/h$ with perfect Andreev reflection. We extend the analysis to interacting systems.

For the case of LL-MKP junction, we consider repulsive electron-electron interactions in the wire. We find that perfect Andreev reflection fixed point is stable with respect to weak repulsive interactions in the lead. This result should be contrasted with the conventional LL-s-wave superconductor junction where weak repulsive interactions destabilize Andreev reflection fixed point and drive the system back to the normal reflection fixed point [26]. The reason for such a difference is that the IR fixed point boundary conditions of LL-MKP junction is similar to LL coupled to spin-triplet p-wave superconductor rather than spin-singlet s-wave superconductor.

Another interesting feature of the MKP is the possibility of having local four fermion interaction terms (i.e. terms proportional to Δ and Δ_{AN}) at the boundary. The existence of such operators leads to BKT phase transitions for moderate strength of the bulk electron-electron interaction ($1/3 > K_\rho > 1/4$). We have summarized the results in the phase diagram in Fig. 4.4.

Next we investigate effect of local interactions in the NL-QD-TRI topological superconductor junction. We show that the system flows to a new fixed point which is

characterized by a strong entanglement of a QD spin with a MKP. These correlations ultimately lead to the change of boundary conditions for lead electrons: from Kondo to perfect Andreev reflection boundary conditions. Using a combination of a perturbative RG analysis and slave-boson mean-field theory we identify the ground-state of the system and calculate tunneling conductance through the junction, demonstrating that zero-temperature differential tunneling conductance is $4e^2/h$. As we increase Majorana coupling λ, the width of the zero-bias peak exhibits a crossover from the Kondo temperature T_K to $\Gamma\lambda^2/\epsilon^2$ in the Majorana-dominated regime. We have also studied effect of Gaussian fluctuations around the mean-field saddle point and shown that the mean-field solution is well-defined (in the quasi-long range order sense) and thus can be used to calculate the spectrum in the QD as well as other observables.

Chapter 5

Future direction

As an extension of the studies in Chapter 2 and 3, it would be interesting to investigate the possibility of realizing Majorana zero modes in either nanowires or magnetic atom chains coupled to the FeSe monolayer superconducting film on top of $SrTiO_3$ substrate [76]. Since the FeSe monolayer deposited on STO has large superconducting gap, one could induce a large topological gap and stabilize the Majorana zero modes. In addition, the broken inversion symmetry at the surface could support significant amount of spin-orbit coupling which makes the system a nice platform to study the various effects of spin-orbit coupling on Yu-Shiba-Rusinov spectrums.

Another possible extension of the results of 3 is to take the lattice symmetry of the superconductor into account. In the recent demonstration of the Yu-Shiba-Rusinov states in two dimensional superconducting film [58], it has been shown that the wavefunction of such states are strongly affected by the lattices of the underlying superconductors. Therefore, understanding the effects of those lattices on the Yu-Shiba-Rusinov spectrum would be an important step toward the experimental realization of topological superconductivity in Yu-Shiba-Rusinov chains.

For future study on Majorana Kramers pairs, it would be interesting to study the

trasport phenomena in Josephson junctions made of two time-reversal invariant topological superconductors. In addition to the differential conductance that we have studied in Chapter 4, Josephson currents in such junctions can show unique signatures of Majorana Kramers pairs.

Appendix A

Calculation of Yu-Shiba-Rusinov spectrum for dimers and chains

A.1 Non-local Green's function

The momentum integral of Green's functions $\overline{\hat{G}^{ij}(E,\theta)}$ can be derived by splitting $\hat{G}(E,\mathbf{p})$ into two branches $\hat{G}^{\pm}(E,\mathbf{p})$ and changing the integral over the momentum to an integral over energy dispersion $\xi_{\pm}$ for each branch:

$$\overline{\hat{G}^{ij}(E,\theta)} = \frac{1}{2}(\overline{\hat{G}^{+,ij}(E,\theta)} + \overline{\hat{G}^{-,ij}(E,\theta)}) \tag{A.1}$$

$$\frac{1}{2}\overline{\hat{G}^{\lambda,ij}(E,\theta)} = \frac{1}{2}\int_0^{\infty}\frac{dp}{2\pi}\,pe^{-ix_{ij}p\cos\theta}\,\hat{G}^{\lambda}(E,\mathbf{p}) \tag{A.2}$$

$$\approx \frac{\nu_\lambda}{2}\int_{-\Lambda}^{\Lambda}d\xi_\lambda\,e^{-ix_{ij}p_\lambda(\xi_\lambda)\cos\theta}\hat{G}^{\lambda}(E,\xi_\lambda,\theta) \tag{A.3}$$

where $x_{ij} = x_i - x_j$, $\lambda = \pm$. One can rewrite the nth angular momentum component $\overline{\hat{G}_n^{ij}(E)}$ using the following integrals:

$$I_{n,\lambda}(x;E) = \frac{N_\lambda}{2\pi^2 N_F}\int_{-\pi}^{\pi} d\theta_{\mathbf{k}} \int_{-D}^{D} d\varepsilon \frac{e^{ik_\lambda(\varepsilon)x\cos\theta_{\mathbf{k}}} e^{in\theta_{\mathbf{k}}}\Delta}{E^2-\varepsilon^2-\Delta^2}, \tag{A.4}$$

$$K_{n,\lambda}(x;E) = \frac{N_\lambda}{2\pi^2 N_F}\int_{-\pi}^{\pi} d\theta_{\mathbf{k}} \int_{-D}^{D} d\varepsilon \frac{e^{ik_\lambda(\varepsilon)x\cos\theta_{\mathbf{k}}} e^{in\theta_{\mathbf{k}}}\varepsilon}{E^2-\varepsilon^2-\Delta^2}, \tag{A.5}$$

where D is an ultra-violet cut-off, $k_\lambda(\varepsilon) = k_{F,\lambda} + \varepsilon m\sqrt{1+\tilde{\alpha}^2}/k_F$ with $k_F = \sqrt{2m\mu}$, $k_{F,\lambda} = k_F\left(\sqrt{1+\tilde{\alpha}^2}+\lambda\tilde{\alpha}\right)$. $N_\lambda = \frac{m}{2\pi}\left[1+\lambda\frac{\tilde{\alpha}}{\sqrt{1+\tilde{\alpha}^2}}\right]$ is the density of states of the λ helical band at the Fermi level in the normal state, and $N_F = (N_+ + N_-)/2$. The analytic results for the above integrals in the limit $D\to\infty$ is given by

$$I_{0,\lambda}(x;E) = \frac{-\Delta\gamma_\lambda}{\sqrt{\Delta^2-E^2}}\mathrm{Re}\left[J_0\left((k_{F,\lambda}+i\zeta_\lambda^{-1})|x|\right) + iH_0\left((k_{F,\lambda}+i\zeta_\lambda^{-1})|x|\right)\right] \tag{A.6}$$

$$K_{0,\lambda}(x;E) = \gamma_\lambda\mathrm{Im}\left[J_0\left((k_{F,\lambda}+i\zeta_\lambda^{-1})|x|\right) + iH_0\left((k_{F,\lambda}+i\zeta_\lambda^{-1})|x|\right)\right] \tag{A.7}$$

$$I_{1,\lambda}(x;E) = -\mathrm{sgn}[x]\frac{i\Delta\gamma_\lambda}{\sqrt{\Delta^2-E^2}}\mathrm{Re}\left[J_1\left((k_{F,\lambda}+i\zeta_\lambda^{-1})|x|\right) - iH_{-1}\left((k_{F,\lambda}+i\zeta_\lambda^{-1})|x|\right)\right] \tag{A.8}$$

$$K_{1,\lambda}(x;E) = \mathrm{sgn}[x]i\gamma_\lambda\mathrm{Im}\left[J_1\left((k_{F,\lambda}+i\zeta_\lambda^{-1})|x|\right) - iH_{-1}\left((k_{F,\lambda}+i\zeta_\lambda^{-1})|x|\right)\right] \tag{A.9}$$

$$I_{2,\lambda}(x;E) = \frac{\Delta\gamma_\lambda}{\sqrt{\Delta^2-E^2}}\mathrm{Re}\left[J_2\left((k_{F,\lambda}+i\zeta_\lambda^{-1})|x|\right) + iH_{-2}\left((k_{F,\lambda}+i\zeta_\lambda^{-1})|x|\right) + \frac{2i}{\pi\left(k_{F,\lambda}+i\zeta_\lambda^{-1}\right)|x|}\right] \tag{A.10}$$

$$K_{2,\lambda}(x;E) = -\gamma_\lambda\mathrm{Im}\left[J_2\left((k_{F,\lambda}+i\zeta_\lambda^{-1})|x|\right) + iH_{-2}\left((k_{F,\lambda}+i\zeta_\lambda^{-1})|x|\right) + \frac{2i}{\pi\left(k_{F,\lambda}+i\zeta_\lambda^{-1}\right)|x|}\right] \tag{A.11}$$

$$I_{3,\lambda}(x;E) = \frac{i\mathrm{sgn}[x]\Delta\gamma_\lambda}{\sqrt{\Delta^2-E^2}}\mathrm{Re}\left[J_3\left((k_{F,\lambda}+i\zeta_\lambda^{-1})|x|\right) - iH_{-3}\left((k_{F,\lambda}+i\zeta_\lambda^{-1})|x|\right) + \frac{6i}{\pi\left[\left(k_{F,\lambda}+i\zeta_\lambda^{-1}\right)|x|\right]^2}\right] \tag{A.12}$$

$$K_{3,\lambda}(x;E) = -\mathrm{sgn}[x]i\gamma_\lambda\mathrm{Im}\left[J_3\left((k_{F,\lambda}+i\zeta_\lambda^{-1})|x|\right) - iH_{-3}\left((k_{F,\lambda}+i\zeta_\lambda^{-1})|x|\right) + \frac{6i}{\pi\left[\left(k_{F,\lambda}+i\zeta_\lambda^{-1}\right)|x|\right]^2}\right] \tag{A.13}$$

Here $J_n(z)$ and $H_n(z)$ are Bessel and Struve functions of order n, respectively; $\zeta_\lambda^{-1} \equiv \frac{\sqrt{\Delta^2-E^2}}{v_{F,\lambda}}$, and $\gamma_\lambda \equiv 1+\lambda\frac{\alpha}{\sqrt{1+\alpha^2}}$. Note that the expressions for $K_{l,\lambda}(x;E)$ given above are

valid for $x \neq 0$, and the integral $K_{l,\lambda}(0;E) = 0$ for $x = 0$. Assuming $k_F|x| \gg 1$ and $\zeta_\lambda^{-1} \approx \frac{\Delta}{v_{F,\lambda}} \ll k_{F,\lambda}$, we can use the asymptotic forms of the Bessel and Struve functions [1]. In the limit $k_F x \gg 1$, one can find approximate expressions up to the order $1/(k_F x)^2$:

$$I_{0,\lambda}(x;E) = \frac{-\Delta\gamma_\lambda}{\sqrt{\Delta^2 - E^2}}\sqrt{\frac{2}{\pi k_{F,\lambda}|x|}}e^{-\zeta_\lambda^{-1}|x|}\left[\cos(k_{F,\lambda}|x| - \frac{1}{4}\pi) + \frac{1}{8k_{F,\lambda}|x|}\sin(k_{F,\lambda}|x| - \frac{1}{4}\pi)\right] \quad \text{(A.14)}$$

$$K_{0,\lambda}(x;E) = \gamma_\lambda\sqrt{\frac{2}{\pi k_{F,\lambda}|x|}}e^{-\zeta_\lambda^{-1}|x|}\left[\sin(k_{F,\lambda}|x| - \frac{1}{4}\pi) - \frac{1}{8k_{F,\lambda}|x|}\cos(k_{F,\lambda}|x| - \frac{1}{4}\pi)\right] + \frac{2\gamma_\lambda}{\pi k_{F,\lambda}|x|} \quad \text{(A.15)}$$

$$I_{1,\lambda}(x;E) = -\frac{i\mathrm{sgn}[x]\Delta\gamma_\lambda}{\sqrt{\Delta^2 - E^2}}\sqrt{\frac{2}{\pi k_{F,\lambda}|x|}}e^{-\zeta_\lambda^{-1}|x|}\left[\cos(k_{F,\lambda}|x| - \frac{3}{4}\pi) - \frac{3}{8k_{F,\lambda}|x|}\sin(k_{F,\lambda}|x| - \frac{3}{4}\pi)\right] \quad \text{(A.16)}$$

$$K_{1,\lambda}(x;E) = \frac{i\gamma_\lambda x}{|x|}\sqrt{\frac{2}{\pi k_{F,\lambda}|x|}}e^{-\zeta_\lambda^{-1}|x|}\left[\sin(k_{F,\lambda}|x| - \frac{3}{4}\pi) + \frac{3}{8k_{F,\lambda}|x|}\cos(k_{F,\lambda}|x| - \frac{3}{4}\pi)\right] + \frac{2i\mathrm{sgn}[x]\gamma_\lambda}{\pi\left(k_{F,\lambda}|x|\right)^2} \quad \text{(A.17)}$$

$$I_{2,\lambda}(x;E) = \frac{-\Delta\gamma_\lambda}{\sqrt{\Delta^2 - E^2}}\sqrt{\frac{2}{\pi k_{F,\lambda}|x|}}e^{-\zeta_\lambda^{-1}|x|}\left[\cos(k_{F,\lambda}|x| - \frac{1}{4}\pi) - \frac{15}{8k_{F,\lambda}|x|}\sin(k_{F,\lambda}|x| - \frac{1}{4}\pi)\right] \quad \text{(A.18)}$$

$$K_{2,\lambda}(x;E) = \gamma_\lambda\sqrt{\frac{2}{\pi k_{F,\lambda}|x|}}e^{-\zeta_\lambda^{-1}|x|}\left[\sin(k_{F,\lambda}|x| - \frac{1}{4}\pi) + \frac{15}{8k_{F,\lambda}|x|}\cos(k_{F,\lambda}|x| - \frac{1}{4}\pi)\right] - \frac{2\gamma_\lambda}{\pi k_{F,\lambda}|x|} \quad \text{(A.19)}$$

$$I_{3,\lambda}(x;E) = -\frac{i\mathrm{sgn}[x]\Delta\gamma_\lambda}{\sqrt{\Delta^2 - E^2}}\sqrt{\frac{2}{\pi k_{F,\lambda}|x|}}e^{-\zeta_\lambda^{-1}|x|}\left[\cos(k_{F,\lambda}|x| - \frac{3}{4}\pi) - \frac{35}{8k_{F,\lambda}|x|}\sin(k_{F,\lambda}|x| - \frac{3}{4}\pi)\right] \quad \text{(A.20)}$$

$$K_{3,\lambda}(x;E) = \frac{i\gamma_\lambda x}{|x|}\sqrt{\frac{2}{\pi k_{F,\lambda}|x|}}e^{-\zeta_\lambda^{-1}|x|}\left[\sin(k_{F,\lambda}|x| - \frac{3}{4}\pi) + \frac{35}{8k_{F,\lambda}|x|}\cos(k_{F,\lambda}|x| - \frac{3}{4}\pi)\right] - \frac{6i\mathrm{sgn}[x]\gamma_\lambda}{\pi\left(k_{F,\lambda}|x|\right)^2} \quad \text{(A.21)}$$

The corresponding Fourier transforms of the above asymptotic forms to the leading order of $\frac{1}{\sqrt{k_F a}}$ are given by

$$\begin{aligned} I_{0,\lambda}(k;E) &= I_{2,\lambda}(k;E) \\ &= \frac{-\Delta\gamma_\lambda}{\sqrt{\Delta^2-E^2}}\sqrt{\frac{1}{2\pi k_{F,\lambda}a}}\Bigg[e^{-i\frac{1}{4}\pi}\mathrm{Li}_{\frac{1}{2}}\left(e^{ik_{F,\lambda}a-\zeta_\lambda^{-1}a+ika}\right)+e^{i\frac{1}{4}\pi}\mathrm{Li}_{\frac{1}{2}}\left(e^{-ik_{F,\lambda}a-\zeta_\lambda^{-1}a+ika}\right) \\ &+e^{-i\frac{1}{4}\pi}\mathrm{Li}_{\frac{1}{2}}\left(e^{ik_{F,\lambda}a-\zeta_\lambda^{-1}a-ika}\right)+e^{i\frac{1}{4}\pi}\mathrm{Li}_{\frac{1}{2}}\left(e^{-ik_{F,\lambda}a-\zeta_\lambda^{-1}a-ika}\right)\Bigg] \end{aligned} \tag{A.22}$$

$$\begin{aligned} K_{0,\lambda}(k;E) &= K_{2,\lambda}(k;E) \\ &= -i\gamma_\lambda\sqrt{\frac{1}{2\pi k_{F,\lambda}a}}\Bigg[e^{-i\frac{1}{4}\pi}\mathrm{Li}_{\frac{1}{2}}\left(e^{ik_{F,\lambda}a-\zeta_\lambda^{-1}a+ika}\right)-e^{i\frac{1}{4}\pi}\mathrm{Li}_{\frac{1}{2}}\left(e^{-ik_{F,\lambda}a-\zeta_\lambda^{-1}a+ika}\right) \\ &+e^{-i\frac{1}{4}\pi}\mathrm{Li}_{\frac{1}{2}}\left(e^{ik_{F,\lambda}a-\zeta_\lambda^{-1}a-ika}\right)-e^{i\frac{1}{4}\pi}\mathrm{Li}_{\frac{1}{2}}\left(e^{-ik_{F,\lambda}a-\zeta_\lambda^{-1}a-ika}\right)\Bigg] \end{aligned} \tag{A.23}$$

$$\begin{aligned} I_{1,\lambda}(k;E) &= I_{3,\lambda}(k;E) \\ &= -\frac{i\Delta\gamma_\lambda}{\sqrt{\Delta^2-E^2}}\sqrt{\frac{1}{2\pi k_{F,\lambda}a}}\Bigg[e^{-i\frac{3}{4}\pi}\mathrm{Li}_{\frac{1}{2}}\left(e^{ik_{F,\lambda}a-\zeta_\lambda^{-1}a+ika}\right)+e^{i\frac{3}{4}\pi}\mathrm{Li}_{\frac{1}{2}}\left(e^{-ik_{F,\lambda}a-\zeta_\lambda^{-1}a+ika}\right) \\ &-e^{-i\frac{3}{4}\pi}\mathrm{Li}_{\frac{1}{2}}\left(e^{ik_{F,\lambda}a-\zeta_\lambda^{-1}a-ika}\right)-e^{i\frac{3}{4}\pi}\mathrm{Li}_{\frac{1}{2}}\left(e^{-ik_{F,\lambda}a-\zeta_\lambda^{-1}a-ika}\right)\Bigg] \end{aligned} \tag{A.24}$$

$$\begin{aligned} K_{1,\lambda}(k;E) &= K_{3,\lambda}(k;E) \\ &= \gamma_\lambda\sqrt{\frac{1}{2\pi k_{F,\lambda}a}}\Bigg[e^{-i\frac{3}{4}\pi}\mathrm{Li}_{\frac{1}{2}}\left(e^{ik_{F,\lambda}a-\zeta_\lambda^{-1}a+ika}\right)-e^{i\frac{3}{4}\pi}\mathrm{Li}_{\frac{1}{2}}\left(e^{-ik_{F,\lambda}a-\zeta_\lambda^{-1}a+ika}\right) \\ &-e^{-i\frac{3}{4}\pi}\mathrm{Li}_{\frac{1}{2}}\left(e^{ik_{F,\lambda}a-\zeta_\lambda^{-1}a-ika}\right)+e^{i\frac{3}{4}\pi}\mathrm{Li}_{\frac{1}{2}}\left(e^{-ik_{F,\lambda}a-\zeta_\lambda^{-1}a-ika}\right)\Bigg] \end{aligned} \tag{A.25}$$

where $\mathrm{Li}_s(z)$ is the polylogarithm function

$$\mathrm{Li}_s(z)=\sum_{n=1}^{\infty}\frac{z^n}{n^s}.$$

Finally, expression for $\overline{\hat{G}_n^{ij}(E)}$ can be written as For $i \neq j$,

$$\begin{aligned}\overline{\hat{G}_n^{ij}(E)} = \frac{\pi N_F}{2}\sum_{\lambda=\pm}\Bigg\{ & (-i\lambda)\left[\left(\frac{E}{\Delta}\sigma_+\tau_0+\sigma_+\tau_x\right) I_{|-1+m|,\lambda} + (\sigma_+\tau_z)\, K_{|-1+m|,\lambda}\right] \\ & + \left[\left(\frac{E}{\Delta}\sigma_0\tau_0+\sigma_0\tau_x\right) I_{|m|,\lambda} + (\sigma_0\tau_z)\, K_{|m|,\lambda}\right] \\ & + (i\lambda)\left[\left(\frac{E}{\Delta}\sigma_-\tau_0+\sigma_-\tau_x\right) I_{|1+m|,\lambda} + (\sigma_-\tau_z)\, K_{|1+m|,\lambda}\right]\Bigg\} \end{aligned} \tag{A.26}$$

with $x_i - x_j$ for the argument of function Is and Ks.

A.2 Equation of YSR spectrum for a dimer

For dimer Eq. (3.11) of the main article becomes

$$\begin{pmatrix} \overline{\hat{G}_0(E)}\hat{V}_1^{-1}-1 & \overline{\hat{G}_{-1}(E)}\hat{V}_1^{0} & 0 & \overline{\hat{G}_0^{12}(E)}\hat{V}_2^{-1} & \overline{\hat{G}_{-1}^{12}(E)}\hat{V}_2^{0} & \overline{\hat{G}_{-2}^{12}(E)}\hat{V}_2^{1} \\ \overline{\hat{G}_1(E)}\hat{V}_1^{-1} & \overline{\hat{G}_0(E)}\hat{V}_1^{0}-1 & \overline{\hat{G}_{-1}(E)}\hat{V}_1^{1} & \overline{\hat{G}_1^{12}(E)}\hat{V}_2^{-1} & \overline{\hat{G}_0^{12}(E)}\hat{V}_2^{0} & \overline{\hat{G}_{-1}^{12}(E)}\hat{V}_2^{1} \\ 0 & \overline{\hat{G}_1(E)}\hat{V}_1^{0} & \overline{\hat{G}_0(E)}\hat{V}_1^{1}-1 & \overline{\hat{G}_2^{12}(E)}\hat{V}_2^{-1} & \overline{\hat{G}_1^{12}(E)}\hat{V}_2^{0} & \overline{\hat{G}_0^{12}(E)}\hat{V}_2^{1} \end{pmatrix} \begin{pmatrix} \overline{\psi_{1,-1}} \\ \overline{\psi_{1,0}} \\ \overline{\psi_{1,1}} \\ \overline{\psi_{2,-1}} \\ \overline{\psi_{2,0}} \\ \overline{\psi_{2,1}} \end{pmatrix} = 0, \tag{A.27}$$

$$\begin{pmatrix} \overline{\hat{G}_0^{21}(E)}\hat{V}_1^{-1} & \overline{\hat{G}_{-1}^{21}(E)}\hat{V}_1^{0} & \overline{\hat{G}_{-2}^{21}(E)}\hat{V}_1^{1} & \overline{\hat{G}_0(E)}\hat{V}_2^{-1}-1 & \overline{\hat{G}_{-1}(E)}\hat{V}_2^{0} & 0 \\ \overline{\hat{G}_1^{21}(E)}\hat{V}_1^{-1} & \overline{\hat{G}_0^{21}(E)}\hat{V}_1^{0} & \overline{\hat{G}_{-1}^{21}(E)}\hat{V}_1^{1} & \overline{\hat{G}_1(E)}\hat{V}_2^{-1} & \overline{\hat{G}_0(E)}\hat{V}_2^{0}-1 & \overline{\hat{G}_{-1}(E)}\hat{V}_2^{1} \\ \overline{\hat{G}_2^{21}(E)}\hat{V}_1^{-1} & \overline{\hat{G}_1^{21}(E)}\hat{V}_1^{0} & \overline{\hat{G}_0^{21}(E)}\hat{V}_1^{1} & 0 & \overline{\hat{G}_1(E)}\hat{V}_2^{0} & \overline{\hat{G}_0(E)}\hat{V}_2^{1}-1 \end{pmatrix} \begin{pmatrix} \overline{\psi_{1,-1}} \\ \overline{\psi_{1,0}} \\ \overline{\psi_{1,1}} \\ \overline{\psi_{2,-1}} \\ \overline{\psi_{2,0}} \\ \overline{\psi_{2,1}} \end{pmatrix} = 0. \tag{A.28}$$

Again bound-state energy is the solution of

$$\det\begin{bmatrix} \overline{\hat{G}_0(E)}\hat{V}_1^{-1}-1 & \overline{\hat{G}_{-1}(E)}\hat{V}_1^0 & 0 & \overline{\hat{G}_0^{12}(E)}\hat{V}_2^{-1} & \overline{\hat{G}_{-1}^{12}(E)}\hat{V}_2^0 & \overline{\hat{G}_{-2}^{12}(E)}\hat{V}_2^1 \\ \overline{\hat{G}_1(E)}\hat{V}_1^{-1} & \overline{\hat{G}_0(E)}\hat{V}_1^0-1 & \overline{\hat{G}_{-1}(E)}\hat{V}_1^1 & \overline{\hat{G}_1^{12}(E)}\hat{V}_2^{-1} & \overline{\hat{G}_0^{12}(E)}\hat{V}_2^0 & \overline{\hat{G}_{-1}^{12}(E)}\hat{V}_2^1 \\ 0 & \overline{\hat{G}_1(E)}\hat{V}_1^0 & \overline{\hat{G}_0(E)}\hat{V}_1^1-1 & \overline{\hat{G}_2^{12}(E)}\hat{V}_2^{-1} & \overline{\hat{G}_1^{12}(E)}\hat{V}_2^0 & \overline{\hat{G}_0^{12}(E)}\hat{V}_2^1 \\ \overline{\hat{G}_0^{21}(E)}\hat{V}_1^{-1} & \overline{\hat{G}_{-1}^{21}(E)}\hat{V}_1^0 & \overline{\hat{G}_{-2}^{21}(E)}\hat{V}_1^1 & \overline{\hat{G}_0(E)}\hat{V}_2^{-1}-1 & \overline{\hat{G}_{-1}(E)}\hat{V}_2^0 & 0 \\ \overline{\hat{G}_1^{21}(E)}\hat{V}_1^{-1} & \overline{\hat{G}_0^{21}(E)}\hat{V}_1^0 & \overline{\hat{G}_{-1}^{21}(E)}\hat{V}_1^1 & \overline{\hat{G}_1(E)}\hat{V}_2^{-1} & \overline{\hat{G}_0(E)}\hat{V}_2^0-1 & \overline{\hat{G}_{-1}(E)}\hat{V}_2^1 \\ \overline{\hat{G}_2^{21}(E)}\hat{V}_1^{-1} & \overline{\hat{G}_1^{21}(E)}\hat{V}_1^0 & \overline{\hat{G}_0^{21}(E)}\hat{V}_1^1 & 0 & \overline{\hat{G}_1(E)}\hat{V}_2^0 & \overline{\hat{G}_0(E)}\hat{V}_2^1-1 \end{bmatrix} = 0. \tag{A.29}$$

Due to the inter-site terms the spectrum now depends on the distance between two impurity as well as their magnetic and scalar potentials.

A.3 Derivation of effective Hamiltonian

In this section, we provide the details of the derivation of effective Hamiltonian in deep s-band and depp $p-$band limits.

In the deep s-band limit, equation for $l = 0$ band reads

$$\sum_{j,l} \mathbf{M}_{0,l}^{ij}(E)\overline{\psi}_{j,l} = 0. \tag{A.30}$$

After substituting Eq. (3.26) back into the above equation, we get

$$\begin{aligned} 0 =&(\mathbf{M}_{0,0}^{ii} - \mathbf{M}_{0,-1}^{ii}(\mathbf{M}_{-1,-1}^{ii})^{-1}\mathbf{M}_{-1,0}^{ii} - \mathbf{M}_{0,1}^{ii}(\mathbf{M}_{1,1}^{ii})^{-1}\mathbf{M}_{1,0}^{ii})\overline{\psi}_{i,0} \\ &+ \sum_{j\neq i}(\mathbf{M}_{0,-1}^{ij}\overline{\psi}_{j,-1} + \mathbf{M}_{0,0}^{ij}\overline{\psi}_{j,0} + \mathbf{M}_{0,1}^{ij}\overline{\psi}_{j,1}) \\ &+ \mathbf{M}_{0,-1}^{ii}(\mathbf{M}_{-1,-1}^{ii})^{-1}\sum_{j\neq i}(\mathbf{M}_{-1,-1}^{ij}\overline{\psi}_{j,-1} + \mathbf{M}_{-1,0}^{ij}\overline{\psi}_{j,0} + \mathbf{M}_{-1,1}^{ij}\overline{\psi}_{j,1}) \\ &+ \mathbf{M}_{0,1}^{ii}(\mathbf{M}_{1,1}^{ii})^{-1}\sum_{j\neq i}(\mathbf{M}_{1,-1}^{ij}\overline{\psi}_{j,-1} + \mathbf{M}_{1,0}^{ij}\overline{\psi}_{j,0} + \mathbf{M}_{1,1}^{ij}\overline{\psi}_{j,1}). \end{aligned} \tag{A.31}$$

The assumption $k_F a \gg 1$ allows one to neglect the terms $\mathcal{O}((\mathbf{M}^{i\neq j})^2)$. Using the tight-binding approximation, one finally arrives at

$$\begin{aligned}
0 =& \Big[\mathbf{M}^{ii}_{0,0} - \mathbf{M}^{ii}_{0,-1}(\mathbf{M}^{ii}_{-1,-1})^{-1}\mathbf{M}^{ii}_{-1,0} - \mathbf{M}^{ii}_{0,1}(\mathbf{M}^{ii}_{1,1})^{-1}\mathbf{M}^{ii}_{1,0}\Big]\overline{\psi}_{i,0} \\
&- \sum_{j\neq i}\Big[\mathbf{M}^{ij}_{0,0} - \mathbf{M}^{ij}_{0,-1}(\mathbf{M}^{ii}_{-1,-1})^{-1}\mathbf{M}^{ii}_{-1,0} - \mathbf{M}^{ij}_{0,1}(\mathbf{M}^{ii}_{1,1})^{-1}\mathbf{M}^{ii}_{1,0} - \mathbf{M}^{ii}_{0,-1}(\mathbf{M}^{ii}_{-1,-1})^{-1}\mathbf{M}^{ij}_{-1,0} \\
&\quad - \mathbf{M}^{ii}_{0,1}(\mathbf{M}^{ii}_{1,1})^{-1}\mathbf{M}^{ij}_{1,0}\Big]\overline{\psi}_{j,0} \\
&- \sum_{j\neq i}\Big[\mathbf{M}^{ii}_{0,-1}(\mathbf{M}^{ii}_{-1,-1})^{-1}\mathbf{M}^{ij}_{-1,-1}(\mathbf{M}^{ii}_{-1,-1})^{-1}\mathbf{M}^{ii}_{-1,0} + \mathbf{M}^{ii}_{0,-1}(\mathbf{M}^{ii}_{-1,-1})^{-1}\mathbf{M}^{ij}_{-1,1}(\mathbf{M}^{ii}_{1,1})^{-1}\mathbf{M}^{ii}_{1,0} \\
&+ \mathbf{M}^{ii}_{0,1}(\mathbf{M}^{ii}_{1,1})^{-1}\mathbf{M}^{ij}_{1,-1}(\mathbf{M}^{ii}_{-1,-1})^{-1}\mathbf{M}^{ii}_{-1,0} + \mathbf{M}^{ii}_{0,1}(\mathbf{M}^{ii}_{1,1})^{-1}\mathbf{M}^{ij}_{1,1}(\mathbf{M}^{ii}_{1,1})^{-1}\mathbf{M}^{ii}_{1,0}\Big]\overline{\psi}_{j,0} + \mathcal{O}((\mathbf{M}^{ij})^2) \\
\equiv& \sum_j \mathbf{M}^{ij}_s(E)\overline{\psi}_{j,0}
\end{aligned} \tag{A.32}$$

In the deep p-band limit, the equations for p-wave bands are given by

$$\sum_{j,l}\mathbf{M}^{ij}_{-1,l}(E)\overline{\psi}_{j,l} = 0 \tag{A.33}$$

$$\sum_{j,l}\mathbf{M}^{ij}_{1,l}(E)\overline{\psi}_{j,l} = 0 \tag{A.34}$$

In order to integrate out s-channel, we have to solve for $\overline{\psi}_{i,0}$ finding that

$$\overline{\psi}_{i,0} = -(\mathbf{M}^{ii}_{1,0})^{-1}(\mathbf{M}^{ii}_{0,-1}\overline{\psi}_{i,-1} + \mathbf{M}^{ii}_{0,1}\overline{\psi}_{i,1} + \sum_{j\neq i,l}\mathbf{M}^{ij}_{0,l}\overline{\psi}_{j,l}). \tag{A.35}$$

Substituting Eq. (A.35) into Eq. (A.33, A.34) and following the same procedure as in

$s-$band limit, we eventually obtain two coupled equations for the p-wave bands

$$\begin{aligned}
0 =&(\mathbf{M}^{ii}_{-1,-1} - \mathbf{M}^{ii}_{-1,0}(\mathbf{M}^{ii}_{0,0})^{-1}\mathbf{M}^{ii}_{0,-1})\overline{\psi}_{i,-1} - \mathbf{M}^{ii}_{-1,0}(\mathbf{M}^{ii}_{0,0})^{-1}\mathbf{M}^{ii}_{0,1}\overline{\psi}_{i,1} \\
&- \sum_{j\neq i}\Big[\mathbf{M}^{ij}_{-1,-1} - \mathbf{M}^{ij}_{-1,0}(\mathbf{M}^{ii}_{0,0})^{-1}\mathbf{M}^{ii}_{0,-1} - \mathbf{M}^{ii}_{-1,0}(\mathbf{M}^{ii}_{0,0})^{-1}\mathbf{M}^{ij}_{0,-1} \\
&\quad + \mathbf{M}^{ii}_{-1,0}(\mathbf{M}^{ii}_{0,0})^{-1}\mathbf{M}^{ij}_{0,0}(\mathbf{M}^{ii}_{0,0})^{-1}\mathbf{M}^{ii}_{0,-1}\Big]\overline{\psi}_{j,-1} - \sum_{j\neq i}\Big[\mathbf{M}^{ij}_{-1,1} - \mathbf{M}^{ij}_{-1,0}(\mathbf{M}^{ii}_{0,0})^{-1}\mathbf{M}^{ii}_{0,1} \\
&\quad - \mathbf{M}^{ii}_{-1,0}(\mathbf{M}^{ii}_{0,0})^{-1}\mathbf{M}^{ij}_{0,1} + \mathbf{M}^{ii}_{-1,0}(\mathbf{M}^{ii}_{0,0})^{-1}\mathbf{M}^{ij}_{0,0}(\mathbf{M}^{ii}_{0,0})^{-1}\mathbf{M}^{ii}_{0,1})\Big]\overline{\psi}_{j,1} \qquad \text{(A.36)} \\
0 =&-\mathbf{M}^{ii}_{1,0}(\mathbf{M}^{ii}_{0,0})^{-1}\mathbf{M}^{ii}_{0,-1}\overline{\psi}_{i,-1} + (\mathbf{M}^{ii}_{1,1} - \mathbf{M}^{ii}_{1,0}(\mathbf{M}^{ii}_{0,0})^{-1}\mathbf{M}^{ii}_{0,1})\overline{\psi}_{i,1} \\
&- \sum_{j\neq i}\Big[\mathbf{M}^{ij}_{1,-1} - \mathbf{M}^{ij}_{1,0}(\mathbf{M}^{ii}_{0,0})^{-1}\mathbf{M}^{ii}_{0,-1} - \mathbf{M}^{ii}_{1,0}(\mathbf{M}^{ii}_{0,0})^{-1}\mathbf{M}^{ij}_{0,-1} \\
&\quad + \mathbf{M}^{ii}_{1,0}(\mathbf{M}^{ii}_{0,0})^{-1}\mathbf{M}^{ij}_{0,0}(\mathbf{M}^{ii}_{0,0})^{-1}\mathbf{M}^{ii}_{0,-1})\Big]\overline{\psi}_{j,-1} - \sum_{j\neq i}\Big[\mathbf{M}^{ij}_{1,1} - \mathbf{M}^{ij}_{1,0}(\mathbf{M}^{ii}_{0,0})^{-1}\mathbf{M}^{ii}_{0,1} \\
&\quad - \mathbf{M}^{ii}_{1,0}(\mathbf{M}^{ii}_{0,0})^{-1}\mathbf{M}^{ij}_{0,1} + \mathbf{M}^{ii}_{1,0}(\mathbf{M}^{ii}_{0,0})^{-1}\mathbf{M}^{ij}_{0,0}(\mathbf{M}^{ii}_{0,0})^{-1}\mathbf{M}^{ii}_{0,1}\Big]\overline{\psi}_{j,1} \qquad \text{(A.37)}
\end{aligned}$$

After some manipulations, one can write eigenvalue equations in the compact form, see Eq. (3.44).

A.4 Effective Hamiltonian in the long wavelength limit

It is instructive to expand the functions $I(n,k)$ and $K(n,k)$ appearing in our effective Hamiltonian close to $k=0$ in order to understand the spectrum qualitatively. After some

algebra, one finds

$$
\begin{aligned}
I_{0,\lambda}(k;E=0) &= I_{2,\lambda}(k;E=0) && \text{(A.38)}\\
&= -2\gamma_\lambda\sqrt{\frac{1}{\pi k_{F,\lambda}a}}\left[A_0(k_{F,\lambda}a+i\zeta_\lambda^{-1}a)+A_2(k_{F,\lambda}a+i\zeta_\lambda^{-1}a)k^2\right]+\mathcal{O}(k^4),\\
I_{1,\lambda}(k;E=0) &= I_{3,\lambda}(k;E=0)\\
&= -2\gamma_\lambda\sqrt{\frac{1}{\pi k_{F,\lambda}a}}B_1(k_{F,\lambda}a+i\zeta_\lambda^{-1}a)k+\mathcal{O}(k^3), && \text{(A.39)}\\
K_{1,\lambda}(k;E=0) &= K_{3,\lambda}(k;E=0)\\
&= 2\gamma_\lambda\sqrt{\frac{1}{\pi k_{F,\lambda}a}}C_1(k_{F,\lambda}a+i\zeta_\lambda^{-1}a)k+\mathcal{O}(k^3), && \text{(A.40)}
\end{aligned}
$$

where

$$
\begin{aligned}
A_0(z) &= \mathrm{Re}\left[\mathrm{Li}_{\frac{1}{2}}\left(e^{iz}\right)\right]+\mathrm{Im}\left[\mathrm{Li}_{\frac{1}{2}}\left(e^{iz}\right)\right], && \text{(A.41)}\\
A_2(z) &= \mathrm{Im}\left[\mathrm{Li}_{-\frac{3}{2}}\left(e^{iz}\right)\right], && \text{(A.42)}\\
B_1(z) &= \mathrm{Re}\left[\mathrm{Li}_{-\frac{1}{2}}\left(e^{iz}\right)\right]-\mathrm{Im}\left[\mathrm{Li}_{-\frac{1}{2}}\left(e^{iz}\right)\right], && \text{(A.43)}\\
C_1(z) &= \mathrm{Re}\left[\mathrm{Li}_{-\frac{1}{2}}\left(e^{iz}\right)\right]+\mathrm{Im}\left[\mathrm{Li}_{-\frac{1}{2}}\left(e^{iz}\right)\right]. && \text{(A.44)}
\end{aligned}
$$

The dependence of the functions $A_0(z)$, $A_2(z)$, $B_1(z)$ and $C_1(z)$ on the external parameters is shown in Fig. A.1. One can notice that when $k_{F,\lambda}a = 2\pi n$ with n being an integer, these functions have singularities which follows from the definition of polylogarithm function. These singularities are cutoff by the finite coherence length. In realistic systems, however, the superconducting coherence length is much larger than the interatomic spacing, and, thus, the parameters such as effective mass and Fermi velocity are strongly dependent on $k_F a$, see Fig. A.1.

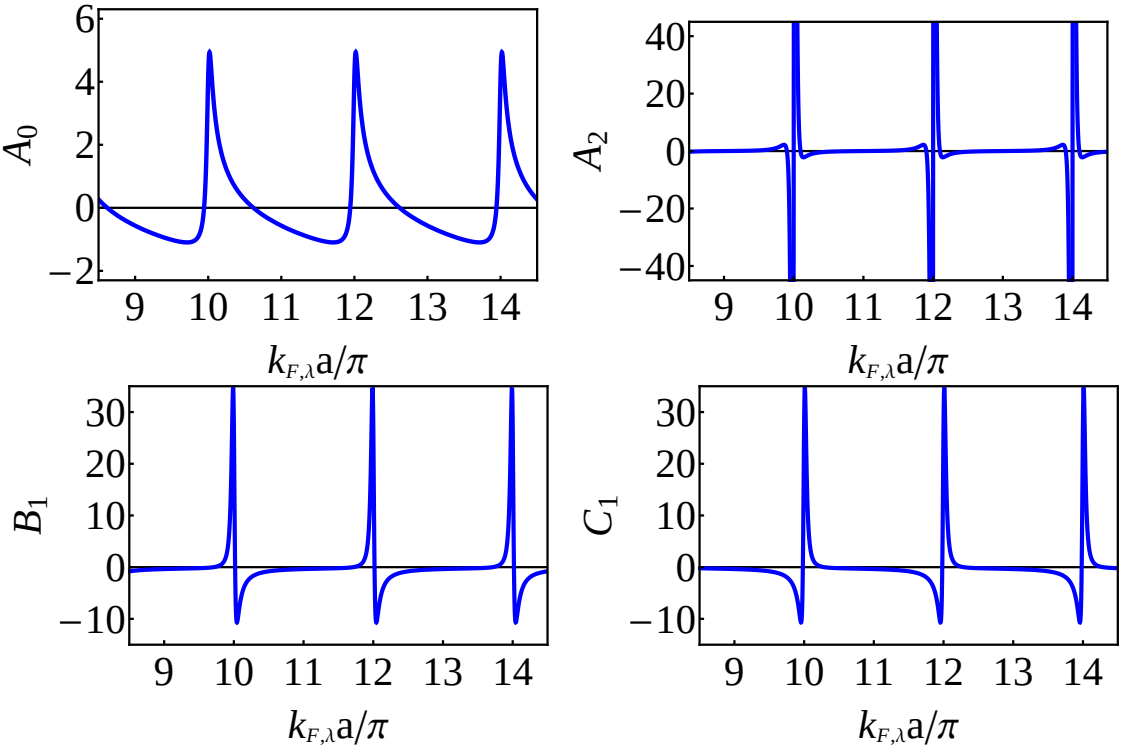

Figure A.1: The dependence of the functions A_0, A_2, B_1 and C_1 on $k_{F,\lambda}a$. Here we used $\zeta_\lambda = 10a$.

Finally, the expansion of the coefficients in the deep s-band Hamiltonian at $k \to 0$ becomes

$$h_z^{(0)} = \epsilon_z - \sum_\lambda \gamma_\lambda \sqrt{\frac{1}{\pi k_{F,\lambda} a}} \left(1 + \frac{2\alpha J_1(\alpha - \lambda)}{1 + J_1}\right) A_0(k_{F,\lambda} a + i\zeta_\lambda^{-1} a), \quad \text{(A.45)}$$

$$h_z^{(2)} = -\sum_\lambda \gamma_\lambda \sqrt{\frac{1}{\pi k_{F,\lambda} a}} \left(1 + \frac{2\alpha J_1(\alpha - \lambda)}{1 + J_1}\right) A_2(k_{F,\lambda} a + i\zeta_\lambda^{-1} a), \quad \text{(A.46)}$$

$$h_x^{(0)} = \epsilon_x - \sum_\lambda \gamma_\lambda \sqrt{\frac{1}{\pi k_{F,\lambda} a}} \left(1 - \frac{2\lambda\alpha J_1}{1 - J_1}\right) A_0(k_{F,\lambda} a + i\zeta_\lambda^{-1} a), \quad \text{(A.47)}$$

$$h_x^{(2)} = -\sum_\lambda \gamma_\lambda \sqrt{\frac{1}{\pi k_{F,\lambda} a}} \left(1 - \frac{2\lambda\alpha J_1}{1 - J_1}\right) A_2(k_{F,\lambda} a + i\zeta_\lambda^{-1} a), \quad \text{(A.48)}$$

$$h_y^{(0)} = \epsilon_x - \sum_\lambda \gamma_\lambda \sqrt{\frac{1}{\pi k_{F,\lambda} a}} \left(1 + \frac{2\lambda\alpha J_1}{1 - J_1}\right) A_0(k_{F,\lambda} a + i\zeta_\lambda^{-1} a), \quad \text{(A.49)}$$

$$h_y^{(2)} = -\sum_\lambda \gamma_\lambda \sqrt{\frac{1}{\pi k_{F,\lambda} a}} \left(1 + \frac{2\lambda\alpha J_1}{1 - J_1}\right) A_2(k_{F,\lambda} a + i\zeta_\lambda^{-1} a), \quad \text{(A.50)}$$

$$\Delta^{(1)} = \sum_\lambda i\gamma_\lambda \sqrt{\frac{1}{\pi k_{F,\lambda} a}} \left(\lambda - \frac{2\alpha J_1}{1 + J_1}\right) C_1(k_{F,\lambda} a + i\zeta_\lambda^{-1} a), \quad \text{(A.51)}$$

$$d_y^{(1)} = -\sum_\lambda \gamma_\lambda \sqrt{\frac{1}{\pi k_{F,\lambda} a}} \left(\lambda + \frac{2\alpha J_1}{1 - J_1}\right) B_1(k_{F,\lambda} a + i\zeta_\lambda^{-1} a). \quad \text{(A.52)}$$

The expansion coefficients in the deep p-band Hamiltonian are

$$h_{11}^{(0)} = \epsilon_1 - \sum_\lambda \gamma_\lambda \sqrt{\frac{1}{\pi k_{F,\lambda} a}} A_0(k_{F,\lambda} a + i\zeta_\lambda^{-1} a), \quad \text{(A.53)}$$

$$h_{22}^{(0)} = \epsilon_2 - \sum_\lambda \gamma_\lambda \sqrt{\frac{1}{\pi k_{F,\lambda} a}} A_0(k_{F,\lambda} a + i\zeta_\lambda^{-1} a), \quad \text{(A.54)}$$

$$h_{12}^{(0)} = = -\sum_\lambda \gamma_\lambda \sqrt{\frac{1}{\pi k_{F,\lambda} a}} A_0(k_{F,\lambda} a + i\zeta_\lambda^{-1} a), \quad \text{(A.55)}$$

$$h_{11}^{(2)} = h_{22}^{(2)} = h_{12}^{(2)} = -\sum_\lambda \gamma_\lambda \sqrt{\frac{1}{\pi k_{F,\lambda} a}} A_2(k_{F,\lambda} a + i\zeta_\lambda^{-1} a), \quad \text{(A.56)}$$

$$\Delta_{11}^{(1)} = \sum_{\lambda} i\gamma_{\lambda}\sqrt{\frac{1}{\pi k_{F,\lambda}a}}\left(\lambda - \frac{2\alpha J_0}{1+J_0}\right) C_1(k_{F,\lambda}a + i\zeta_{\lambda}^{-1}a), \tag{A.57}$$

$$\Delta_{22}^{(1)} = \sum_{\lambda} i\lambda\gamma_{\lambda}\sqrt{\frac{1}{\pi k_{F,\lambda}a}} C_1(k_{F,\lambda}a + i\zeta_{\lambda}^{-1}a), \tag{A.58}$$

$$\Delta_{12}^{(1)} = \sum_{\lambda} i\gamma_{\lambda}\sqrt{\frac{1}{\pi k_{F,\lambda}a}}\left(\lambda - \frac{\alpha J_0}{1+J_0}\right) C_{1,}(k_{F,\lambda}a + i\zeta_{\lambda}^{-1}a). \tag{A.59}$$

Appendix B

Second order perturbative RG analysis

B.1 Majorana Kramers pair - Luttinger liquid junction with $\mathbb{U}(1)$ symmetry

Here we provide details for the perturbative RG calculation for the MKP-LL junction with $\mathbb{U}(1)$ spin-rotation symmetry. We will use momentum shell RG procedure and calculate each term that is generated in the second order of perturbation theory.

In order to obtain the quadratic corrections to the RG flow Eq. (4.15) and Eq. (4.16) of the main text, let us consider the contribution from the $t_\uparrow t_\downarrow$ term:

$$\delta S^{(tt)} = -\frac{1}{2}\int d\tau \int d\tau' \frac{t_\uparrow t_\downarrow}{(2\pi a)^2}\gamma_\uparrow(\tau)\Gamma_\uparrow(\tau)\,\gamma_\downarrow(\tau')\Gamma_\downarrow(\tau') \tag{B.1}$$
$$\times\left(\left\langle \cos\frac{\theta_\rho(\tau)+\theta_\sigma(\tau)}{\sqrt{2}}\cos\frac{\theta_\rho(\tau')-\theta_\sigma(\tau')}{\sqrt{2}}\right\rangle_> - \left\langle \cos\frac{\theta_\rho(\tau)+\theta_\sigma(\tau)}{\sqrt{2}}\right\rangle_>\left\langle \cos\frac{\theta_\rho(\tau)-\theta_\sigma(\tau)}{\sqrt{2}}\right\rangle_>\right).$$

Here $\langle\ldots\rangle_>$ denotes integrating out the fast modes, $\Lambda/b < |\omega| < \Lambda$, where $b = e^l \approx 1 + dl$ describes the change in UV cutoff under RG procedure. One can evaluate above

correlation functions using the following identity:

$$\langle e^{\frac{i}{\sqrt{2}}\theta_j^>(\tau)}\rangle = e^{-\frac{1}{4}\langle\theta_j^>(\tau)^2\rangle}. \tag{B.2}$$

Taking into account that the correlation function $\langle(\theta_j^<(\tau)-\theta_j^<(\tau'))^2\rangle_<$ decays sufficiently quickly with $\tau-\tau'$, one can use the short distance expansion:

$$e^{i(\theta_j^<(\tau)-\theta_j^<(\tau'))} = (1+(\tau-\tau')\partial_\tau\theta_j+\ldots)e^{-\frac{1}{2}\langle(\theta_j^<(\tau)-\theta_j^<(\tau'))^2\rangle_<} \tag{B.3}$$

where the correlation functions are given by

$$\begin{aligned}\langle(\theta_j(\tau)-\theta_j(\tau'))^2\rangle &= \langle(\theta_j^<(\tau)-\theta_j^<(\tau'))^2\rangle_< + \langle(\theta_j^>(\tau)-\theta_j^>(\tau'))^2\rangle_> \\ &= \frac{2}{K_j}\ln\left[\frac{a}{v|\tau-\tau'|+a}\right] \qquad \text{(B.4)}\\ g_j(\tau-\tau') &\equiv \langle\theta_j^>(\tau)\theta_j^>(\tau')\rangle_> = \frac{1}{K_j}\int_{\Lambda/b}^{\Lambda}\frac{d\omega}{\omega}\cos(\omega|\tau-\tau'|). \qquad \text{(B.5)}\end{aligned}$$

Using the above, one finds that

$$\begin{aligned}&\left\langle\cos\frac{\theta_\rho(\tau)+\theta_\sigma(\tau)}{\sqrt{2}}\cos\frac{\theta_\rho(\tau')-\theta_\sigma(\tau')}{\sqrt{2}}\right\rangle_> \\ &= \frac{1}{2}\left(\frac{\cos\frac{\theta_\sigma^<(\tau)+\theta_\sigma^<(\tau')}{\sqrt{2}}}{(\Lambda|\tau-\tau'|+1)^{\frac{1}{2K_\rho}}}e^{-\frac{1}{2}(g_\sigma(0)+g_\sigma(\tau-\tau'))}+\frac{\cos\frac{\theta_\rho^<(\tau)+\theta_\rho^<(\tau')}{\sqrt{2}}}{(\Lambda|\tau-\tau'|+1)^{\frac{1}{2K_\sigma}}}e^{-\frac{1}{2}(g_\rho(0)+g_\rho(\tau-\tau'))}\right).\end{aligned} \tag{B.6}$$

The contribution of disconnected part is given by

$$\left\langle \cos\frac{\theta_\rho(\tau)+\theta_\sigma(\tau)}{\sqrt{2}} \right\rangle_> \left\langle \cos\frac{\theta_\rho(\tau)-\theta_\sigma(\tau)}{\sqrt{2}} \right\rangle_> \tag{B.7}$$

$$= \frac{1}{2}\left(\frac{\cos\frac{\theta_\sigma^<(\tau)+\theta_\sigma^<(\tau')}{\sqrt{2}}}{(\Lambda|\tau-\tau'|+1)^{\frac{1}{2K_\rho}}} e^{-\frac{1}{2}(g_\sigma(0)+g_\rho(\tau-\tau'))} + \frac{\cos\frac{\theta_\rho^<(\tau)+\theta_\rho^<(\tau')}{\sqrt{2}}}{(\Lambda|\tau-\tau'|+1)^{\frac{1}{2K_\sigma}}} e^{-\frac{1}{2}(g_\rho(0)+g_\sigma(\tau-\tau'))} \right). \tag{B.8}$$

Before we proceed, it is important to note that

$$g_j(\tau-\tau') \equiv \langle \theta_j^>(\tau)\theta_j^>(\tau')\rangle = \frac{1}{K_j}\int_{\Lambda/b}^{\Lambda}\frac{d\omega}{\omega}\cos[\omega(\tau-\tau')] \approx \frac{1}{K_j}\cos[\Lambda(\tau-\tau')]dl \tag{B.9}$$

for small dl, and thus $g_j(0) \approx dl/K_j$. Now we introduce new variables: center-of-mass $T = \frac{\tau+\tau'}{2}$ and relative coordinates $s = \tau - \tau'$. The correction to the action to the linear order of dl becomes

$$\begin{aligned}
\delta S^{(tt)} &= \frac{1}{4}\frac{t_\uparrow t_\downarrow}{(2\pi a)^2}\int_0^\infty dT\int_{-\infty}^\infty ds\gamma_\uparrow\gamma_\downarrow\Gamma_\uparrow\Gamma_\downarrow\cos\frac{\theta_\sigma(T+s/2)+\theta_\sigma(T-s/2)}{\sqrt{2}} \\
&\quad\times\left(\frac{1}{2K_\rho}-\frac{1}{2K_\sigma}\right)\left(\frac{\cos(\Lambda s)}{(\Lambda|s|+1)^{\frac{1}{2K_\rho}}}\right)dl \\
&\quad+\frac{1}{4}\frac{t_\uparrow t_\downarrow}{(2\pi a)^2}\int_0^\infty dT\int_{-\infty}^\infty ds\gamma_\uparrow\gamma_\downarrow\Gamma_\uparrow\Gamma_\downarrow\cos\frac{\theta_\rho(T+s/2)+\theta_\rho(T-s/2)}{\sqrt{2}} \\
&\quad\times\left(\frac{1}{2K_\sigma}-\frac{1}{2K_\rho}\right)\left(\frac{\cos(\Lambda s)}{(\Lambda|s|+1)^{\frac{1}{2K_\sigma}}}\right)dl
\end{aligned} \tag{B.10}$$

Since the above expression has a power law decay in $\Lambda|s|$, the contributions to the integral comes from the short time $|s| \sim 1/\Lambda$. After the simplification, the total contri-

bution to the effective action reads

$$\delta S^{(tt)} \approx \frac{1}{4}\frac{t_\uparrow t_\downarrow}{(2\pi a)^2}\frac{2dl}{\Lambda}\left(\frac{1}{2K_\rho}-\frac{1}{2K_\sigma}\right)C\left(\frac{1}{2K_\rho}\right)\int_0^\beta dT\gamma_\uparrow\gamma_\downarrow\Gamma_\uparrow\Gamma_\downarrow\cos\sqrt{2}\theta_\sigma(T)$$
$$+\frac{1}{4}\frac{t_\uparrow t_\downarrow}{(2\pi a)^2}\frac{2dl}{\Lambda}\left(\frac{1}{2K_\sigma}-\frac{1}{2K_\rho}\right)C\left(\frac{1}{2K_\sigma}\right)\int_0^\beta dT\gamma_\uparrow\gamma_\downarrow\Gamma_\uparrow\Gamma_\downarrow\cos\sqrt{2}\theta_\rho(T) \quad \text{(B.11)}$$

where the dimensionless function $C(\nu)$ is defined as

$$C(\nu)=\lim_{\delta\to 0^+}\int_0^\infty \frac{e^{-\delta x}\cos x}{(1+x)^\nu}dx. \quad \text{(B.12)}$$

Notice that $C(\nu)$ is proportional to ν when $\nu\to 0$. Away from $\nu=0$, $C(\nu)$ is simply $\mathcal{O}(1)$ constant which can be absorbed into the definition of the coupling constants.

Combining all the terms in Eq. (B.11), we find the following contributions to the RG equations at quadratic order in t:

$$\frac{d\Delta^{(2)}}{dl} = -\frac{t^2}{4\pi v}\left(\frac{1}{K_\rho}-\frac{1}{K_\sigma}\right) \quad \text{(B.13)}$$
$$\frac{d\Delta^{(2)}_{\mathrm{AN}}}{dl} = \frac{t^2}{4\pi v}\left(\frac{1}{K_\rho}-\frac{1}{K_\sigma}\right), \quad \text{(B.14)}$$

where $v=a\Lambda$. See Eq. (4.15) and Eq. (4.16) of the main text. Note that factor of 2 here originates from the switching time coordinates τ and τ'.

We now consider the contribution to RG equations from the crossed terms proportional to $t\Delta$, see Eq. (4.14) in the main text. The relevant terms in the second order expansion of S_T are

$$\delta S^{(t\Delta)} = -\frac{1}{2}\int d\tau\int\tau'\frac{-i\,t_\uparrow\Delta}{(2\pi a)^2}\gamma_\uparrow(\tau)\Gamma_\uparrow(\tau)\,\gamma_\uparrow(\tau')\gamma_\downarrow(\tau')\Gamma_\uparrow(\tau')\Gamma_\downarrow(\tau') \quad \text{(B.15)}$$
$$\times\left(\langle\cos\frac{\theta_\rho(\tau)+\theta_\sigma(\tau)}{\sqrt{2}}\cos\sqrt{2}\theta_\sigma(\tau')\rangle_> - \langle\cos\frac{\theta_\rho(\tau)+\theta_\sigma(\tau)}{\sqrt{2}}\rangle_>\langle\cos\sqrt{2}\theta_\sigma(\tau')\rangle_>\right).$$

Given that $\langle\gamma_s(\tau)\gamma_s(\tau')\rangle = \mathrm{sgn}(\tau-\tau')$ and $\langle\Gamma_s(\tau)\Gamma_s(\tau')\rangle = \mathrm{sgn}(\tau-\tau')$, Majoranas and Klein factors can be simplified as

$$\gamma_\uparrow(\tau)\Gamma_\uparrow(\tau)\,\gamma_\uparrow(\tau')\gamma_\downarrow(\tau')\Gamma_\uparrow(\tau')\Gamma_\downarrow(\tau') = \gamma_\downarrow(\tau')\Gamma_\downarrow(\tau'). \tag{B.16}$$

Next, we evaluate the bosonic part of the correlation function

$$\begin{aligned}\langle\cos\frac{\theta_\rho(\tau)+\theta_\sigma(\tau)}{\sqrt{2}}\cos\sqrt{2}\theta_\sigma(\tau')\rangle_> - \langle\cos\frac{\theta_\rho(\tau)+\theta_\sigma(\tau)}{\sqrt{2}}\rangle_>\langle\cos\sqrt{2}\theta_\sigma(\tau')\rangle_> \\ \approx \frac{1}{2K_\sigma}\cos\frac{\theta^<_\rho(T)-\theta^<_\sigma(T)}{\sqrt{2}}\frac{\cos(\Lambda s)dl}{(\Lambda|s|+1)^{\frac{1}{2K_\sigma}}}.\end{aligned} \tag{B.17}$$

Here we dropped irrelevant terms generated by the RG procedure such as $\cos\frac{\theta^<_\rho(\tau)+3\theta^<_\sigma(\tau)}{\sqrt{2}}$. Using similar steps as for $\delta S^{(tt)}$, we obtain the correction to the action proportional $t\Delta$:

$$\delta S^{(t\Delta)} \approx \frac{1}{4}\frac{i\,t_\uparrow\Delta}{(2\pi a)^2}\frac{2dl}{\Lambda}\frac{1}{2K_\sigma}C\left(\frac{1}{2K_\sigma}\right)\int_0^\beta dT\gamma_\downarrow(T)\Gamma_\downarrow(T)\cos\frac{\theta_\rho(T)-\theta_\sigma(T)}{\sqrt{2}}. \tag{B.18}$$

Similarly, we evaluate the contribution to the effective action from $t_\uparrow\Delta_{\mathrm{AN}}$ term to find

$$\begin{aligned}\delta S^{(t\Delta_{\mathrm{AN}})} &= -\frac{1}{2}\int d\tau\int d\tau'\frac{-i\,t_\uparrow\Delta_{\mathrm{AN}}}{(2\pi a)^2}\gamma_\uparrow(\tau)\Gamma_\uparrow(\tau)\,\gamma_\uparrow(\tau')\gamma_\downarrow(\tau')\Gamma_\uparrow(\tau')\Gamma_\downarrow(\tau') \\ &\quad\times\left(\langle\cos\frac{\theta_\rho(\tau)+\theta_\sigma(\tau)}{\sqrt{2}}\cos\sqrt{2}\theta_\rho(\tau')\rangle - \langle\cos\frac{\theta_\rho(\tau)+\theta_\sigma(\tau)}{\sqrt{2}}\rangle\langle\cos\sqrt{2}\theta_\rho(\tau')\rangle\right) \\ &\approx \frac{1}{4}\frac{i\,t_\uparrow\Delta_{\mathrm{AN}}}{(2\pi a)^2}\frac{2dl}{\Lambda}\frac{1}{2K_\rho}C\left(\frac{1}{2K_\rho}\right)\int_0^\beta dT\gamma_\downarrow(T)\Gamma_\downarrow(T)\cos\frac{\theta_\rho(T)-\theta_\sigma(T)}{\sqrt{2}}.\end{aligned} \tag{B.19}$$

Once again here we dropped the irrelevant term $\cos\frac{3\theta^<_\rho(\tau)+3\theta(\tau)}{\sqrt{2}}$. Combining all the terms

in Eq. (B.11), we find the quadratic part of the RG flow Eq. (4.14) in the main text:

$$\frac{dt}{dl} = -\frac{\Delta t}{4\pi v K_\sigma} - \frac{\Delta_{\rm AN} t}{4\pi v K_\rho}. \tag{B.20}$$

B.2 Majorana Kramers pair - Luttinger liquid junction without $\mathbb{U}(1)$ symmetry

In this section we evaluate additional terms contributing to the RG equations when $U(1)$ symmetry is broken. We first consider the contribution of $\tilde{\Delta} t_\downarrow$ to the RG flow Eq. (4.38)in the main text:

$$\begin{aligned}
\delta S^{(\tilde{\Delta} t_\downarrow)} &= \frac{1}{2}\int d\tau \int d\tau' \frac{\tilde{\Delta}}{2\pi v}(-1)\gamma_\uparrow(\tau)\gamma_\downarrow(\tau)\frac{i t_\downarrow}{2\pi a}\gamma_\downarrow(\tau')\Gamma_\downarrow(\tau') \\
&\quad \times \frac{1}{2\sqrt{2}}\Big[\langle \partial_\tau\theta_\sigma(\tau) e^{\frac{i}{\sqrt{2}}(\theta_\sigma(\tau')-\theta_\rho(\tau'))}\rangle - \langle\partial_\tau\theta_\sigma(\tau)\rangle\langle e^{\frac{i}{\sqrt{2}}(\theta_\sigma(\tau')-\theta_\rho(\tau'))}\rangle \\
&\qquad + \langle \partial_\tau\theta_\sigma(\tau) e^{-\frac{i}{\sqrt{2}}(\theta_\sigma(\tau')-\theta_\rho(\tau'))}\rangle - \langle\partial_\tau\theta_\sigma(\tau)\rangle\langle e^{-\frac{i}{\sqrt{2}}(\theta_\sigma(\tau')-\theta_\rho(\tau'))}\rangle\Big] \\
&\approx -\frac{b^{-\frac{1}{4}}}{8\pi v}\frac{i\tilde{\Delta} t_\downarrow}{2\pi a}\int dT \gamma_\uparrow\Gamma_\downarrow \sin\frac{\theta_\rho^< - \theta_\sigma^<}{\sqrt{2}} \int ds\ \mathrm{sgn}(s)\partial_s g_\sigma(s) \\
&\approx \frac{\tilde{\Delta} t_\downarrow}{2\pi a}\frac{dl}{4\pi v K_\sigma}\int dT\ i\gamma_\uparrow\Gamma_\downarrow \sin\frac{\theta_\rho^< - \theta_\sigma^<}{\sqrt{2}}.
\end{aligned} \tag{B.21}$$

Here we use the definition $g_j(\tau-\tau') = \langle\theta_j^>(\tau)\theta_j^>(\tau')\rangle$with $g_j(0) = \ln b/K_j$, and the following relations

$$\begin{aligned}
\langle\partial_\tau\theta_\sigma(\tau)e^{\pm\frac{i}{\sqrt{2}}\theta_\sigma(\tau')}\rangle &= \partial_\tau\theta_\sigma^<(\tau)\; e^{\pm\frac{i}{\sqrt{2}}\theta_\sigma^<(\tau')}e^{-\frac{1}{4}\langle(\theta_\sigma^>)^2\rangle} \\
&\quad + e^{\pm\frac{i}{\sqrt{2}}\theta_\sigma(\tau')}\langle\partial_\tau\theta_\sigma^>(\tau)e^{\pm\frac{i}{\sqrt{2}}\theta_\sigma^>(\tau')}\rangle, \qquad \text{(B.22)}\\
\langle\partial_\tau\theta_\sigma(\tau)\rangle\langle e^{\pm\frac{i}{\sqrt{2}}\theta_\sigma(\tau')}\rangle &= \partial_\tau\theta_\sigma^<(\tau)\; e^{\pm\frac{i}{\sqrt{2}}\theta_\sigma^<(\tau')}e^{-\frac{1}{4}\langle(\theta_\sigma^>)^2\rangle,} \qquad \text{(B.23)}\\
\langle\partial_\tau\theta_\sigma^>(\tau)e^{\pm\frac{i}{\sqrt{2}}\theta_\sigma^>(\tau')}\rangle &= \frac{\pm i}{\sqrt{2}}\partial_\tau\langle\theta_\sigma^>(\tau)\theta_\sigma^>(\tau')\rangle e^{-\frac{1}{4}\langle(\theta_\sigma^>)^2\rangle} \qquad \text{(B.24)}\\
\lim_{\delta\to 0^+}\int ds\; \mathrm{sgn}(s)\partial_s g_\sigma(s)e^{-\delta|s|} &= -\frac{2}{K_\sigma}\ln b \approx -\frac{2dl}{K_\sigma}. \qquad \text{(B.25)}
\end{aligned}$$

Following the similar procedure as in Sec. B.1, we get the correction to the RG equation,

$$\frac{d\widetilde{t_{\uparrow\downarrow}}}{dl} = -\frac{\tilde{\Delta}t_\downarrow}{2\pi v K_\sigma}. \qquad \text{(B.26)}$$

Similarly, the contribution of $\tilde{\Delta}t_\uparrow$ will generate the following contribution:

$$\frac{d\widetilde{t_{\downarrow\uparrow}}}{dl} = -\frac{\tilde{\Delta}t_\uparrow}{2\pi v K_\sigma}. \qquad \text{(B.27)}$$

The cross term $\tilde{\Delta}\tilde{t}$ leads to the similar correction to t. It is also straightforward to compute the contributions from $\Delta\tilde{t_i}$ terms using the same technique.

We now evaluate the contribution of the $t\tilde{t}$ term in the second order expansion of S_T, see Eq. (4.40) in the main text. During this calculation we will encounter the expressions such as $e^{i\frac{\theta_\rho(\tau)+\theta_\sigma(\tau)}{\sqrt{2}}}e^{-i\frac{\theta_\rho(\tau')+\theta_\sigma(\tau')}{\sqrt{2}}}$. This term will contribute to the RG flow of $\tilde{\Delta}$. In order to demostrate this, one needs to carefully expand above expression up to the linear order

in s:

$$e^{i\frac{\theta_\rho(\tau)+\theta_\sigma(\tau)}{\sqrt{2}}}e^{-i\frac{\theta_\rho(\tau')+\theta_\sigma(\tau')}{\sqrt{2}}} = e^{i\frac{\theta_\rho(\tau)-\theta_\rho(\tau')}{\sqrt{2}}}e^{i\frac{\theta_\sigma(\tau)-\theta_\sigma(\tau')}{\sqrt{2}}} \tag{B.28}$$

$$= \left(1+s\frac{i\partial_T\theta_\rho}{\sqrt{2}}\right)\frac{1}{(\Lambda|s|+1)^{\frac{1}{2K_\rho}}}\left(1+s\frac{i\partial_T\theta_\sigma}{\sqrt{2}}\right)\frac{1}{(\Lambda|s|+1)^{\frac{1}{2K_\sigma}}} \tag{B.29}$$

$$\sim \left(\frac{1}{\Lambda|s|+1}+\frac{\mathrm{sgn}(s)}{\Lambda}\frac{i\partial_T(\theta_\rho+\theta_\sigma)}{\sqrt{2}}\right)\frac{1}{(\Lambda|s|+1)^{\frac{1}{2K_\rho}+\frac{1}{2K_\sigma}-1}} \tag{B.30}$$

After some algebra, one finds

$$\begin{aligned}
\delta S^{t\widetilde{t}} &= -\frac{1}{2}\int d\tau\int d\tau'\Bigg\{\frac{t\widetilde{t}}{(2\pi a)^2}i\gamma_\uparrow(\tau)\Gamma_\uparrow(\tau)i\gamma_\downarrow(\tau')\Gamma_\uparrow(\tau') \\
&\quad\times\Big[\langle\cos\frac{\theta_\rho+\theta_\sigma(\tau)}{\sqrt{2}}\sin\frac{\theta_\rho+\theta_\sigma(\tau')}{\sqrt{2}}\rangle-\langle\cos\frac{\theta_\rho+\theta_\sigma(\tau)}{\sqrt{2}}\rangle\langle\sin\frac{\theta_\rho+\theta_\sigma(\tau')}{\sqrt{2}}\rangle\Big] \\
&\quad+\frac{t\widetilde{t}}{(2\pi a)^2}i\gamma_\downarrow(\tau)\Gamma_\downarrow(\tau)i\gamma_\uparrow(\tau')\Gamma_\downarrow(\tau') \\
&\quad\times\Big[\langle\cos\frac{\theta_\rho-\theta_\sigma(\tau)}{\sqrt{2}}\sin\frac{\theta_\rho-\theta_\sigma(\tau')}{\sqrt{2}}\rangle-\langle\cos\frac{\theta_\rho-\theta_\sigma(\tau)}{\sqrt{2}}\rangle\langle\sin\frac{\theta_\rho-\theta_\sigma(\tau')}{\sqrt{2}}\rangle\Big]\Bigg\} \\
&\approx \frac{1}{2}\int dT\int ds\frac{t\widetilde{t}}{(2\pi a)^2\Lambda}\gamma_\uparrow\gamma_\downarrow\frac{\partial_\tau\theta_\sigma}{\sqrt{2}}\frac{\cos(s\Lambda)}{(\Lambda|s|+1)^{\frac{1}{2K_\rho}+\frac{1}{2K_\sigma}-1}}\left(\frac{1}{2K_\rho}+\frac{1}{2K_\sigma}\right)dl \\
&\approx -\frac{1}{8\pi v}\frac{t\widetilde{t}}{2\pi v}\left(\frac{1}{K_\rho}+\frac{1}{K_\sigma}\right)dl\,C\left(\frac{1}{2K_\rho}+\frac{1}{2K_\sigma}-1\right)\int dT i\gamma_\uparrow\Gamma_\uparrow\frac{i\partial_T\theta_\sigma}{\sqrt{2}}.
\end{aligned} \tag{B.31}$$

Once again we have to multiply the above expression by 2 due to the symmetry of between τ and τ'.

Taking into account above results, one finds the following system of RG equations for

generic values of K_ρ and K_σ:

$$\frac{dt}{dl} = \left(1 - \frac{1}{4K_\rho} - \frac{1}{4K_\sigma} - \frac{C(1/2K_\sigma)\Delta}{4\pi v K_\sigma}\right) t - \frac{\tilde{\Delta}\tilde{t}}{2\pi v K_\sigma}, \tag{B.32}$$

$$\frac{d\tilde{t}}{dl} = \left(1 - \frac{1}{4K_\rho} - \frac{1}{4K_\sigma} + \frac{C(1/2K_\sigma)\Delta}{4\pi v K_\sigma}\right) \tilde{t} - \frac{\tilde{\Delta}t}{2\pi v K_\sigma}, \tag{B.33}$$

$$\frac{d\Delta}{dl} = -\frac{C(1/2K_\rho)}{4\pi v}\left(\frac{1}{K_\rho} - 1\right)(t^2 - \tilde{t}^2), \tag{B.34}$$

$$\frac{d\tilde{\Delta}}{dl} = -\frac{C(1/2K_\rho + 1/2K_\sigma - 1)}{4\pi v}\left(\frac{1}{K_\rho} + \frac{1}{K_\sigma}\right) t\tilde{t}, \tag{B.35}$$

Compare with Eqs. (4.37) and (4.40) in the main text. Provided the coefficients $C(x_i)$ are non-zero (i.e. $K_\rho, K_\sigma \neq 1/2$), one can rescale $C(1/2K_\sigma)\Delta \to \Delta$, $\sqrt{C(1/2K_\rho)C(1/2K_\sigma)}\, t \to t$ and $\sqrt{C(1/2K_\rho)C(1/2K_\sigma)}\, \tilde{t} \to \tilde{t}$ to absorb the $C(\nu)$'s in first three equations. Then the last equation becomes

$$\frac{d\tilde{\Delta}}{dl} = -\frac{C(1/2K_\rho + 1/2K_\sigma - 1)}{C(1/2K_\rho)C(1/2K_\sigma)}\left(\frac{1}{K_\rho} + \frac{1}{K_\sigma}\right)\frac{t\tilde{t}}{4\pi v}, \tag{B.36}$$

and we recover Eq. (4.43).

Appendix C

Slave-boson mean field theory and Gaussian fluctuations

C.1 Green's functions in the slave-boson mean-field equations

To evaluate the correlation functions in Eqs. (4.83) and (4.84), we first transform the action to the Matsubara frequency domain after the mean-field approximation:

$$\begin{aligned} S_{\rm sb} = & \sum_{n,\sigma} \Bigg[\sum_k \psi^*_{k,n,\sigma}(-i\omega_n + \xi_k)\psi_{k,n,\sigma} + f^*_{n,\sigma}(-i\omega_n + \tilde{\epsilon})f_{n,\sigma} + i\lambda_\sigma b\gamma^1_{-n,\sigma}(f_{n,\sigma} + f^*_{-n,\sigma}) \\ & + \sum_k tb(f^*_{n,\sigma}\psi_{k,n,\sigma} + \psi^*_{k,n,\sigma}f_{n,\sigma}) \\ & - \frac{1}{2}\sum_{i=1,2} i\omega_n\gamma^i_{-n,\sigma}\gamma^i_{n,\sigma} + i\delta_{1\sigma}\gamma^1_{-n,\sigma}\gamma^2_{n,\sigma} + i\delta_2\gamma^1_{-n,\sigma}\gamma^2_{n,-\sigma} \Bigg], \end{aligned} \tag{C.1}$$

where $\tilde{\epsilon} = \epsilon + \eta$. Next, we integrate out the NL fermion fields ψ^* and ψ to find the following effective action:

$$\begin{aligned} S_{\text{eff}}(f,\gamma^1,\gamma^2) =& \sum_{n,\sigma}\Bigg[f^*_{n,\sigma}(-i\omega_n + \tilde{\epsilon} + \sum_k \frac{t^2b^2}{i\omega_n - \xi_k})f_{n,\sigma} + i\lambda_\sigma b\gamma^1_{-n,\sigma}(f_{n,\sigma} + f^*_{-n,\sigma}) \\ & - \sum_{i=1,2}\frac{i\omega_n}{2}\gamma^i_{-n,\sigma}\gamma^i_{n,\sigma} + i\delta_{1\sigma}\gamma^1_{-n,\sigma}\gamma^2_{n,\sigma} + i\delta_2\gamma^1_{-n,\sigma}\gamma^2_{n,-\sigma}\Bigg], \qquad \text{(C.2)} \\ =& \sum_{n,\sigma}\Bigg[f^*_{n,\sigma}(-i(\omega_n + \Gamma_n) + \tilde{\epsilon})f_{n,\sigma} + i\lambda_\sigma b\gamma^1_{-n,\sigma}(f_{n,\sigma} + f^*_{-n,\sigma}) \\ & - \sum_{i=1,2}\frac{i\omega_n}{2}\gamma^i_{-n,\sigma}\gamma^i_{n,\sigma} + i\delta_{1\sigma}\gamma^1_{-n,\sigma}\gamma^2_{n,\sigma} + i\delta_2\gamma^1_{-n,\sigma}\gamma^2_{n,-\sigma}\Bigg], \qquad \text{(C.3)} \end{aligned}$$

where $\Gamma_n = \Gamma b^2 \operatorname{sgn}\omega_n$ and $\Gamma = \pi t^2 \nu_F$ and ν_F is the density of states in NL at the Fermi energy. To compute the correlation functions in the mean-field equation, we perform a canonical transformation for the Majorana fields $\gamma^1_\sigma = (c^*_\sigma + c_\sigma)/\sqrt{2}$, $\gamma^2_\uparrow = i(c^*_\uparrow - c_\uparrow)/\sqrt{2}$ and $\gamma^2_\downarrow = -i(c^*_\downarrow - c_\downarrow)/\sqrt{2}$. Then the effective action can be written as

$$\begin{aligned} S_{\text{eff}}(f,c) =& \sum_{n,\sigma}\Bigg[f^*_{n,\sigma}(-i(\omega_n+\Gamma_n)+\tilde{\epsilon})f_{n,\sigma} + \frac{i\lambda_\sigma b}{\sqrt{2}}(c^*_{n,\sigma}f_{n,\sigma} + c_{-n,\sigma}f^*_{-n,\sigma} + c_{-n,\sigma}f_{n,\sigma} + c^*_{n,\sigma}f^*_{-n,\sigma}) \\ & - i\omega_n c^*_{n,\sigma}c_{n,\sigma} + \delta_1 c^*_{n,\sigma}c_{n,\sigma} + \delta_2(c^*_{n,\uparrow}c^*_{-n,\downarrow} - c_{n,\uparrow}c_{-n,\downarrow})\Bigg] \qquad \text{(C.4)} \end{aligned}$$

We now introduce the Nambu space and rewrite $S_{\text{eff}} = \sum_{n>0}\phi^\dagger_n A_n \phi_n$ with

$$\phi^\dagger_n = (f^*_{n,\uparrow},\, f^*_{n,\downarrow},\, c^*_{n,\uparrow},\, c^*_{n,\downarrow},\, f_{-n,\uparrow},\, f_{-n,\downarrow},\, c_{-n,\uparrow},\, c_{-n,\downarrow}) \qquad \text{(C.5)}$$

and

$$A_n = \begin{pmatrix} \tilde{\epsilon}-i(\omega_n+\Gamma_n) & 0 & -\frac{ib\lambda}{\sqrt{2}} & 0 & 0 & 0 & -\frac{ib\lambda}{\sqrt{2}} & 0 \\ 0 & \tilde{\epsilon}-i(\omega_n+\Gamma_n) & 0 & \frac{ib\lambda}{\sqrt{2}} & 0 & 0 & 0 & \frac{ib\lambda}{\sqrt{2}} \\ \frac{ib\lambda}{\sqrt{2}} & 0 & -i\omega_n+\delta_1 & 0 & i\frac{ib\lambda}{\sqrt{2}} & 0 & 0 & \delta_2 \\ 0 & -\frac{ib\lambda}{\sqrt{2}} & 0 & -i\omega_n+\delta_1 & 0 & -i\frac{ib\lambda}{\sqrt{2}} & -\delta_2 & 0 \\ 0 & 0 & -i\frac{ib\lambda}{\sqrt{2}} & 0 & -\tilde{\epsilon}-i(\omega_n+\Gamma_n) & 0 & -\frac{ib\lambda}{\sqrt{2}} & 0 \\ 0 & 0 & 0 & i\frac{ib\lambda}{\sqrt{2}} & 0 & -\tilde{\epsilon}-i(\omega_n+\Gamma_n) & 0 & \frac{ib\lambda}{\sqrt{2}} \\ \frac{ib\lambda}{\sqrt{2}} & 0 & 0 & -\delta_2 & i\frac{ib\lambda}{\sqrt{2}} & 0 & -i\omega_n-\delta_1 & 0 \\ 0 & -\frac{ib\lambda}{\sqrt{2}} & \delta_2 & 0 & 0 & -i\frac{ib\lambda}{\sqrt{2}} & 0 & -i\omega_n-\delta_1 \end{pmatrix}. \tag{C.6}$$

The correlation functions can be calculated as

$$\begin{aligned} G_1(\omega_n) &\equiv \langle f_{n,\uparrow}\gamma^1_{-n,\uparrow}\rangle = \frac{1}{\sqrt{2}}(\langle f_{n,\uparrow}c_{-n,\uparrow}\rangle + \langle f_{n,\uparrow}c^*_{n,\uparrow}\rangle) && \text{(C.7)} \\ &= \frac{\Theta(n)}{\sqrt{2}}\left([A_n^{-1}]_{17}+[A_n^{-1}]_{13}\right) - \frac{\Theta(-n)}{\sqrt{2}}\left([A_{-n}^{-1}]_{35}+[A_{-n}^{-1}]_{75}\right) && \text{(C.8)} \\ &= \frac{\omega_n}{i(\omega_n+\Gamma_n)-\tilde{\epsilon}}\cdot\frac{\lambda b}{\omega_n^2+\delta_1^2+\delta_2^2+\frac{2b^2\lambda^2\omega_n(\omega_n+\Gamma_n)}{(\omega_n+\Gamma_n)^2+\tilde{\epsilon}^2}} && \text{(C.9)} \\ &= -\langle f_{n,\downarrow}\gamma^1_{-n,\downarrow}\rangle, && \text{(C.10)} \\ G_f(\omega_n) &\equiv \langle f_{n,\uparrow}f^*_{n,\uparrow}\rangle = \Theta(n)[A_n^{-1}]_{11} - \Theta(-n)[A_{-n}^{-1}]_{55} = \frac{-1+i\lambda b G_1(\omega_n)}{i(\omega_n+\Gamma_n)-\tilde{\epsilon}} && \text{(C.11)} \\ &= \langle f_{n,\downarrow}f^*_{n,\downarrow}\rangle. && \text{(C.12)} \end{aligned}$$

Notice the following relationship between correlation functions

$$\langle f^*_{-n,\uparrow}\gamma^1_{-n,\uparrow}\rangle = -\langle f^*_{-n,\downarrow}\gamma^1_{-n,\downarrow}\rangle = -G_1(\omega_n)^*. \tag{C.13}$$

To compute $\langle\psi^*_{k,n,\sigma}f_{n,\sigma}\rangle$, we have to integrate out NL fermions $\psi^*_{k',\sigma}$ and $\psi_{k',\sigma}$ for all $k'\neq k$ from Eq. (C.1). This procedure leaves the terms $\sum_{n,\sigma}\psi^*_{k,n,\sigma}(-i\omega_n+\xi_k)\psi_{k,n,\sigma}$ and $tb(f^*_{n,\sigma}\psi_{k,n,\sigma}+\psi^*_{k,n,\sigma}f_{n,\sigma})$ in the effective action and shifts $i\Gamma_n\to i\Gamma_n+\frac{t^2b^2}{i\omega_n-\xi_k}$ such that

$S'_{\text{eff}} = \sum_{n>0} \Phi^\dagger B_n \Phi$ where

$$\Phi^\dagger = (\psi^*_{k,n,\uparrow},\, \psi^*_{k,n,\downarrow},\, \psi_{-n,\uparrow},\, \psi_{-n,\downarrow},\, f^*_{n,\uparrow},\, f^*_{n,\downarrow},\, c^*_{n,\uparrow},\, c^*_{n,\downarrow},\, f_{-n,\uparrow},\, f_{-n,\downarrow},\, c_{-n,\uparrow},\, c_{-n,\downarrow}) \quad \text{(C.14)}$$

and

$$B_n = \begin{pmatrix}
\xi_k - i\omega_n & 0 & 0 & 0 & bt & 0 & 0 & 0 & 0 & 0 & 0 & 0 \\
0 & \xi_k - i\omega_n & 0 & 0 & 0 & bt & 0 & 0 & 0 & 0 & 0 & 0 \\
0 & 0 & -\xi_k - i\omega_n & 0 & 0 & 0 & 0 & 0 & -bt & 0 & 0 & 0 \\
0 & 0 & 0 & -\xi_k - i\omega_n & 0 & 0 & 0 & 0 & 0 & -bt & 0 & 0 \\
bt & 0 & 0 & 0 & & & & & & & & \\
0 & bt & 0 & 0 & & & & & & & & \\
0 & 0 & 0 & 0 & & & & & & & & \\
0 & 0 & 0 & 0 & & & A_n(i\Gamma_n \to i\Gamma_n + \frac{t^2 b^2}{i\omega_n \,\mathrm{sgn}(n) - \xi_k}) & & & & & \\
0 & 0 & -bt & 0 & & & & & & & & \\
0 & 0 & 0 & -bt & & & & & & & & \\
0 & 0 & 0 & 0 & & & & & & & & \\
0 & 0 & 0 & 0 & & & & & & & &
\end{pmatrix}. \quad \text{(C.15)}$$

Then straightforward calculation gives

$$G_T(k,\omega_n) \equiv \langle f_{n,\uparrow} \psi^*_{k,n,\uparrow} \rangle = \Theta(n)[B_n^{-1}]_{51} - \Theta(-n)[B_{-n}^{-1}]_{39} = \frac{tb\, G_f(\omega_n)}{i\omega_n - \xi_k} \quad \text{(C.16)}$$

$$= \langle f_{n,\downarrow} \psi^*_{k,n,\downarrow} \rangle \quad \text{(C.17)}$$

Plugging the above correlation functions back into the mean-field equations (4.83) and (4.84) leads to

$$b^2 - \frac{2}{\beta} \sum_n G_f(\omega_n) e^{i\omega_n 0^+} = 1 \quad \text{(C.18)}$$

$$2b\eta - \frac{4t}{\beta} \sum_{k,n} \mathrm{Re}[G_T(k,\omega_n) e^{i\omega_n 0^+}] - \frac{4\lambda}{\beta} \sum_n \mathrm{Re}[i G_1(\omega_n) e^{i\omega_n 0^+}] = 0 \quad \text{(C.19)}$$

Now we evaluate Matsubara sum in Eq. (C.18) using the conventional analytic continuation method with cut along the real frequency axis due to the non-analyticity of $\mathrm{sgn}(\omega_n) = \mathrm{sgn}(\mathrm{Im}\,\omega)$.

$$\begin{aligned}
-\frac{2}{\beta}\sum_n G_f(\omega_n) &= \frac{2}{\beta}\sum_n \left[\frac{1}{i\omega_n - \tilde{\epsilon} + i\Gamma b^2\,\mathrm{sgn}(\omega_n)} - \frac{i\lambda G_1(\omega_n)}{i\omega_n - \tilde{\epsilon} + i\Gamma b^2\,\mathrm{sgn}(\omega_n)}\right] \\
&= \frac{i}{\pi}\oint d\omega n_F(\omega)\left[\frac{1}{\omega - \tilde{\epsilon} + i\Gamma b^2\,\mathrm{sgn}(\mathrm{Im}\,\omega)} - \frac{i\lambda G_1(-i\omega)}{\omega - \tilde{\epsilon} + i\Gamma b^2\,\mathrm{sgn}(\mathrm{Im}\,\omega)}\right] \\
&= \frac{1}{\pi}\int_{-\infty}^{\infty} d\omega n_F(\omega)\left[\frac{2\Gamma b^2}{(\omega-\tilde{\epsilon})^2 + (\Gamma b^2)^2} + F(b,\eta)\right] \\
&\overset{T\to 0}{\approx} 1 - \frac{2}{\pi}\arctan\frac{\tilde{\epsilon}}{\Gamma b^2} + \frac{1}{\pi}\int_{-\infty}^{0} d\omega F(b,\eta),
\end{aligned} \tag{C.20}$$

where

$$n_F(\omega) = \frac{1}{e^{\beta\omega}+1}, \tag{C.21}$$

$$F(b,\eta) = 2\,\mathrm{Re}\left[\frac{i\omega\lambda^2 b^2}{(\omega - \tilde{\epsilon} + i\Gamma b^2)^2}\cdot\frac{1}{\omega^2 - \delta_1^2 - \delta_2^2 - \frac{2b^2\lambda^2(\omega^2 + i\omega\Gamma b^2)}{(\omega + i\Gamma b^2)^2 - \tilde{\epsilon}^2}}\right]. \tag{C.22}$$

The last term in Eq.(C.20) is $\mathcal{O}(\lambda^2 b^2)$. Given that $b \ll 1$ we will ignore this term for a moment. Plugging Eq.(C.20) back into Eq.(C.18) yeilds $\tilde{\epsilon} \approx \frac{\pi}{2}\Gamma b^4 \sim b^4$. Therefore, in the limit of small b, the contribution from $\tilde{\epsilon}$ is $\mathcal{O}(b^4)$. Including the last term in Eq.(C.20) does not change this conclusion.

Next, we evaluate the second term in Eq. (C.19).

$$\begin{aligned}
-\frac{4t}{\beta}\sum_{k,n} G_T(k,\omega_n) &= \frac{4t^2 b}{\beta}\sum_{k,n}\frac{1}{i\omega_n - \xi_k}\left[\frac{1}{i\omega_n - \tilde{\epsilon} + i\Gamma b^2\,\mathrm{sgn}(\omega_n)} - \frac{i\lambda b G_1(\omega_n)}{i\omega_n - \tilde{\epsilon} + i\Gamma b^2\,\mathrm{sgn}(\omega_n)}\right] \\
&= -\frac{4i\Gamma b}{\beta}\sum_n\left[\frac{\mathrm{sgn}(\omega_n)}{i\omega_n - \tilde{\epsilon} + i\Gamma b^2\,\mathrm{sgn}(\omega_n)} - \frac{i\lambda b G_1(\omega_n)\,\mathrm{sgn}(\omega_n)}{i\omega_n - \tilde{\epsilon} + i\Gamma b^2\,\mathrm{sgn}(\omega_n)}\right]
\end{aligned} \tag{C.23}$$

The first term in the above equation can be calculated by introducing a UV cutoff Λ.

$$\begin{aligned}
-\frac{4i\Gamma b}{\beta}\sum_n \frac{\mathrm{sgn}(\omega_n)}{i\omega_n-\tilde{\epsilon}+i\Gamma b^2\,\mathrm{sgn}(\omega_n)} &= \frac{4\Gamma b}{2\pi}\oint d\omega n_F(\omega)\frac{\mathrm{sgn}(\mathrm{Im}\,\omega)}{\omega-\tilde{\epsilon}+i\Gamma b^2\,\mathrm{sgn}(\mathrm{Im}\,\omega)} \\
&= \frac{4\Gamma b}{\pi}\int_{-\infty}^{\infty} d\omega n_F(\omega)\frac{\omega-\tilde{\epsilon}}{(\omega-\tilde{\epsilon})^2+(\Gamma b^2)^2} \\
&\overset{T\to 0}{\approx} \frac{4\Gamma b}{\pi}\int_{-\Lambda}^{0} d\omega\frac{\omega-\tilde{\epsilon}}{(\omega-\tilde{\epsilon})^2+(\Gamma b^2)^2} \\
&\overset{\tilde{\epsilon}\to 0}{\approx} -\frac{4\Gamma b}{\pi}\ln\frac{\Lambda}{|\Gamma b^2|}
\end{aligned} \tag{C.24}$$

Since the second term in Eq. (C.23) are not UV divergent and $\mathcal{O}(\lambda^2 b^2)$, we can ignore its contribution. Finally, we evaluate the last term in Eq. (C.19).

$$\begin{aligned}
-\frac{4\lambda}{\beta}\sum_n iG_1(\omega_n) &= -\frac{4\lambda^2 b}{\beta}\sum_n \frac{i\omega_n}{i\omega_n-\tilde{\epsilon}+i\Gamma b^2\,\mathrm{sgn}\,\omega_n}\,\frac{1}{\omega_n^2+\delta_1^2+\delta_2^2+\frac{2b^2\lambda^2\omega_n(\omega_n+\Gamma b^2\,\mathrm{sgn}\,\omega_n)}{(\omega_n+\Gamma b^2\,\mathrm{sgn}\,\omega_n)^2+\tilde{\epsilon}^2}} \\
&= \frac{4}{\pi b}\int_{-\infty}^{\infty} d\omega n_F(\omega)\,\mathrm{Re}\left[\frac{i\omega\lambda^2 b^2}{\omega-\tilde{\epsilon}+i\Gamma b^2}\,\frac{1}{\omega^2-\delta_1^2-\delta_2^2-\frac{2b^2\lambda^2(\omega^2+i\omega\Gamma b^2)}{(\omega+i\Gamma b^2)^2-\tilde{\epsilon}^2}}\right] \\
&\overset{T\to 0}{\approx} \frac{4}{\pi b}\int_{-\infty}^{0} d\omega\,\mathrm{Re}\left[\frac{i\omega\lambda^2 b^2}{\omega-\tilde{\epsilon}+i\Gamma b^2}\,\frac{1}{\omega^2-\delta_1^2-\delta_2^2-\frac{2b^2\lambda^2(\omega^2+i\omega\Gamma b^2)}{(\omega+i\Gamma b^2)^2-\tilde{\epsilon}^2}}\right] \\
&\overset{\tilde{\epsilon},\delta_1,\delta_2\to 0}{\approx} \frac{4}{\pi b}\int_{-\infty}^{0} d\omega\frac{\omega\lambda^2\Gamma b^4}{(\omega^2-2b^2\lambda^2)^2+\omega^2\Gamma^2 b^4} \\
&= -\frac{2\Gamma b}{\pi}\int_0^{\infty} dx\frac{1}{x^2+(r-4)x+4}
\end{aligned} \tag{C.25}$$

where $r=\Gamma^2 b^2/\lambda^2$ is a dimensionless quantity. In the limit of $r\ll 1$ we get,

$$-\frac{4\lambda}{\beta}\sum_n iG_1(\omega_n)\sim -\frac{2|\lambda|}{\sqrt{2}}+\mathcal{O}(b) \tag{C.26}$$

After collecting all the contributions in Eq. (C.19) and expanding them to the lowest

order in r, one finds the following equation for b:

$$\eta - \frac{2\Gamma}{\pi} \ln \frac{\Lambda}{\Gamma b^2} - \frac{|\lambda|}{\sqrt{2}b} = 0. \tag{C.27}$$

C.2 Gaussian fluctuations

In this section we present the details of the calculation of the matrix elements in Eq. (4.106). Once we expand the Tr lns in Eq. (4.95) and collecting the terms, we find Eq. (4.106) with

$$\Gamma_\nu^{\dot\theta\dot\theta} = -\frac{2}{\beta} \sum_{n>0} \left[G_n^p G_{n+\nu}^p + G_n^h G_{n+\nu}^h - 2\Delta_n \Delta_{n+\nu} \right] \tag{C.28}$$

$$\begin{aligned}\Gamma_\nu^{\dot\theta s} = {} & 2i\bar{s} + \frac{2i\bar{s}}{\beta} \sum_{n>0} \big[G_n^p (G_{X,n} + G_{X,n+\nu}) G_{n+\nu}^p + G_n^p (G_{\gamma,n} + G_{\gamma,n+\nu}) \Delta_{n+\nu} \\ & - G_n^h (\tilde{G}_{X,n} + \tilde{G}_{X,n+\nu}) G_{n+\nu}^h - G_n^h (G_{\gamma,n} + G_{\gamma,n+\nu}) \Delta_{n+\nu} + \Delta_n G_{\gamma,n} (G_{n+\nu}^p - G_{n+\nu}^h) \\ & + \Delta_n G_{\gamma,n+\nu} (G_{n+\nu}^p - G_{n+\nu}^h) + \Delta_n (\tilde{G}_{X,n} - G_{X,n}) \Delta_{n+\nu} + \Delta_n (\tilde{G}_{X,n+\nu} - G_{X,n+\nu}) \Delta_{n+\nu} \big]\end{aligned} \tag{C.29}$$

$$\Gamma_\nu^{ss} = \Gamma_\nu^{s(0)} + \Gamma_\nu^{s(2)} + \Gamma_\nu^{s(4)} \tag{C.30}$$

$$\Gamma_\nu^{s(0)} = 2(\bar{\eta} - i\omega_\nu) \tag{C.31}$$

$$\Gamma_\nu^{s(2)} = \frac{4}{\beta} \sum_{n>0} \left[G_n^p G_{X,n+\nu} + 2\Delta_n G_{\gamma,n+\nu} + G_n^h \tilde{G}_{X,n+\nu} \right] \tag{C.32}$$

$$\Gamma_\nu^{s(4)} = \frac{4\bar{s}^2}{\beta}\sum_{n>0}\big[G_n^p G_{X,n} G_{n+\nu}^p G_{X,n+\nu} + G_{X,n} G_n^p G_{X,n} G_{n+\nu}^p + G_n^h \tilde{G}_{X,n} G_{n+\nu}^h \tilde{G}_{X,n+\nu}$$
$$+\tilde{G}_{X,n} G_n^h \tilde{G}_{X,n} G_{n+\nu}^h + G_n^p G_{\gamma,n} G_{X,n+\nu}\Delta_{n+\nu} + G_n^p G_{\gamma,n} G_{X,n}\Delta_{n+\nu} + G_n^p G_{\gamma,n} G_{X,n+\nu}\Delta_n$$
$$+G_n^p G_{\gamma,n+\nu} G_{X,n}\Delta_n + 2G_n^p G_{\gamma,n+\nu} G_{X,n}\Delta_{n+\nu} + G_{n+\nu}^p G_{\gamma,n} G_{X,n}\Delta_n + G_n^p G_{\gamma,n+\nu} G_{X,n+\nu}\Delta_n$$
$$+G_n^h G_{\gamma,n+\nu} G_{X,n+\nu}\Delta_n + G_n^h G_{\gamma,n}\tilde{G}_{X,n+\nu}\Delta_{n+\nu} + G_n^h G_{\gamma,n}\tilde{G}_{X,n}\Delta_{n+\nu} + G_n^h G_{\gamma,n} G_{X,n+\nu}\Delta_n$$
$$+G_n^h G_{\gamma,n+\nu} G_{X,n}\Delta_n + 2G_n^h G_{\gamma,n+\nu}\tilde{G}_{X,n}\Delta_{n+\nu} + G_{n+\nu}^h G_{\gamma,n}\tilde{G}_{X,n}\Delta_n + 2\Delta_n G_{\gamma,n}\Delta_{n+\nu} G_{\gamma,n+\nu}$$
$$+2\Delta_n G_{\gamma,n}\Delta_{n+\nu} G_{\gamma,n} + 2\Delta_n G_{X,n}\Delta_{n+\nu}\tilde{G}_{X,n+\nu} + 2\Delta_n G_{X,n}\Delta_{n+\nu}\tilde{G}_{X,n}$$
$$+2G_n^p G_{\gamma,n} G_{n+\nu}^h G_{\gamma,n+\nu} + G_n^p G_{\gamma,n} G_{n+\nu}^h G_{\gamma,n} + G_{n+\nu}^p G_{\gamma,n} G_n^h G_{\gamma,n}\big] \tag{C.33}$$

where

$$G_{X,n} = G_{\psi,n} + G_{\gamma,n} = \tilde{G}_{X,n}. \tag{C.34}$$

Plugging in the mean-field solution $\bar{\eta} \approx -\epsilon$ leads to

$$G_{f,n} = \frac{1}{i\omega_n - \bar{s}^2(G_{\psi,n} + G_{\gamma,n})} = \tilde{G}_{f,n} \;\rightarrow\; G_n^p = G_n^h. \tag{C.35}$$

As a result, we get $\Gamma_\nu^{\dot{\theta}s} = 2i\bar{s}$ near the mean field solution.

To evaluate $\Gamma_\nu^{\dot{\theta}\dot{\theta}}$ and Γ_ν^{ss}, we need to sum over the fermionic Matsubara frequency ω_n. It can be done using analytical continuation $\omega_n = -i\omega$ and integration along the contour shown in Fig. C.1 a). One can see that the summation over Matsubara frequency ω_n can be evaluated by integrating along the branch cuts shown in Fig C.1 a). We note that in addition to the branch cuts, there are also contributions from the poles. However, one can show that the contribution from all the residues sums to zero. Thus, for $\nu > 0$ we

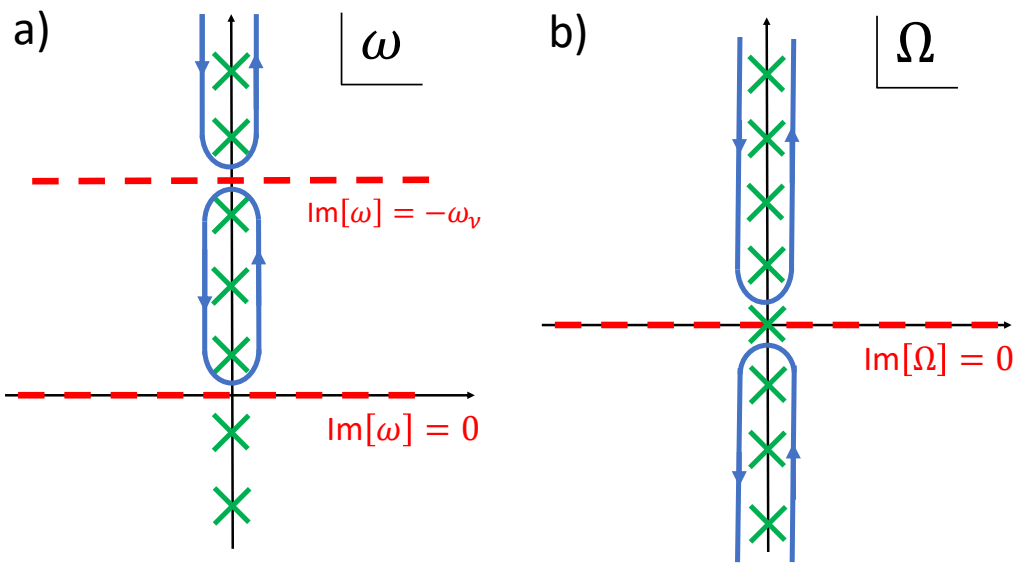

Figure C.1: a) Integration contour to evaluate fermionic Matsubara sum in Γ^{ss}_{ν} and $\Gamma^{\dot{\theta}\dot{\theta}}_{\nu}$. b) Integration contour for bosonic Matsubara sum in Eq. (4.110).

only have one branch cut $\mathrm{Im}[\omega] = 0$. For example,

$$\begin{aligned}\Gamma^{\dot{\theta}\dot{\theta}}_{\nu>0} &= \oint \frac{n_F(\omega)}{2\pi i}\left[G^p(\omega)G^p(\omega+i\omega_\nu) + G^h(\omega)G^h(\omega+i\omega_\nu) - 2\Delta(\omega)\Delta(\omega+i\omega_\nu)\right] \\ &= \lim_{\xi\to 0^+}\int_{-\Lambda}^{\Lambda}\frac{n_F(\omega)}{2\pi i}\left[G^p(\omega+i\xi)G^p(\omega+i\omega_\nu) + G^h(\omega+i\xi)G^h(\omega+i\omega_\nu)\right. \\ &\quad \left. -2\Delta(\omega+i\xi)\Delta(\omega+i\omega_\nu)\right] \qquad \text{(C.36)}\end{aligned}$$

where $n_F(\omega)$ is the Fermi distribution function which we eventually approximate as the theta function in the zero temperature limit; Λ is a UV cutoff. For $\nu < 0$ we have two additional integrals above and below branch cut at $\mathrm{Im}[\omega] = \omega_\nu$. Finally, we symmetrize the $\Gamma^{\dot{\theta}\dot{\theta}}_{\nu}$ and Γ^{ss}_{ν} by averaging the values for ν and $-\nu$. Similar method can be used for evaluating the boson correlation function Eq. (4.110). In this case the Matsubara sum can be transformed to an integration over contour shown in Fig. C.1 b).

Bibliography

[1] M. Abramovitz and I. A. Stegun. *Handbook of mathematical functions*. Dover, 1964.

[2] I. Affleck and D. Giuliano. Topological Superconductor-Luttinger Liquid Junctions. *Journ. Stat. Mech.*, 2013:P06011, May 2013.

[3] S. M. Albrecht, A. P. Higginbotham, M. Madsen, F. Kuemmeth, J. Jespersen, T. S. Nygard, P. Krogstrup, and C. M. Marcus. Exponential protection of zero modes in majorana islands. *Nature*, 531:206, 2016.

[4] J. Alicea. New directions in the pursuit of majorana fermions in solid state systems. *Reports on Progress in Physics*, 75(7):076501, 2012.

[5] J. Alicea, Y. Oreg, G. Refael, F. von Oppen, and M. P. A. Fisher. Non-abelian statistics and topological quantum information processing in 1D wire networks. *Nature Phys.*, 7(5):412–417, 2011.

[6] A. Altland and M. R. Zirnbauer. Nonstandard symmetry classes in mesoscopic normal-superconducting hybrid structures. *Phys. Rev. B*, 55:1142–1161, Jan 1997.

[7] N. E. Bickers. Review of techniques in the large-n expansion for dilute magnetic alloys. *Rev. Mod. Phys.*, 59:845–939, Oct 1987.

[8] B. Braunecker and P. Simon. Interplay between classical magnetic moments and superconductivity in quantum one-dimensional conductors: Toward a self-sustained topological majorana phase. *Phys. Rev. Lett.*, 111:147202, Oct 2013.

[9] P. M. R. Brydon, S. Das Sarma, H.-Y. Hui, and J. D. Sau. Topological yu-shiba-rusinov chain from spin-orbit coupling. *Phys. Rev. B*, 91:064505, Feb 2015.

[10] M. Cheng, M. Becker, B. Bauer, and R. M. Lutchyn. Interplay between kondo and majorana interactions in quantum dots. *Phys. Rev. X*, 4:031051, Sep 2014.

[11] M. Cheng, R. M. Lutchyn, V. Galitski, and S. Das Sarma. Tunneling of anyonic majorana excitations in topological superconductors. *Phys. Rev. B*, 82:094504, Sep 2010.

[12] T.-P. Choy, J. M. Edge, A. R. Akhmerov, and C. W. J. Beenakker. Majorana fermions emerging from magnetic nanoparticles on a superconductor without spin-orbit coupling. *Phys. Rev. B*, 84:195442, Nov 2011.

[13] S. B. Chung, H.-J. Zhang, X.-L. Qi, and S.-C. Zhang. Topological superconducting phase and majorana fermions in half-metal/superconductor heterostructures. *Phys. Rev. B*, 84:060510, Aug 2011.

[14] H. O. H. Churchill, V. Fatemi, K. Grove-Rasmussen, M. T. Deng, P. Caroff, H. Q. Xu, and C. M. Marcus. Superconductor-nanowire devices from tunneling to the multichannel regime: Zero-bias oscillations and magnetoconductance crossover. *Phys. Rev. B*, 87:241401, Jun 2013.

[15] P. Coleman. New approach to the mixed-valence problem. *Phys. Rev. B*, 29:3035–3044, Mar 1984.

[16] P. Coleman. Mixed valence as an almost broken symmetry. *Phys. Rev. B*, 35:5072–5116, Apr 1987.

[17] A. Cook and M. Franz. Majorana fermions in a topological-insulator nanowire proximity-coupled to an s-wave superconductor. *Phys. Rev. B*, 84:201105, Nov 2011.

[18] A. Das, Y. Ronen, Y. Most, Y. Oreg, M. Heiblum, and H. Shtrikman. Zero-bias peaks and splitting in an Al-InAs nanowire topological superconductor as a signature of Majorana fermions. *Nature Phys.*, 8(12):887–895, 2012.

[19] M. T. Deng, C. L. Yu, G. Y. Huang, M. Larsson, P. Caroff, and H. Q. Xu. Observation of Majorana Fermions in a Nb-InSb Nanowire-Nb Hybrid Quantum Device. *Nano Lett.*, 12:6414, apr 2012.

[20] M. T. Deng, C. L. Yu, G. Y. Huang, M. Larsson, P. Caroff, and H. Q. Xu. Parity independence of the zero-bias conductance peak in a nanowire based topological superconductor-quantum dot hybrid device. *Scientific Reports*, 4:7261, 2014.

[21] S. Deng, L. Viola, and G. Ortiz. Majorana modes in time-reversal invariant s-wave topological superconductors. *Phys. Rev. Lett.*, 108:036803, Jan 2012.

[22] M. Duckheim and P. W. Brouwer. Andreev reflection from noncentrosymmetric superconductors and majorana bound-state generation in half-metallic ferromagnets. *Phys. Rev. B*, 83:054513, Feb 2011.

[23] E. Dumitrescu, B. Roberts, S. Tewari, J. D. Sau, and S. Das Sarma. Majorana fermions in chiral topological ferromagnetic nanowires. *Phys. Rev. B*, 91:094505, Mar 2015.

[24] H. Ebisu, K. Yada, H. Kasai, and Y. Tanaka. Majorana edge states and topological properties in 1d/2d rashba semiconductor proximity coupled to iron-based superconductor. *Superconductor Science and Technology*, 28(1):014001, 2015.

[25] H. Ebisu, K. Yada, H. Kasai, and Y. Tanaka. Odd-frequency pairing in topological superconductivity in a one-dimensional magnetic chain. *Phys. Rev. B*, 91:054518, Feb 2015.

[26] L. Fidkowski, J. Alicea, N. H. Lindner, R. M. Lutchyn, and M. P. A. Fisher. Universal transport signatures of majorana fermions in superconductor-luttinger liquid junctions. *Phys. Rev. B*, 85:245121, Jun 2012.

[27] A. D. K. Finck, D. J. Van Harlingen, P. K. Mohseni, K. Jung, and X. Li. Anomalous modulation of a zero-bias peak in a hybrid nanowire-superconductor device. *Phys. Rev. Lett.*, 110:126406, Mar 2013.

[28] P. A. Frigeri, D. F. Agterberg, A. Koga, and M. Sigrist. Superconductivity without inversion symmetry: Mnsi versus cept$_3$Si. *Phys. Rev. Lett.*, 92:097001, Mar 2004.

[29] L. Fu and C. L. Kane. Superconducting proximity effect and majorana fermions at the surface of a topological insulator. *Phys. Rev. Lett.*, 100:096407, Mar 2008.

[30] L. Fu and C. L. Kane. Josephson current and noise at a superconductor/quantum-spin-hall-insulator/superconductor junction. *Phys. Rev. B*, 79:161408(R), 2009.

[31] E. Gaidamauskas, J. Paaske, and K. Flensberg. Majorana bound states in two-channel time-reversal-symmetric nanowire systems. *Phys. Rev. Lett.*, 112:126402, Mar 2014.

[32] S. Gangadharaiah, B. Braunecker, P. Simon, and D. Loss. Majorana edge states in interacting one-dimensional systems. *Phys. Rev. Lett.*, 107(3):036801, Jul 2011.

[33] T. Giamarchi. *Quantum Physics in One Dimension*. Oxford University Press, Oxford, 2003.

[34] L. P. Gor'kov and E. I. Rashba. Superconducting 2d system with lifted spin degeneracy: Mixed singlet-triplet state. *Phys. Rev. Lett.*, 87:037004, Jul 2001.

[35] A. Heimes, D. Mendler, and P. Kotetes. Interplay of topological phases in magnetic adatom-chains on top of a Rashba superconducting surface. *New Journal of Physics*, 17(2):023051, Feb. 2015.

[36] A. P. Higginbotham, S. M. Albrecht, G. Kirsanskas, W. Chang, F. Kuemmeth, P. Krogstrup, T. S. Jespersen, J. Nygard, K. Flensberg, and C. M. Marcus. Parity lifetime of bound states in a proximitized semiconductor nanowire. *Nature Physics*, 11:1017, Jan. 2015.

[37] H.-Y. Hui, P. M. R. Brydon, J. D. Sau, S. Tewari, and S. D. Sarma. Majorana fermions in ferromagnetic chains on the surface of bulk spin-orbit coupled s-wave superconductors. *Scientific Reports*, 5:8880, Mar. 2015.

[38] S.-H. Ji, T. Zhang, Y.-S. Fu, X. Chen, X.-C. Ma, J. Li, W.-H. Duan, J.-F. Jia, and Q.-K. Xue. High-resolution scanning tunneling spectroscopy of magnetic impurity induced bound states in the superconducting gap of pb thin films. *Phys. Rev. Lett.*, 100:226801, Jun 2008.

[39] A. Keselman, L. Fu, A. Stern, and E. Berg. Inducing time-reversal-invariant topological superconductivity and fermion parity pumping in quantum wires. *Phys. Rev. Lett.*, 111:116402, Sep 2013.

[40] Y. Kim, J. Cano, and C. Nayak. Majorana zero modes in semiconductor nanowires in contact with higher-T_c superconductors. *Phys. Rev. B*, 86:235429, Dec 2012.

[41] Y. Kim, M. Cheng, B. Bauer, R. M. Lutchyn, and S. Das Sarma. Helical order in one-dimensional magnetic atom chains and possible emergence of majorana bound states. *Phys. Rev. B*, 90:060401, Aug 2014.

[42] Y. Kim, J. Zhang, E. Rossi, and R. M. Lutchyn. Impurity-induced bound states in superconductors with spin-orbit coupling. *Phys. Rev. Lett.*, 114:236804, Jun 2015.

[43] A. Kitaev. Fault-tolerant quantum computation by anyons. *Ann. Phys.*, 303:2, 2002.

[44] A. Kitaev. Periodic table for topological insulators and superconductors. In V. Lebedev and M. Feigel'Man, editors, *American Institute of Physics Conference Series*, volume 1134 of *American Institute of Physics Conference Series*, pages 22–30, May 2009.

[45] A. Y. Kitaev. Unpaired majorana fermions in quantum wires. *Physics-Uspekhi*, 44(10S):131, 2001.

[46] J. Klinovaja, P. Stano, A. Yazdani, and D. Loss. Topological superconductivity and majorana fermions in rkky systems. *Phys. Rev. Lett.*, 111:186805, Nov 2013.

[47] J. Klinovaja, A. Yacoby, and D. Loss. Kramers pairs of majorana fermions and parafermions in fractional topological insulators. *Phys. Rev. B*, 90:155447, Oct 2014.

[48] K. T. Law, P. A. Lee, and T. K. Ng. Majorana fermion induced resonant andreev reflection. *Phys. Rev. Lett.*, 103:237001, 2009.

[49] J. Li, H. Chen, I. K. Drozdov, A. Yazdani, B. A. Bernevig, and A. H. MacDonald. Topological superconductivity induced by ferromagnetic metal chains. *Phys. Rev. B*, 90:235433, Dec 2014.

[50] J. Li, W. Pan, B. A. Bernevig, and R. M. Lutchyn. Detection of majorana kramers pairs using a quantum point contact. *ArXiv e-prints*, Nov. 2015.

[51] D. E. Liu, M. Cheng, and R. M. Lutchyn. Probing majorana physics in quantum-dot shot-noise experiments. *Phys. Rev. B*, 91:081405, Feb 2015.

[52] D. E. Liu, A. Levchenko, and R. M. Lutchyn. Majorana zero modes choose euler numbers as revealed by full counting statistics. *Phys. Rev. B*, 92:205422, Nov 2015.

[53] A. M. Lobos, R. M. Lutchyn, and S. Das Sarma. Interplay of disorder and interaction in majorana quantum wires. *Phys. Rev. Lett.*, 109:146403, Oct 2012.

[54] R. M. Lutchyn, J. D. Sau, and S. Das Sarma. Majorana fermions and a topological phase transition in semiconductor-superconductor heterostructures. *Phys. Rev. Lett.*, 105:077001, Aug 2010.

[55] R. M. Lutchyn and J. H. Skrabacz. Transport properties of topological superconductor˘luttinger liquid junctions: A real-time keldysh approach. *Phys. Rev. B*, 88:024511, Jul 2013.

[56] R. M. Lutchyn, T. D. Stanescu, and S. Das Sarma. Search for majorana fermions in multiband semiconducting nanowires. *Phys. Rev. Lett.*, 106(12):127001, Mar 2011.

[57] D. L. Maslov, M. Stone, P. M. Goldbart, and D. Loss. Josephson current and proximity effect in luttinger liquids. *Phys. Rev. B*, 53:1548–1557, Jan 1996.

[58] G. C. Ménard, S. Guissart, C. Brun, S. Pons, V. S. Stolyarov, F. Debontridder, M. V. Leclerc, E. Janod, L. Cario, D. Roditchev, P. Simon, and T. Cren. Coherent long-range magnetic bound states in a superconductor. *Nature Physics*, 11:1013–1016, Dec. 2015.

[59] C. Moca, E. Demler, B. Jankó, and G. Zaránd. Spin-resolved spectra of shiba multiplets from mn impurities in mgb_2. *Phys. Rev. B*, 77:174516, May 2008.

[60] V. Mourik, K. Zuo, S. M. Frolov, S. R. Plissard, E. P. A. M. Bakkers, and L. P. Kouwenhoven. Signatures of Majorana Fermions in Hybrid Superconductor-Semiconductor Nanowire Devices. *Science*, 336:1003–, May 2012.

[61] S. Nadj-Perge, I. K. Drozdov, B. A. Bernevig, and A. Yazdani. Proposal for realizing majorana fermions in chains of magnetic atoms on a superconductor. *Phys. Rev. B*, 88:020407, Jul 2013.

[62] S. Nadj-Perge, I. K. Drozdov, J. Li, H. Chen, S. Jeon, J. Seo, A. H. MacDonald, B. A. Bernevig, and A. Yazdani. Observation of majorana fermions in ferromagnetic atomic chains on a superconductor. *Science*, 2014.

[63] N. Nagaosa. *Quantum Field Theory in Strongly Correlated Electronic Systems*. Springer, 1999.

[64] S. Nakosai, J. C. Budich, Y. Tanaka, B. Trauzettel, and N. Nagaosa. Majorana bound states and nonlocal spin correlations in a quantum wire on an unconventional superconductor. *Phys. Rev. Lett.*, 110:117002, Mar 2013.

[65] C. Nayak, S. H. Simon, A. Stern, M. Freedman, and S. Das Sarma. Non-abelian anyons and topological quantum computation. *Rev. Mod. Phys.*, 80:1083, 2008.

[66] J. Nilsson, A. R. Akhmerov, and C. W. J. Beenakker. Splitting of a cooper pair by a pair of majorana bound states. *Phys. Rev. Lett.*, 101:120403, Sep 2008.

[67] Y. Niu, S. B. Chung, C.-H. Hsu, I. Mandal, S. Raghu, and S. Chakravarty. Majorana zero modes in a quantum ising chain with longer-ranged interactions. *Phys. Rev. B*, 85:035110, Jan 2012.

[68] M. R. Norman, M. Randeria, H. Ding, and J. C. Campuzano. Phenomenological models for the gap anisotropy of $bi_2sr_2cacu_2o_8$ as measured by angle-resolved photoemission spectroscopy. *Phys. Rev. B*, 52:615–622, Jul 1995.

[69] Y. Oreg, G. Refael, and F. von Oppen. Helical liquids and majorana bound states in quantum wires. *Phys. Rev. Lett.*, 105:177002, 2010.

[70] R. Pawlak, M. Kisiel, J. Klinovaja, T. Meier, S. Kawai, T. Glatzel, D. Loss, and E. Meyer. Probing Atomic Structure and Majorana Wavefunctions in Mono-Atomic Fe-chains on Superconducting Pb-Surface. *ArXiv e-prints*, May 2015.

[71] Y. Peng, F. Pientka, L. I. Glazman, and F. von Oppen. Strong localization of majorana end states in chains of magnetic adatoms. *Phys. Rev. Lett.*, 114:106801, Mar 2015.

[72] F. Pientka, L. I. Glazman, and F. von Oppen. Topological superconducting phase in helical shiba chains. *Phys. Rev. B*, 88:155420, Oct 2013.

[73] F. Pientka, L. I. Glazman, and F. von Oppen. Unconventional topological phase transitions in helical shiba chains. *Phys. Rev. B*, 89:180505, May 2014.

[74] D. I. Pikulin, Y. Komijani, and I. Affleck. Luttinger liquid in contact with a kramers pair of majorana bound states. *ArXiv e-prints*, Nov. 2015.

[75] K. Pöyhönen, A. Weststrom, J. Röntynen, and T. Ojanen. Majorana states in helical shiba chains and ladders. *Phys. Rev. B*, 89:115109, Mar 2014.

[76] W. Qing-Yan, L. Zhi, Z. Wen-Hao, Z. Zuo-Cheng, Z. Jin-Song, L. Wei, D. Hao, O. Yun-Bo, D. Peng, C. Kai, W. Jing, S. Can-Li, H. Ke, J. Jin-Feng, J. Shuai-Hua, W. Ya-Yu, W. Li-Li, C. Xi, M. Xu-Cun, and X. Qi-Kun. Interface-induced high-temperature superconductivity in single unit-cell fese films on srtio 3. *Chinese Physics Letters*, 29(3):037402, 2012.

[77] N. Read. Role of infrared divergences in the 1/n expansion of the u= anderson model. *Journal of Physics C: Solid State Physics*, 18(13):2651, 1985.

[78] N. Read and D. M. Newns. On the solution of the coqblin-schrieffer hamiltonian by the large-n expansion technique. *J. Phys. C-solid State Phys.*, 16(17):3273–3295, 1983.

[79] M. Ruby, F. Pientka, Y. Peng, F. von Oppen, B. W. Heinrich, and K. J. Franke. End states and subgap structure in proximity-coupled chains of magnetic adatoms. *Phys. Rev. Lett.*, 115:197204, Nov 2015.

[80] A. I. Rusinov. Superconductivity near a Paramagnetic Impurity. *Soviet Journal of Experimental and Theoretical Physics Letters*, 9:85, 1969.

[81] M. Sato and S. Fujimoto. Topological phases of noncentrosymmetric superconductors: Edge states, majorana fermions, and non-abelian statistics. *Phys. Rev. B*, 79(9):094504, Mar 2009.

[82] J. D. Sau and E. Demler. Bound states at impurities as a probe of topological superconductivity in nanowires. *Phys. Rev. B*, 88:205402, Nov 2013.

[83] J. D. Sau, S. Tewari, and S. Das Sarma. Experimental and materials considerations for the topological superconducting state in electron- and hole-doped semiconductors: Searching for non-abelian majorana modes in 1d nanowires and 2d heterostructures. *Phys. Rev. B*, 85:064512, Feb 2012.

[84] A. P. Schnyder, S. Ryu, A. Furusaki, and A. W. W. Ludwig. Classification of topological insulators and superconductors in three spatial dimensions. *Phys. Rev. B*, 78:195125, Nov 2008.

[85] C. Schrade, A. A. Zyuzin, J. Klinovaja, and D. Loss. Proximity-induced π josephson junctions in topological insulators and kramers pairs of majorana fermions. *Phys. Rev. Lett.*, 115:237001, Dec 2015.

[86] J. R. Schrieffer and P. A. Wolff. Relation between the anderson and kondo hamiltonians. *Phys. Rev.*, 149:491–492, Sep 1966.

[87] H. Shiba. Classical Spins in Superconductors. *Progress of Theoretical Physics*, 40:435–451, 1968.

[88] S. Takei, B. M. Fregoso, V. Galitski, and S. Das Sarma. Topological superconductivity and majorana fermions in hybrid structures involving cuprate high-T_c superconductors. *Phys. Rev. B*, 87:014504, Jan 2013.

[89] S. Takei and V. Galitski. Microscopic theory for a ferromagnetic nanowire/superconductor heterostructure: Transport, fluctuations, and topological superconductivity. *Phys. Rev. B*, 86:054521, Aug 2012.

[90] J. C. Y. Teo and C. L. Kane. Topological defects and gapless modes in insulators and superconductors. *Phys. Rev. B*, 82:115120, Sep 2010.

[91] S. Tewari, T. D. Stanescu, J. D. Sau, and S. D. Sarma. Topologically non-trivial superconductivity in spinorbit-coupled systems: bulk phases and quantum phase transitions. *New Journal of Physics*, 13(6):065004, 2011.

[92] M. M. Vazifeh and M. Franz. Self-organized topological state with majorana fermions. *Phys. Rev. Lett.*, 111:206802, Nov 2013.

[93] A. Weststrom, K. Pöyhönen, and T. Ojanen. Topological properties of helical shiba chains with general impurity strength and hybridization. *Phys. Rev. B*, 91:064502, Feb 2015.

[94] C. L. M. Wong and K. T. Law. Majorana kramers doublets in $d_{x^2-y^2}$-wave superconductors with rashba spin-orbit coupling. *Phys. Rev. B*, 86:184516, Nov 2012.

[95] L. Yu. Bound state in superconductors with paramagnetic impurities. *Acta Physica Sinica*, 21(1):75, 1965.

[96] F. Zhang, C. L. Kane, and E. J. Mele. Time-reversal-invariant topological superconductivity and majorana kramers pairs. *Phys. Rev. Lett.*, 111:056402, Aug 2013.

[97] H. Zhang, O. Gül, S. Conesa-Boj, K. Zuo, V. Mourik, F. K. de Vries, J. van Veen, D. J. van Woerkom, M. P. Nowak, M. Wimmer, D. Car, S. Plissard, E. P. A. M. Bakkers, M. Quintero-Pérez, S. Goswami, K. Watanabe, T. Taniguchi, and L. P. Kouwenhoven. Ballistic majorana nanowire devices. *ArXiv e-prints*, Mar. 2016.

[98] J. Zhang, Y. Kim, E. Rossi, and R. M. Lutchyn. Topological superconductivity in a multichannel yu-shiba-rusinov chain. *Phys. Rev. B*, 93:024507, Jan 2016.